

Nanostructured Oxides in Chemistry: Characterization and Properties

M. Fernández-García,^{*,†} A. Martínez-Arias,[†] J. C. Hanson,[‡] and J. A. Rodríguez^{*,‡}

Instituto de Catálisis y Petroleoquímica, CSIC, C/ Marie Curie s/n, Campus Cantoblanco, 28049-Madrid, Spain, and Brookhaven National Laboratory, Chemistry Department, Building 555, Upton, New York 11973

Received December 22, 2003

Contents

| | |
|--|------|
| 1. Introduction | 4063 |
| 2. Characterization of Nanostructured Oxides | 4066 |
| 2.1. Analysis of Structural Characteristics | 4067 |
| 2.1.1. XRD and PDF | 4067 |
| 2.1.2. XAS | 4069 |
| 2.1.3. Raman Spectroscopy | 4071 |
| 2.1.4. TEM and STEM | 4073 |
| 2.1.5. STM and AFM | 4075 |
| 2.2. Analysis of Electronic Characteristics | 4076 |
| 2.2.1. XANES | 4076 |
| 2.2.2. Optical Absorption | 4077 |
| 2.2.3. Valence and Core-Level Photoemission | 4079 |
| 2.2.4. Theoretical Studies | 4081 |
| 3. Oxide Systems | 4084 |
| 3.1. Ti-Containing Oxides | 4084 |
| 3.1.1. Pure Titania Nanoparticles | 4084 |
| 3.1.2. Ti-Containing Mixed-Metal Oxides | 4085 |
| 3.2. Zr-Containing Oxides | 4086 |
| 3.3. Ce-Containing Oxides | 4087 |
| 3.3.1. Pure Ceria Nanoparticles | 4087 |
| 3.3.2. Ce-Containing Mixed-Metal Oxides | 4089 |
| 3.4. MgO and Other Alkaline-Earth Oxides | 4091 |
| 3.5. Other Oxides | 4092 |
| 4. Physicochemical Properties | 4093 |
| 4.1. Charge-Related Phenomena: Transport and Photochemistry | 4093 |
| 4.1.1. Transport Properties and Techniques Employed for their Analysis | 4093 |
| 4.1.2. Photochemical Properties | 4095 |
| 4.2. Chemical Reactivity and Surface Properties | 4096 |
| 5. Concluding Remarks and Future Work | 4098 |
| 6. Acknowledgment | 4098 |
| 7. References | 4098 |

1. Introduction

Metal oxides play a very important role in many areas of chemistry, physics, and materials science.^{1–5} The metal elements are able to form a large diversity of oxide compounds.⁶ These can adopt a vast number of structural geometries with an electronic structure that can exhibit metallic, semiconductor, or insulator

characteristics. In technological applications, oxides are used in the fabrication of microelectronic circuits, sensors, piezoelectric devices, fuel cells, coatings for the passivation of surfaces against corrosion, and as catalysts. For example, almost all catalysts used in industrial applications involve an oxide as active phase, promoter, or “support”. In the chemical and petrochemical industries, products worth billions of dollars are generated every year through processes that use oxide and metal/oxide catalysts.⁷ For the control of environmental pollution, catalysts or sorbents that contain oxides are employed to remove the CO, NO_x, and SO_x species formed during the combustion of fossil-derived fuels.^{8,9} Furthermore, the most active areas of the semiconductor industry involve the use of oxides.¹⁰ Thus, most of the chips used in computers contain an oxide component.

In the emerging field of nanotechnology, a goal is to make nanostructures or nanoarrays with special properties with respect to those of bulk or single particle species.^{11–15} Oxide nanoparticles can exhibit unique chemical properties due to their limited size and a high density of corner or edge surface sites. In recent years, methods have been developed for the preparation of novel nanostructures of oxides. They can be generated by a number of preparation methods that typically are described as physical and chemical methods.^{16,17} These all produce solid powders with a reasonable control of the primary particle size, i.e., the size of a single crystallite, as well as of a secondary particle size, i.e., the size of a typical agglomerate of crystallites. Physical-like methods include gas/vapor condensation, thermochemical/flame methods, and spray pyrolysis (the name of the method essentially indicates the energy source applied to provide high temperature during gas-to-solid conversion). Gas condensation methods, which form a supersaturated vapor of metals in a first stage of condensation under (high pressure) inert gas with a subsequent stage of oxidation, are among the earlier preparative methods due to their ease of performance and high purity of the resulting solids, although they have the drawbacks of high cost and low yield. Thermochemical methods are typically used to synthesize ceramic precursor powders and are customarily referred to as chemical vapor deposition. Chemical salts/precursors are vaporized and subsequently oxidized in a combustion process using a fuel-oxidant mixture which induces rapid thermal degradation and reaction with oxygen. This method is industrially

* To whom correspondence should be addressed.

[†] Instituto de Catálisis y Petroleoquímica, CSIC.

[‡] Brookhaven National Laboratory.

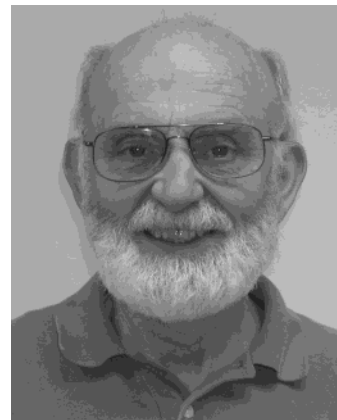


Marcos Fernández-García was born in Madrid, Spain. He obtained his B.S. degree in physical chemistry from Complutense University in Madrid in 1989. In 1993, he obtained a Ph.D. in chemistry under the supervision of Prof. J. C. Conesa working at the "Instituto de Catálisis y Petroleoquímica" (CSIC). He conducted postdoctoral work at Yale University with Prof. G. L. Haller from 1994 to 1995. In 1998, he was awarded a European Fellowship by the Royal Society (London) which funded a visit to Dundee University, UK. In 1999, he joined the Institute of "Catálisis y Petroleoquímica" as "Científico Titular". Currently, his research is focused on comparing the chemical properties of nanostructured catalysts based on the use of metal or oxide phases as active components. At an experimental level, his research centers on the use of in-situ synchrotron-based techniques (XANES and EXAFS) and spectroscopies (Raman, infrared, and electron paramagnetic resonance) for the characterization of catalytic materials under real, operating conditions. Quantum-chemical calculations based on *ab initio* (Hartree–Fock and multiconfigurational) approaches have been also performed to help in the interpretation of experimental results. In 1996, he received the Volkswagen-CSIC award for environmental research. He is coauthor of over 90 papers and 2 review articles published in international journals, 5 book chapters, and recently has co-edited a book titled *Supported Metals in Catalysis* (Imperial College Press, 2004).

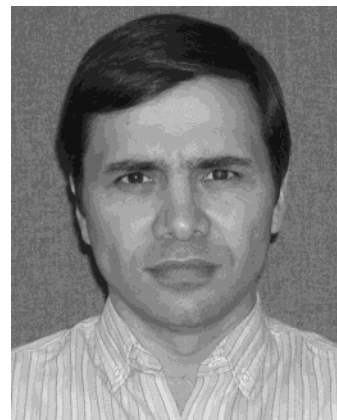


Arturo Martínez Arias was born in Madrid in 1965. He studied chemistry (physical chemistry) at the Universidad Autónoma de Madrid in which he received his Ph.D. degree in 1994. His doctoral thesis was developed at the Instituto de Catálisis y Petroleoquímica, CSIC, under the supervision of Prof. J. Soria and dealt with surface characterization of ceria-related catalysts with the use of probe molecules. After a postdoctoral stay at the Université Pierre et Marie Curie, Paris, in the group of Prof. M. Che, he returned to the ICP–CSIC in Madrid, in which he became Tenured Scientist in 2001. He is the author of 85 scientific articles or book chapters and 56 contributions to scientific congresses. His current research interests are in the field of heterogeneous catalysis applications in energy and environment sectors.

used due to its low cost, but control of particle size and morphology is somewhat difficult. Finally, spray pyrolysis involves generation of aerosol droplets by



Jonathan Hanson was born in Chicago, Illinois. He did his undergraduate education at Northwestern University where he received a B.S. in science engineering. He received a Ph.D. in chemistry under supervision of Christer Nordman at the University of Michigan. Then, he conducted postdoctoral work in crystallography under George Stout and Lyle Jensen at the University of Washington and with Warner Love at Johns Hopkins University. He came to Brookhaven National Laboratory in 1977 to work with Beno Schoenborn in the study of proteins with neutron diffraction. In 1993, he became beam line scientist at the National Synchrotron Light Source at Brookhaven National Laboratory. His main interest is the application of X-ray and neutron diffraction in solid-state chemistry and in the characterization of heterogeneous catalysts. Over the years, he has developed in-situ diffraction techniques with Poul Norby and Axel Christensen of Aarhus University in Denmark and Clare Grey and John Parise at the State University of New York.



José A. Rodríguez was born in Caracas, Venezuela. He did his undergraduate education at Simon Bolívar University, where he received B.S. degrees in chemistry and chemical engineering. After getting an M.S. in theoretical chemistry at Simon Bolívar University, he moved to the United States to get a Ph.D. in physical chemistry at Indiana University, Bloomington. In his Ph.D. thesis, he worked under the supervision of C. T. Campbell and used surface-science techniques and theoretical methods to study the elementary steps of the water-gas shift reaction and methanol synthesis over Cu and ZnO catalysts. He conducted postdoctoral work at Texas A&M University with D. W. Goodman. In Texas A&M, he became interested in the behavior of bimetallic systems and established systematic correlations between their electronic and chemical properties. In the early 1990s, he joined Brookhaven National Laboratory, where he is currently a Senior Scientist. Nowadays, he is studying and comparing the chemical properties of nanoparticles and extended surfaces of metals, oxides, and carbides. At an experimental level, his research centers on the use of synchrotron-based techniques (high-resolution photoemission, infrared spectroscopy, time-resolved X-ray diffraction, and X-ray absorption spectroscopy) for the characterization of catalytic materials. Quantum-chemical calculations based on density functional theory are performed to help in the interpretation of experimental results and provide fundamental information on the physical properties of solids or nanoparticles and the mechanisms of catalytic reactions.

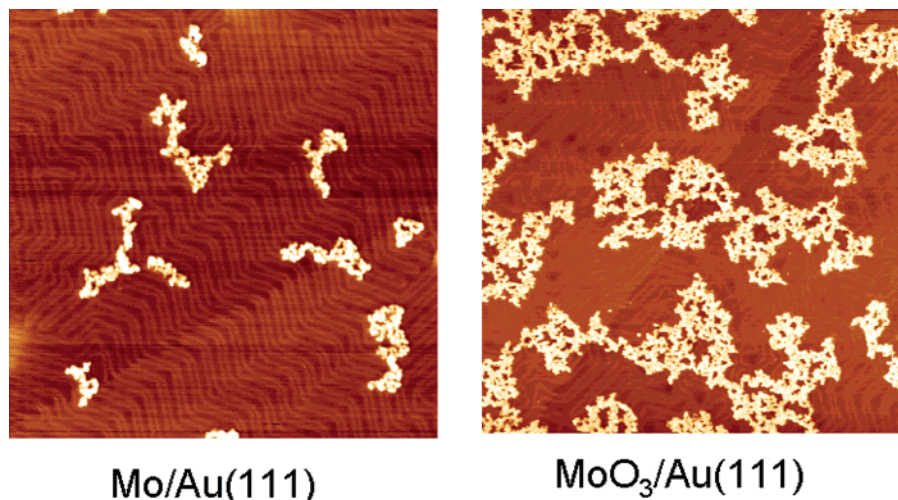


Figure 1. STM images recorded before and after oxidizing Mo nanoparticles on a Au(111) template. Image size: $190 \times 190 \text{ nm}^2$. Reprinted with permission from ref 23. Copyright 2003 American Chemical Society.

nebulization of a starting solution, sol or suspension of a precursor, further evaporation of the solvent, drying, and thermolysis at high temperature to form microporous particles, which can sinter to form more or less dense materials depending on experimental conditions. A disadvantage of spray pyrolysis is the large amount of solvent required, while the high purity of the process is a typical plus. On the other hand, current liquid-phase chemical methods are sol-gel, micellar, and chemical/mechanical synthesis.¹⁶ Some of the chemical methods may offer potential routes to obtain better materials in terms of chemical homogeneity, particularly in the case of mixed oxides, and morphological control (i.e., primary and secondary particle size) with respect to the above-mentioned physical methods. Most apparent additional differences between the two kinds of preparation methods can be related to surface properties and, particularly, to hydrophilicity/hydrophobicity as controlled by hydroxyl concentration and characteristics.¹⁷ Sol-gel is becoming a standard method in synthesizing oxides and is based in the hydrolysis of reactive metal precursors, usually alkoxides in an alcohol solution, resulting in a gel that is subsequently thermally or hydrothermally treated to yield the nanostructured product. Advantages of this preparation are the production of ultrafine powders having high chemical homogeneity. Micellar methods use micelles as microreactors in which the oxide or oxide precursor are obtained by reaction between solvated cations and a precipitating agent. This method is also used to obtain ultrafine powders with significant control of chemical homogeneity and particle size but at the cost of low and expensive production yields. Mechanochemical synthesis involves mechanical activation of solid reactions by the milling of precursor powders (usually a salt and a metal oxide) to form the desired nanoscale compound, which can be typically obtained after heating and purification. Other chemical methods currently used include the use of complexing agents (e.g., citrate) or other than micellar colloidal methods. Finally, it can be mentioned that precipitation from solution was the conventional method in the past, but the need of a degree of control

of size in the nanometer range has diminished its utility significantly.^{16,17}

Although all these methods yield well-defined solids, in the case of metal oxides their size distribution differs from a delta function and is typically asymmetric; both facts influence the interpretation of results coming from characterization techniques.¹⁶ To characterize these complex systems and explore possible correlations among their structural, electronic, and chemical properties, one needs sophisticated experimental techniques and state-of-the-art theory. The combination of experimental and theoretical studies should produce a "conceptual frame" that will allow the rational design and manipulation of oxide nanoparticles and nanoarrays.

Particle size is expected to influence three important groups of properties in any material. The first one comprises the structural characteristics, namely, the lattice symmetry and cell parameters.¹⁸ Bulk oxides are usually robust and stable systems with well-defined crystallographic structures. However, the growing importance of surface free energy and stress with decreasing particle size must be considered: changes in thermodynamic stability associate with size can induce modification of cell parameters and/or structural transformations^{18–21} and in extreme cases the nanoparticle can disappear due to interactions with its surrounding environment and a high surface free energy.²² To display mechanical or structural stability, a nanoparticle must have a low surface free energy. As a consequence of this requirement, phases that have a low stability in bulk materials can become very stable in nanostructures. This structural phenomenon has been detected in TiO_2 , VO_x , Al_2O_3 or MoO_x oxides.^{19–21,23} For example, in the case of alumina the stable structure for microsized samples is the alpha phase while gamma appears more stable for nanostructured materials.²⁰ The surface free energy and stress also strongly affect the organization of the nanoparticles on a substrate or template. This is illustrated by the images of scanning tunneling microscopy (STM) shown in Figure 1.²³ In the left-side panel, Mo nanoparticles are present on a Au(111) substrate. Due to the

relatively high surface free energy of Mo with respect to Au,²⁴ the Mo nanoparticles form three-dimensional aggregates and Mo/Au surface alloys.²⁵ Upon reaction with oxygen the Mo transforms into MoO₃, which has a low surface free energy and spreads out covering the Au(111) substrate. MoO₃ nanoparticles formed by this approach have a structure different from that seen in the most common phases of bulk MoO₃.²³

Size-induced structural distortions associated with changes in cell parameters have been observed in nanoparticles of Al₂O₃,²⁰ NiO,²⁶ Fe₂O₃,²⁷ ZrO₂,²⁸ MoO₃,²³ CeO₂,²⁹ and Y₂O₃.³⁰ As the particle size decreases, the increasing number of surface and interface atoms generates stress/strain and concomitant structural perturbations.^{29,31,32} Beyond this “intrinsic” strain, there may be also “extrinsic” strain associated with a particular synthesis method, which may be partially relieved by annealing or calcination.²⁹ On the other hand, interactions with the substrate on which the nanoparticles are supported can complicate the situation and induce structural perturbations or phases not seen for the bulk state of the oxide.³³

The second important effect of size is related to the electronic properties of the oxide. In any material, the nanostructure produces the so-called quantum size or confinement effects which essentially arise from the presence of discrete, atom-like electronic states. From a solid-state point of view, these states can be considered as being a superposition of bulklike states with a concomitant increase in oscillator strength.³⁴ Additional general electronic effects of quantum confinement experimentally probed on oxides are related to the energy shift of exciton levels and optical band gap.^{35,36} An important factor to consider when dealing with the electronic properties of a bulk oxide surface are the long-range effects of the Madelung field, which are not present or limited in an oxide nanoparticle.^{37–39} Theoretical studies for oxides show a redistribution of charge when going from large periodic structures to small clusters or aggregates which must be roughly considered to be relatively small for ionic solids while significantly larger for covalent ones.^{40–45} The degree of ionicity or covalency in a metal–oxygen bond can however strongly depend on size in systems with partial ionic or covalent character; an increase in the ionic component to the metal–oxygen bond in parallel to the size decreasing has been proposed.¹⁸

Structural and electronic properties obviously drive the chemical properties of the solid, the third group of properties influenced by size in a simple classification. In their bulk state, many oxides have wide band gaps and a low reactivity.⁴⁶ A decrease in the average size of an oxide particle does in fact change the magnitude of the band gap,^{35,47} with strong influence in the chemical reactivity.^{48,49} Surface properties are a somewhat particular group included in this subject due to their importance in chemistry. Solid–gas or solid–liquid chemical reactions can be mostly confined to the surface and/or subsurface regions of the solid. As mentioned above, the two-dimensional (2D) nature of surfaces has notable structural, typically a rearrangement or reconstruction of bulk geom-

etries,^{3,14,50} and electronic, e.g., presence of mid-gap states,^{45,51} consequences. In the case of nanostructured oxides, surface properties are strongly modified with respect to 2D infinite surfaces, producing solids with unprecedented sorption or acid/base characteristics.⁵² Furthermore, the presence of undercoordinated atoms (like corners or edges) or O vacancies in an oxide nanoparticle should produce specific geometrical arrangements as well as occupied electronic states located above the valence band of the corresponding bulk material,^{53–55} enhancing in this way the chemical activity of the system.^{46,48,56}

This article provides a review of recent studies that deal with the chemistry of nanostructured oxides. Although closely connected with the chemistry and physics of extended/infinite surfaces, the previous introduction clearly states the significant differences encountered between these two types of systems. Isolated centers, typically in zeotypes or mesoporous materials, or located in oxides by doping, are out of the scope of this review as their properties are mostly associated to their electronic structure in a specific local geometric environment and not to collective properties of the systems as a whole. We feel that it is important to stress the need for a fundamental understanding of the behavior of nanostructured oxides, particularly for sizes in which the surface atoms represent a significant percentage of the total number of atoms present in the solid particle, e.g., below 10 nm. The review begins with the presentation of an array of experimental techniques and theoretical methods that are useful for examining the behavior of nanostructures and/or nanoarrays. Then, systematic studies concerned with the structural and electronic properties of several types of size-limited oxides are discussed. The emphasis will be on well-defined systems that allow the study of relationships between physical and chemical properties. At the end, we will describe several areas in which nanostructured oxides can have a technological impact.

2. Characterization of Nanostructured Oxides

As briefly outlined in the introduction, nanostructured solids are nowadays generated by a series of different physical and chemical preparation methods.^{16,17} Although such synthetic methods have reached significant advances in terms of homogeneity in the structural/electronic properties of the particles forming the solid, as well as in the size distribution, still much work is needed to obtain full control of the synthesis variables and their influence in the final metal oxide solid prepared. Problems related to oxide stoichiometry and metal oxidation state (commonly at surface layers) or the presence of impurities and amorphous phases coexisting with the crystalline one are often encountered.^{57–59} A glimpse into these problems would indicate that structural and electronic properties as well as the primary particle size distribution are strongly dependent on the preparation method and, at the state of the art, a first goal is to perform a detailed and full characterization of the particular solid yielded by the specific preparation method used. To do this in a systematic way, one needs a diverse array of experimental techniques

Table 1. Possible Imperfections in Crystals^a

| type of imperfection | | description of imperfection |
|----------------------|-----------------------------------|---|
| point defects | interstitials | extra atom in an interstitial site |
| | Schottky defect Frenkel defect | atom missing from correct site atom displaced to interstitial site creating nearby vacancy |
| line defects | edge dislocation | row of atoms marking edge of a crystallographic plane extending only part way in crystal |
| | screw dislocation | row of atoms about which a normal crystallographic plane appears to spiral |
| plane defects | lineage boundary | boundary between two adjacent perfect regions in the same crystal that are slightly tilted with respect to each other |
| | grain boundary | boundary between two crystals in a polycrystalline solid |
| | stacking fault | boundary between two parts of closest packing having alternate stacking sequences |

^a From ref 65.

(X-ray diffraction and scattering, microscopies, vibrational and electron spectroscopies, etc.) and theoretical methods (ab initio and semiempirical quantum-mechanical calculations, Monte Carlo simulations, molecular dynamics, etc.). An important issue is the correct interpretation of the experimental results obtained by characterization techniques. To help in reaching this goal, in this section we will describe the most often used techniques and the specific consequences that nanostructure induces in their corresponding physicochemical observables.

2.1. Analysis of Structural Characteristics

2.1.1. XRD and PDF

Since the 1910s, X-ray crystallography has been a valuable tool for obtaining structural parameters of metal oxides.⁶ X-ray diffraction powder patterns come from the interference pattern of elastically dispersed X-ray beams by atom cores and, in the case of materials with moderate to long-range order, contain information that arises from the atomic structure and the particle characteristics (for example, size, strain). The effect of atomic structure on peak positions and intensities is described in textbooks,⁶⁰ and the effect of particle characteristics on peak shape has been recently reviewed.⁶¹

Alternatively, the radial distribution of the materials can be determined by the appropriate Fourier transform of the diffraction pattern independent of any requirement of long-range coherence. This is an advantage in the study of nanoparticles or nanostructures in which there is reduced long-range order. Egami and co-workers have applied this technique to metal oxide particles and obtained information about the structure and its defects.⁶² Finally, low angle X-ray diffraction⁶³ can be used to determine the structure of nanoparticles.

Particle Characteristics from Whole Powder Profile Fitting. Recent analyses of particle characteristics rely on least squares refinement of the whole powder diffraction profile, although there are several useful approximations that give some of these characteristics from individual peaks. The pattern is represented as a superposition of peaks where the peak position depends on the cell parameters, and the peak width is a sum of instrument parameters, particle size parameters (τ), and strain related pa-

rameters (ϵ). The particle size peak width is given by

$$\beta_{\tau} = K\lambda/\tau \cos \theta \quad (2.1.1.1.a)$$

while the strain peak width varies as

$$\beta_{\epsilon} = 4\epsilon \tan \theta \quad (2.1.1.1.b)$$

with λ representing the wavelength and θ representing the diffraction angle. The fact that the strain broadening follows a $\tan \theta$ function whereas the crystallite size broadening has a $1/\cos \theta$ dependence allows the separation of these effects in whole profile fitting through a range of θ .⁶⁴ Here, the strain (ϵ) can be the result of a nonuniform application of stress in the lattice of the nanoparticles and reflects variations in cell dimension within the sample. Obvious variations are present at the surface of the material with respect to bulk since local symmetry and distances are different.⁶¹ Additionally, oxygen vacancies and the different types of defects⁶⁵ shown in Table 1 can lead to strain in the lattice of a nanoparticle.⁶⁴ The relative importance of each type of defect depends on the size of the nanoparticle and the chemical nature of the oxide. Several cases will be described at length in section 3.

Additional structural features can be obtained from diffraction. In some cases, the refinement of the powder pattern can include structural parameters for the thermal motion of the atoms, the fractional occupancy and the positions. The quality of these refinements can be greatly improved with high energy X-rays where the absorption correction is negligible and a larger range of Q ($4\pi \sin(\theta)/\lambda$) can be measured.⁶⁶

Local Structure from Fourier Analysis of Whole Pattern. The local structure from amorphous nanoparticles can be determined from the diffraction pattern in a manner similar to techniques that have been used to determine the structures of liquids and glasses.⁶⁷ As an example, we describe the determination of the atomic pair distribution function (PDF) of amorphous quartz. Figure 2a shows the diffraction pattern from a quartz capillary. The local structure $g(r)$ is defined as the probability of finding an atom at a distance r from a reference atom and is derived from $G(r)$.

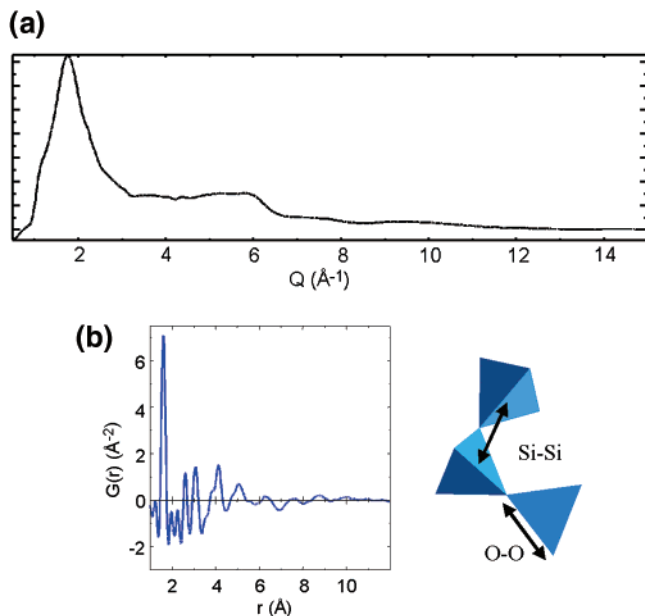


Figure 2. Part a shows the diffraction pattern for a quartz capillary. Part b displays the $G(r)$ obtained from the data in part a.

$$G(r) = 4\pi r[\rho(r) - \rho_0] \quad \rho(r) = \rho_0 g(r) \quad (2.1.1.2.a)$$

where $\rho(r)$ is the pair density function, and ρ_0 is the average pair density.

$G(r)$ is also the Fourier transform of the total structure factor, $S(Q)$

$$G(r) = (2/\pi) \int Q[S(Q) - 1] \sin(Qr) dQ \quad (2.1.1.2.b)$$

$$Q = 4\pi \sin(\theta)/\lambda \quad (2.1.1.2.c)$$

The structure factor $S(Q)$ is related to the elastic part of the diffraction intensity (I^{el}) as follows:

$$S(Q) = 1 + [I^{\text{el}}(Q) - \sum c_i |f_i(Q)|^2] / \sum c_i |f_i(Q)|^2 \quad (2.1.1.2.d)$$

where c_i is the fraction of species i , and $f_i(Q)$ is the atomic scattering factor of species i . The I^{el} is obtained from the total scattering after subtraction of background, and corrections for Compton scattering, absorption, multiple scattering.⁶² The calculated $G(r)$ is shown in Figure 2b. In this figure, we clearly see the Si–O, O–O, and Si–Si distances and some longer distances. The number of interatomic distances has decreased to nearly zero by the distance of 10 Å.

The real space resolution obtained in the PDF is directly dependent on the Q range measured, and it is therefore a necessity to measure data to high Q , with adequate counting statistics, to obtain well-resolved peaks in the PDF.⁶⁸ Generally, the data are collected at synchrotrons where high energy (short wavelength) and high intensity facilitate the above requirement. When the PDF technique is applied to crystalline materials, it has the advantage that the diffuse scattering data in the “background” (not under Bragg diffraction peaks) region contributes to the PDF. The obvious disadvantage of having a one-

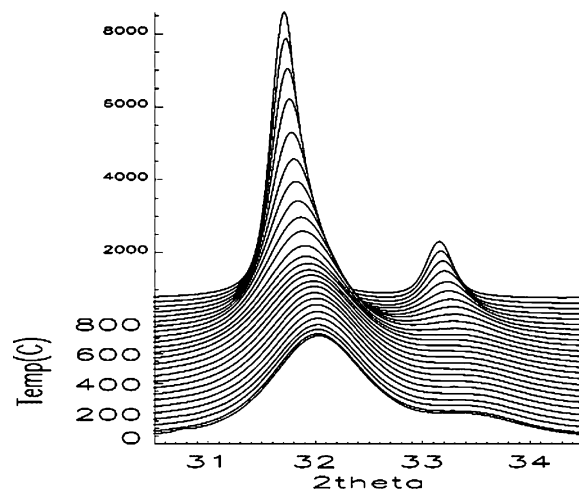


Figure 3. Time-resolved XRD data for the heating of $\text{Ce}_{0.9}\text{Zr}_{0.1}\text{O}_2$ nanoparticles in air. Heating rate = $4.8 \text{ }^\circ\text{C}/\text{min}$, $\lambda = 0.8941 \text{ \AA}$. Reprinted with permission from ref 76. Copyright 2003 American Chemical Society.

dimensional result is partly compensated by refining three-dimensional models of the one-dimensional data.⁶⁹

The PDF analysis of nanoparticles of ceria is another good example of the application of this tool to nanostructures of oxides.⁷⁰ In this case, data of neutron diffraction was used in the analysis. The neutron scattering cross-sections from cerium and oxygen are nearly equal, while X-ray diffraction scattering by oxygen is much less than cerium, and, consequently, neutron diffraction provides a more reliable determination of the oxygen structural features. However, a recent experiment on nano ceria using high energy X-rays ($\lambda = 0.15$) obtained similar results.⁷¹ Frenkel defects of the oxygen atoms in ceria were observed using this technique. Recent PDF studies⁷² of Zr-doped ceria have show that the oxygen storage capacity can be related to interfacial domains between the zirconium and cerium rich domains.

In-Situ Time-Resolved Powder Diffraction.

Investigations at Brookhaven National Laboratory and other institutions have established the feasibility of conducting subminute, time-resolved X-ray diffraction (XRD) experiments under a wide variety of temperature and pressure conditions ($-190 < T < 900 \text{ }^\circ\text{C}$; $P < 45 \text{ atm}$).^{73–75} This is made possible by the combination of synchrotron radiation with new parallel data-collection devices.⁷³ Using time-resolved XRD, one can follow structural changes during the preparation of nanoparticles and under reaction conditions. Figure 3 shows time-resolved powder diffraction results for Zr-doped nano ceria ($\text{Ce}_{0.9}\text{Zr}_{0.1}\text{O}_2$) during heating from 25 to 925 °C in air.⁷⁶ The sintering of the nanoparticles produces a sharpening of the diffraction peaks at temperatures above 600 °C. This type of approach can also provide information of changes in cell dimension or lattice strain with temperature.⁷⁶

Recently, the PDF technique has been extended/modified to allow the rapid acquisition of the necessary data. Time-resolved PDF measurements of nano catalysts under reaction conditions are now in progress.⁷⁷

2.1.2. XAS

The X-ray absorption structure (XAS) acronym refers to the oscillatory structure observed in the absorption coefficient ($\mu(E)$) just above or close to the absorption edge of an element constituting the sample. X-rays absorption spectroscopies are, essentially, synchrotron-based techniques and measure the absorption coefficient as a function of the X-ray energy $E = h\nu$. A typical absorption spectrum ($\mu(E)$ vs E) show three general features: the pre-edge, the edge, and an oscillatory structure that can be roughly described as a periodical function, progressively damped as evolves from the edge energy. As absorption techniques, XAS spectroscopies are element specific. On the other hand, the deep penetration of X-rays in the matter allows them to probe the whole system, being only surface sensitive by performing specific detection schemes which will be briefly discussed in section 2.2.1.

The XAS spectrum, $\chi(E)$, is defined phenomenologically as the normalized oscillatory structure of the X-ray absorption, e.g., $\chi(E) = (\mu(E) - \mu_0(E))/\mu_0(E)$, where $\mu_0(E)$ is the smooth varying atomic-like background absorption. Essentially, the XAS spectrum involves the quantum-mechanical transition from an inner, atomic-like core orbital electron to unoccupied bound (pre-edge transition) or unbound, free-like continuum levels. The oscillatory structure therefore reflects the unoccupied part of the electronic bands of the system in the presence of a core-hole.^{78–82} Note that this differs from the initial, ground state by physical effects induced by the fact that the core-hole is not infinitely long-lived but must decay as a function of time and distance from the photoabsorbed atom.^{78–82} The latter is a point to stress here as their short-range order character makes these techniques particularly suitable to analyze nanostructured materials which, frequently, do not possess or have a strongly disturbed long-range order.

Theoretical Background. Historically, it was controversial to recognize the local nature of the XAS techniques (see Lytle for a recent discussion),⁸³ but now the theoretical description of the techniques is reasonably well settled.^{80,81} The absorption of X-rays by matter is described in many textbooks.⁸⁴ The treatment of the radiation as an electric field without practical spatial variation on a molecular/local scale and eliminating magnetic parts leads to the Fermi Golden Rule for the X-ray cross-section:

$$\mu(E) = K|\langle\phi_f|e\cdot\vec{r}|\phi_i\rangle|^2 \delta_{E_f-E_i+h\nu} \quad (2.1.2.a)$$

The intensity of the absorption process is then proportional to the square of the transition matrix element connecting the initial (ϕ_i) and final (ϕ_f) states times a delta function, which ensures the fulfillment of the conservation energy theorem. The elimination of the spatial dependence of the electric field corresponds to a series expansion of its $e^{2\pi z/\lambda}$ dependence up to the first term (linear dependence in r , equation 2.1.2.a); this yields the dipole approximation of the interaction energy between the atom electronic cloud and the X-ray radiation field. Better approximations will include quadrupole, octapole, and so forth terms.

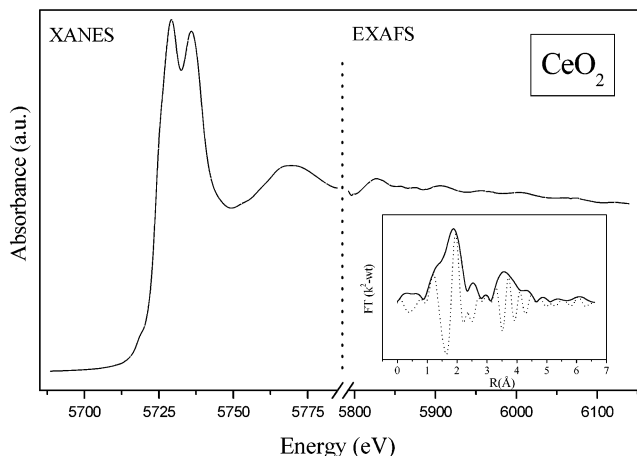


Figure 4. Ce L_{III} absorption spectrum of fluorite CeO₂. Inset: Fourier transform of the EXAFS spectrum.

However, except in few cases, some of them here detailed, the dipole approximation gives quantitative analysis of the XANES shape.

An important approximation is to assume that the matrix element can be rewritten into a single-electron matrix element. This is based in the sudden approximation, which allows reordering the transition element in 2.1.2.a in terms of a overlap term of the $N - 1$ "inactive" electrons, which is roughly independent of energy, and the mentioned single-electron matrix element connecting wave functions of the unbound and inner-core electrons.⁸⁵ The validity of the sudden approximation depends primarily on the photoexcited electron kinetic energy and has been the subject of many studies.^{79,82,84} All electron rearrangements (interatomic and mainly extra-atomic relaxation of valence electrons) in response to the core-hole creation are thus neglected, the series of delta functions corresponding to different final states identifies with the local density of states (ρ),⁸⁶ and the corresponding X-ray absorption cross-section becomes:

$$\mu(E) = K|\langle\phi_f|e\cdot\vec{r}|\phi_i\rangle|^2 \rho \quad (2.1.2.b)$$

where $\phi_{i,f}$ correspond to the mentioned initial and final mono-electronic wave functions. The dipole matrix element dictates that the local density of states has an orbital moment that differs by 1 from the core state ($\Delta L = \pm 1$), while the spin is conserved ($\Delta S = 0$).

There are two XAS techniques: X-ray absorption near edge spectroscopy (XANES) and extended X-ray absorption fine structure (EXAFS). They differ in the energy of the final electronic state sampled which is limited to a maximum of about 40–50 eV for XANES and above that point for EXAFS (Figure 4). Intuitively, it is obvious that pure electronic information (e.g., chemical bonding information) is only enclosed in the low-lying extended states and is thus confined to the XANES region. This will be discussed in section 2.2.1. On the other hand, at high energy in the continuum of electrons participating in EXAFS, the effect of neighboring atoms becomes small and electron states approximate to spherical waves that

are simply scattered by such atoms. The information extracted is thus of geometrical local character.

As a general rule, eqs 2.1.2.a and 2.1.2.b can be solved by using modern quantum-mechanical methods. Two general approaches are discerned. The first one employs *ab initio* or DFT methods to calculate the initial and final wave functions of the electronic transition. The second reformulates the Schrödinger equation in terms of the scattering theory and allows one to write the absorption equation as a correlation function. This latter is particularly useful for EXAFS analysis of nanostructured materials as they can be treated as clusters for calculations which, in turn, can be performed in steps of growing size, showing the effect of introducing different coordination spheres. Detailed accounts for the multiple scattering EXAFS theory can be found in refs 87 and 88. Using this theoretical framework, the EXAFS formula can be written as:

$$\chi(k) = S_0^2 \sum_i \frac{N_i F(k)}{k R_i^2} e^{-2R_i/\lambda(k)} e^{-2DW} \sin(2kR + \phi(k)) \quad (2.1.2.c)$$

This was originally proposed by Sayer et al.,⁸⁹ based on a single-scattering formalism but can be generalized to represent the contribution of *N* equivalent multiple-scattering contributions of path length $2R$.⁸⁸ It can be thus considered the standard EXAFS formula, providing a convenient parametrization for fitting the local structure around the absorbing atoms. The dependence of the oscillatory structure on interatomic distance and energy is reflected in the $\sin(2kR)$ term. The decay of the wave due to mean free path or lifetime (including intrinsic core-hole and extrinsic inelastic losses) is enclosed in the exponential $2R/\lambda$, which is largely responsible for the relatively short range probed by EXAFS in a material. As early recognized in ref 89, the sinusoidal nature of the EXAFS phenomenon allows a Fourier analysis of the signal (inset in Figure 4), yielding key information to give initial guesses for the fitting parameters. The strength of the interfering waves depends on the type and number (*N*) of neighboring atoms through the backscattering amplitude ($F(k)$), which largely dictates the magnitude of the signal. The phase function ($\phi(k)$) reflects the quantum-mechanical wavelike nature of backscattering which depends on both the absorber and the scatterer atom properties.^{79,81}

Another important factor is the Debye–Waller factor e^{-DW} . This accounts for thermal and static disorder effects concerning the movement/position of atoms around their equilibrium/averaged position. A point to stress is that the nature of this term is different to the counterpart term in XRD.⁹⁰ Since vibrations increase with temperature, EXAFS spectra are usually acquired at low temperature to maximize information. Spectra at different temperatures may, on the other hand, allow one to determine thermal and static contributions to DW. The DW term smears the sharp interference pattern of the sinusoidal term and cut off EXAFS at sufficiently large energy beyond ca. 20 \AA^{-1} . Important to stress is that the DW factor

is in fact a complex mathematical function and has a natural cumulant expansion in powers of *k*. The amplitude of the e^{-DW} factor contains even moments $DW(k) = 2C_2k^2 - (2/3)C_4k^4 + \dots$ while odd moments contribute to the EXAFS phase $\phi(k) = 2c_1k - (4/3)C_3k^3 + \dots$ ⁹¹ While the fitting of bulk systems makes use up to the squared term of the *k*-series expansion, the point is that the k^3 behavior (third cumulant) is important for “disordered” systems; as surface atoms have a less symmetric environment with respect to bulk ones and correspond to a significant part in nanostructured materials, the cumulant expansion needs to be considered in analyzing EXAFS data. Inclusion of the third cumulant would mainly influence coordination distance, while the fourth would influence the coordination number and/or (second order) Debye–Waller factor.

Effect of Nanostructure. EXAFS analysis of oxides as a function of size are scarce and mainly devoted to study Ti,^{92–94} Y,⁹⁵ Zr,^{58,95} and Ce^{96–98} containing systems. A point to stress is that, as mentioned throughout the text, nanocrystalline phases prepared by chemical methods are commonly accompanied by amorphous ones,^{58,59} and different techniques may in fact be selective to one of them (XRD) while others (as XAS) inform over the whole system. Analysis of the EXAFS data of nanostructured oxides which account for the relative asymmetric (anharmonic) pair distribution of bond distances are even more scarce and exclusively devoted to Ti and Ce oxide systems.^{99,100} This however has been frequently worked out for nanostructured chalcogenides¹⁰¹ and has been studied in detail for nanostructured fcc metals.¹⁰² As metal oxides display a multitude of different crystal structures,⁶ no general correlation between EXAFS coordination numbers of the three or four first shell coordination numbers and average particle size/morphology has been published. This can be found for fcc metals¹⁰³ and might be generalized to certain oxide cubic structures. It can be however noted that first shells display coordination numbers (CN) close to bulk ones, differing typically only by one unit as undercoordinated atoms complete their first coordination shell at surfaces by using hydroxyl groups or water molecules (see below). Second and further shells display CNs departing from bulk values, but their analysis is structure and shape dependent. A point to mention is that in some cases, such as ZrO₂ oxides, coexistence of two crystalline (or one amorphous) phases can lead to destructive interference effects and misleading interpretation of results.¹⁰⁴ Although EXAFS studies of dispersed surface species are not the main target of this review, it can be mentioned here that revisions of related papers can be found in ref 105.

For titanium oxides, the studies usually identify the presence of 5-fold-coordinated species in the nanostructured anatase and rutile surfaces, with a shortening of the Ti–O first shell bond distance,^{92,93} which in some cases is identified as a result of the presence of Ti hydroxyl groups at the surface.⁹² Note however that the inclusion of the third cumulant for studying mesoporous (amorphous by XRD but with a surface local structure similar to nanostructured

anatase) titania suggests a larger Ti–O average first coordination distance with respect to the rutile/anatase phase.¹⁰⁰ The presence of surface hydroxyl-coordinated centers has been also mentioned in ZrO₂ but detected by using other techniques.⁵⁸ As will be discussed in section 3.2, the case of cerium-containing nanostructured oxides is still under study because the series of samples with increasing size are obtained by calcining at progressively higher temperatures solids from Ce(III) precursors, and this influences the presence and concentration of two oxidation states Ce(III)/Ce(IV) in materials with small particle size.^{29,96,97}

Geometrical information is also enclosed in the XANES spectrum. The energy position of the peaks corresponding to electronic transitions to final quasi-bound, continuum states (called continuum resonances, CRs, in solid-state physics) depends on both electronic and geometrical factors.^{78,84,106} Electronic factors are analyzed in section 2.2.1. Geometrical factors are summarized in the so-called $1/R^2$ rule, which states that the quantity $\Delta E/R^2$ is a constant, where ΔE refers to the energy difference between the CR energy position and the zero electron kinetic energy and R is the nearest neighbor distance. This rule has been used fruitfully in solid-state studies, but a paper by Kizler¹⁰⁷ demonstrates limitations in its applicability. Essentially, this rule can be used with generality only for CRs dominated by scattering from first or second nearest neighbors.

2.1.3. Raman Spectroscopy

Raman spectroscopy is a powerful tool to analyze structural/morphological properties of solid oxides at a local level, given the strong sensitivity of the phonon characteristics to the crystalline nature of the materials.¹⁰⁸ The theoretical basis for the application of this technique to the study of the properties of extended crystals as well as of individual molecular complexes present at the surface of oxide materials is out of the scope of the present work and can be found in different textbooks or review articles.^{109,110} Raman spectroscopy is a bulk sensitive technique, but the use of excitation frequencies allowing charge-transfer band absorption (Resonance Raman) allows some surface sensitivity, as briefly outlined for several oxides in section 3. Essentially, the theoretical background for the study of nanocrystalline (considered as a whole as crystalline materials) oxides as well as the spectral consequences observed by Raman is provided by the phonon confinement model that will be briefly analyzed in a first part; complete details of this model can be found elsewhere.^{111–113} The study by Raman spectroscopy of other properties that can in some cases be linked to the nanoscopic nature of the oxide materials, like the existence of disorder associated to the presence of lattice defects (see also section 2.1.1) or surface phonons, will be described later.

Phonon Confinement Model. The model employed for analyzing the features observed in the Raman spectra of nanocrystalline materials is the so-called “phonon confinement” (or “spatial correlation”) model.^{111–114} Within such model, nanocrystalline

materials can be considered as an intermediate case between that of a perfect infinite crystal and that of an amorphous material. Thus, in a perfect crystal, conservation of phonon momentum (q) during phonon creation or decay upon interaction with the external radiation field requires that, in first-order Raman scattering, only optic phonons near the center of the Brillouin zone ($q \approx 0$) are involved. In amorphous materials, due to the lack of long-range order, the q vector selection rule does not apply and the Raman spectrum resembles the phonon density of states. In the intermediate case of nanocrystalline materials, due to the uncertainty principle, a range of q vectors of the order $\Delta q \approx 1/L$ (where L is the particle size) can be involved in the Raman process.^{111–114} The approach employed in the phonon confinement model follows from the work by Richter et al.,¹¹¹ which shows that the relaxation of the conservation of phonon momentum selection rule arises from substitution of the phonon wave function in an infinite crystal by a wave function in which the phonon is confined in the volume of the crystallite. In their approach, which is employed to explain the first-order Raman spectrum of microcrystalline spherical silicon particles, it is used a Gaussian function to impose the phonon localization. Later, Campbell and Fauchet extend the model by using other confinement functions and considering different shapes for the nanocrystallites (spherical, columnar, or thin films).¹¹³ They found that the Raman spectrum of different semiconductor nanocrystals is best explained by using a Gaussian confinement function similar to the one employed by Richter et al., although with lower amplitude at the boundaries. By using this model, the first-order Raman spectrum is, considering the general case of a Gaussian confinement function with phonon amplitudes at the borders depending on a confinement parameter β ,^{111–114} given by

$$I(\omega) \cong \int_{BZ} \frac{d^3 q \exp(-q^2 L^2/8\beta)}{(\omega - \omega(q))^2 + (\Gamma_0/2)^2} \quad (2.1.3.a)$$

where the integration is carried out over the entire Brillouin zone in the corresponding symmetry directions, $\omega(q)$ is the phonon dispersion curve and Γ_0 is the natural line width. In the case of an infinite crystal ($L \rightarrow \infty$), $I(\omega)$ is a Lorentzian centered at ω (the Raman frequency) with a line width of Γ_0 . Application of eq 2.1.3.a to any given Raman line of the perfect crystal results, as experimentally observed,^{111–115} in frequency shifts and asymmetric broadenings that increase with decreasing the particle size of the nanocrystal, and of a sign and magnitude that depend on the form and dispersion of the $\omega(q)$ function. Thus, a negative/positive dispersion in ω values as q increases is expected to produce asymmetric low/high-frequency broadening and a red/blue shift of the peak.

Examples on the application of the phonon confinement model to the analysis of Raman lines in nano-sized TiO₂ and SnO₂ materials^{57,116} are shown in Figure 5; similar analyses successfully applied to the study of Raman lines in ZrO₂ or ZnO nanoparticles are found in the literature.^{116,117} In the general case,

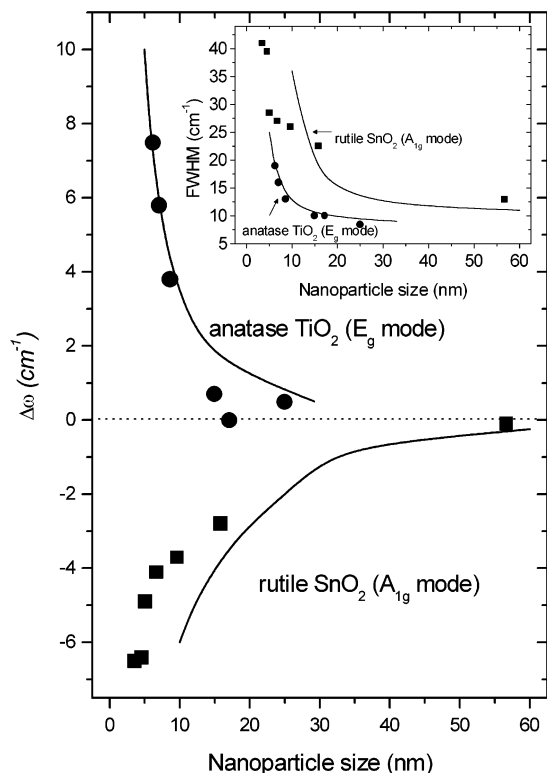


Figure 5. Experimental values (points) and values calculated according to the phonon confinement model (lines) for the Raman shift with respect to the large crystal value for peaks at 142 cm^{-1} of anatase TiO_2 (E_g mode) and 638 cm^{-1} of rutile SnO_2 (A_{1g} mode) as a function of the particle size. The evolution of the corresponding peaks widths is shown in the inset (experimental: points; calculated: lines); as inferred from the model, a high/low-frequency asymmetry was also observed with decreasing the particle size for the $142/638\text{ cm}^{-1}$ peaks. The figure was constructed with data extracted from refs 57, 115, and 116.

a qualitative approach to the model is used to explain the evolutions of Raman peaks with decreasing the size of the nanoparticles. In this sense, it must be considered that in addition to the uncertainty in the choice of the confinement function and phonon dispersion curves (in the absence of precise theoretical or experimental results by neutron inelastic scattering), the presence of nonuniform particle size distributions or of imperfect crystallites (further confining the phonons by the microdomain boundaries or defects) often leads to resorting to empirical correlations for the analysis.^{57,115–123} Some examples of application of the confinement model for qualitative interpretation of Raman results in series of nanostructured oxides such as anatase TiO_2 , CuO , Cr_2O_3 , ZrTiO_4 , or manganese oxides can be found elsewhere.^{118–124}

In some cases, refinement of the model by including effects of defects or more precise consideration of particle size distributions leads to closer approaches to the experimental results, as shown by Spanier et al. for CeO_2 nanoparticles.¹¹⁴ Thus, the analysis of the 3-fold degenerated F_{2g} peak at 465 cm^{-1} (the only one allowed in first order) in CeO_2 nanosized samples with multidisperse size distributions requires consideration of both the effects of the presence of the vacancies (proposed to increase with decreasing

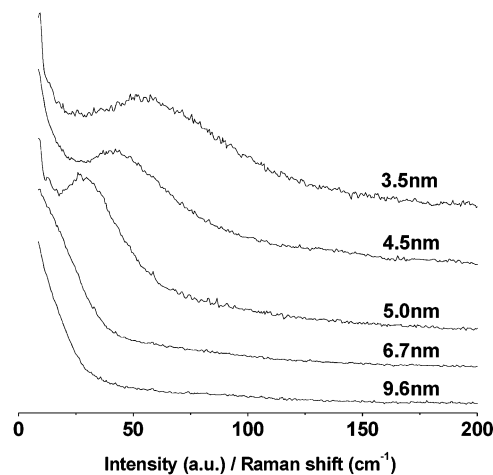


Figure 6. Acoustic modes observed in the Raman spectra of SnO_2 nanoparticles as a function of the particle size (courtesy of Dr. A. Diéguez).

particle size, at least for sizes below ca. 3 nm)¹²⁵ and the associated change in lattice dimensions. While the former, according to experimental evidence, is expected to give rise to blue shifts of the peak, this is compensated by the red shift produced upon lattice expansion (Δa), in accordance with the equation:

$$\Delta\omega = -3\gamma\omega_0(\Delta a/a_0) \quad (2.1.3.b)$$

where ω_0 is the F_{2g} frequency in pure stoichiometric CeO_2 , a_0 is the CeO_2 lattice constant, and $\gamma = (B/\omega) \cdot (d\omega/dP)$ is the Grüneisen constant with B the bulk modulus and $d\omega/dP$ the linear shift of the frequency with hydrostatic pressure.¹²⁶ The result is that the red shift and broadening observed in the Raman line is significantly larger than expected from the phonon confinement model and adequate fitting of the experimental spectra is only obtained when jointly considering the effects of inhomogeneous strain (associated with the dispersion in lattice constants as a consequence of the presence of vacancies and reduced cerium centers)¹²⁵ and phonon confinement.¹¹⁴ A similar approach has been employed to explain qualitatively the shifts observed in the main band of Ce–Tb mixed oxide nanoparticles as a function of the terbium content.¹²⁷ Another effect of the presence of oxygen vacancies in the CeO_2 nanoparticles is the appearance of a new broad peak at ca. 600 cm^{-1} that can be related to a second-order phonon or a local mode centered on the vacancy positions.^{114,126,128} The presence of second-order peaks associated with nanostructured configurations has been also reported for ZrO_2 .¹²⁹

Observation of Acoustic Modes. Another possible consequence of decreasing the particle size in the nanosized oxides is the appearance of low-frequency bands associated with acoustic modes. An example is the study performed on SnO_2 , which, for particles from 3.7 to 9.5 nm of average size, displays a peak from ca. 15 to 60 cm^{-1} that shifts to higher frequency and becomes less intense and broader with decreasing the particle size (Figure 6 shows the spectrum obtained under typical backscattering geometry of the spectrometer; note that correction of Bose-Einstein phonon occupation factor required for

the analysis is not included).¹³⁰ Analysis of such peak considers the vibration of the nanoparticle as a whole. Thus, the nanoparticle is considered as an elastic body of spherical shape with two types of vibrational modes, spheroidal and torsional. Then, after considering different boundary conditions (rigid or stress free), one arrives at expressions for estimating the frequency of the vibration as a function of the particle size of the type:¹³⁰

$$\omega = \frac{S_{l,t} v_{l,t}}{Lc} \quad (2.1.3.c)$$

where $v_{l,t}$ is one of the two sound velocities (v_l for spherical or longitudinal and v_t for torsional or transversal vibrations) in the bulk of the oxide, $S_{l,t}$ is a coefficient that depends on the sound velocities and c is the vacuum light velocity. As an interesting application of this analysis, nondestructive estimation of the particle size distribution can be done with this model after selecting the most adequate theoretical condition and applying it to deconvolute the experimental spectrum.¹³⁰ Similar analyses have been applied to explain the presence of acoustical phonon modes in ZrO_2 nanoparticles.¹³¹

Other Spectral Consequences of Nanostructure. An obvious consequence of decreasing the particle size is that a relatively large fraction of atoms in the nanoparticle reside on the surface and, as a result, surface optical phonons can also be observed with measurable intensity and analyzed by Raman spectroscopy (in addition to high resolution electron energy loss spectroscopy and helium atom scattering techniques, most typically used for this purpose). An interesting application for this purpose is the use of resonant Raman spectroscopy tuned to the surface region, taking advantage of the different band structures of bulk and surface.¹³² The appearance of new vibrations (ascribed to surface phonon modes) different than those observed for the bulk material and increasing their relative intensity with decreasing the particle size has been observed in different oxide systems.^{57,129,133} A classical model is usually employed to analyze such surface phonons. According to the classical optical dispersion theory, each vibrational motion is characterized by an independent harmonic electric dipole oscillator with the corresponding transverse optical (TO) and longitudinal optical (LO) phonon modes. The frequency corresponding to the surface phonon modes must lie between ν_{TO} and ν_{LO} of any determinate TO–LO pair and satisfies the following condition:

$$\nu^2 = \nu_{\text{TO}}^2 \left[\frac{\epsilon_0 + \epsilon_m(1/L_k - 1)}{\epsilon_\infty + \epsilon_m(1/L_k - 1)} \right] \quad (2.1.3.d)$$

where ϵ_0 , ϵ_∞ , and ϵ_m are dielectric constants for the material (static and high-frequency ones) and the surrounding medium and L_k are depolarization factors that depend on the particle shape. Full details of this theoretical approach and its successful application to the analysis of SiO_2 surface modes can be found elsewhere.¹³⁴

2.1.4. TEM and STEM

Transmission electron microscopy (TEM) is one of the most powerful and versatile techniques for the characterization of nanostructured systems. Its unique characteristics allow one to achieve atomic resolution of crystal lattices as well as to obtain (with the assistance of energy-dispersive X-ray spectroscopy (EDS) and electron energy-loss spectroscopy (EELS) complementary techniques) chemical and electronic information at the sub-nanometer scale. Numerous monographs have addressed technical or theoretical aspects involved in modern TEM microscopy employed for characterization of nanostructured systems as well as particular applications in different fields (see, for instance, refs 135–144 and references therein). The vast extension of the field precludes giving an exhaustive treatment here, and only a brief outline of fundamental aspects of the TEM application to characterization of nanostructured systems will be thus attempted. As it is well known, the interaction of an electron beam with a solid specimen results in a number of elastic or inelastic scattering phenomena (backscattering or reflection, emission of secondary electrons, X-rays or optical photons, and transmission of the undepleted beam along with beams deviated as a consequence of elastic – single atom scattering, diffraction – or inelastic phenomena). The TEM technique is dedicated to the analysis of the transmitted or forward-scattered beam. Such a beam is passed through a series of lenses, among which the objective lens mainly determines the image resolution, to obtain the magnified image. In low-resolution TEM, the objective aperture will be adjusted for selection of the central beam (containing the less-scattered electrons) or of a particular diffracted (or scattered in any form) beam to form the bright-field or dark-field image, respectively. In high-resolution TEM (HRTEM), which is usually performed in bright-field mode, the image is formed by collecting a few diffracted beams in addition to the central one.

Analysis of contrasts observed in the experimental TEM images when using the central beam by intercepting the electrons scattered through angles larger than a selected objective aperture is usually done on the basis of amplitude (or scattering) and mass thickness or atomic number contrast theories.^{135,136} Figure 7 shows a typical example of a bright-field image collected in this mode.^{145,146} The higher contrast resolution usually attained in dark-field with respect to bright-field images can be most useful to analyze particle size or shape of the nanoparticles; an interesting example in this sense has been shown in a work by Yin and Wang in which the tetrahedral shape of CoO nanoparticles is assessed from contrast analysis in dark-field images.¹⁴⁷ On the other hand, interference between the scattered and the incident wave at the image point is usually analyzed in terms of the phase contrast theoretical approach, which is employed for interpretation of HRTEM images.^{135–139} As a result of interaction with the specimen, the incoming electron wave is modified into a transmitted electron wave whose function $\psi(x,y)$ contains information (the electron wave exiting from the specimen

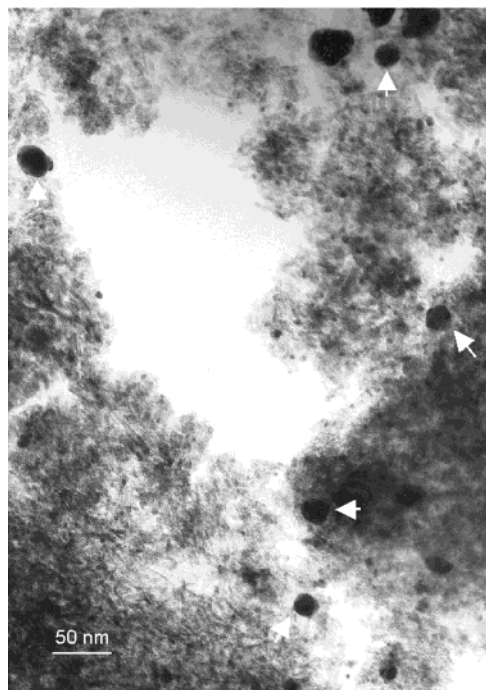


Figure 7. Bright-field TEM picture of a Ag/Al₂O₃ catalyst. The darkest zones (some of them marked with arrows) appear as a consequence of the higher scattering power of silver and are attributed (on the basis of analysis with other techniques) to oxidic silver nanoparticles. Thickness contrast is also revealed by comparing contrast in different zones in the picture. From ref 145 and 146. Copyright 2000 and 2003 Elsevier Science.

can be approximated as $\psi(x,y) = \exp[i\sigma V_p(x,y)]$, being $V_p(x,y)$ the electrostatic potential of the specimen projected in the x,y plane and σ an interaction constant^{135–139} on the structural details of the sample. Extraction of such information by formation of an image at the detector requires further interaction of the transmitted beam with the series of lenses constituting the microscope optics, in such a way that the observed image intensity distribution ($I(x,y) = |\psi_m(x,y)|^2$) is correlated with $\psi(x,y)$ through a function T that contains instrumental parameters (like apertures, wave attenuations, defocus and spherical aberration coefficient of the objective lens, etc.), according to^{135–139}

$$\hat{\psi}_m(u,v) = \hat{\psi}(u,v)T(u,v) \quad (2.1.4.a)$$

where $\hat{\psi}_m(u,v)$ represents the Fourier transform of the wave function after the lenses, $\hat{\psi}(u,v)$ is the Fourier transform of $\psi(x,y)$, and u,v are coordinates of the reciprocal space vector.

To take into account the influence of the different parameters affecting the contrasts observed in the experimental images (electron scattering by the sample, particularly influences of irregular, columnar, etc. disposal of the scatterers, lens imperfections, microscope instability, etc.), HRTEM quantitative analysis is usually based on matching experimental and calculated images, for which various computational methods have been developed.^{135,137,141,142,148,149} Figure 8 shows an example of application of simulated images to resolve geometrical aspects in a supported oxide system.¹⁴¹

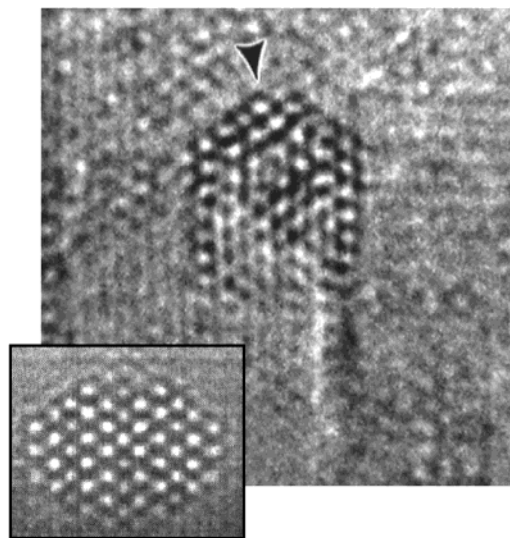


Figure 8. HRTEM image of a Nd₂O₃/MgO catalyst and simulation (left bottom) of the Nd₂O₃ nanoparticle appearing in the experimental image (marked with an arrow). The best match is observed to correspond to a rounded, unstrained, monolayer raft of cubic Nd₂O₃ in [001] orientation grown under parallel orientation over a (001) MgO surface. (Courtesy of Dr. J. J. Calvino).

Resolution limits of the TEM technique and schemes to achieve sub-angstrom resolution have been analyzed in detail by Spence.¹³⁷ The highest structural resolution possible (point resolution) when the obtained images can be directly related to the projected structure of the specimen is given by the Scherzer expression $R_s = 0.66 \lambda^{3/4} C_s^{1/4}$, where λ is the electron wavelength and C_s is the spherical aberration coefficient.¹³⁷ From this expression and considering the de Broglie formula, higher resolution is achieved upon use of high-voltage instruments (acceleration voltages higher than 0.5 MeV). Enhanced radiation damage, which may have stronger effects for nanostructured materials,¹³⁹ must however be considered in that case. Aberration correction has in turn allowed one to achieve sub-angstrom resolution with microscopes operating at lower voltages (typically, 200 keV), allowing the resolution of oxygen atoms in oxides materials.^{137,143} On the other hand, considering that high resolution is achieved in TEM as the result of electron wave interference among diffracted peaks, a limitation to structural resolution can also arise from decreasing the number of atoms in the nanoparticle.¹³⁹ This also can pose limitations to routinely employed determination of particle size distributions, particularly in cases when contrast differences between various sample components are not clearly resolved, as may occur for supported catalysts.¹⁴⁹ Considering that such estimations are both microscope and sample dependent, calculations are generally required to establish limitations in contrast resolution in each particular case.^{149,150}

As mentioned above, information on chemical and electronic characteristics of the nanocrystals at a high spatial resolution is also achievable with TEM instruments. The use of scanning transmission electron microscopy (STEM) in which a fine convergent electron probe is scanned over the sample (the resolution being related to the probe size that can be as small

as $\approx 0.1 \text{ nm}$)¹⁴³ is particularly useful for this purpose.^{135,136,139,147,151} The electrons kinetic energy losses or the X-rays emitted as a consequence of inelastic scattering processes during electron–specimen interaction can be analyzed by EELS and EDS techniques, which are the two most commonly used in chemical microanalysis. Due to EDS limitations in detection of light elements, EELS is most employed for the analysis of oxide materials. In addition to elemental information, the EELS spectra provide information on the electronic structure, bonding, and nearest neighbor distribution of the specimen atoms. Among the different loss regions, the one most useful for this purpose is the high-loss one, related to electrons that have interacted with inner-shell or core electrons of the specimen atoms. Thus, the information obtained is similar to that given by XAS (see above), i.e., K-, L-, M-, etc. ionization edges of the elements present in the sample appear in the EELS spectrum (near edge and extended energy-loss fine structure, ELNES and EXELFS, regions being defined within them). A generally higher energy resolution is however achieved with EELS, which comparatively facilitates analysis of the states present in a determinate band.¹³⁹

In connection with this, TEM images can be also formed with electrons that have lost a specific energy with respect to a determinate energy threshold of the atomic inner shell, giving rise to energy-filtered TEM (EF-TEM). A chemical mapping at the nanoscale can be obtained in this mode, which allows resolving the location of the corresponding elements in the samples, being most useful in cases when small contrast differences between different sample components are observed in the bright-field images; in addition, differences observed in the EELS spectra as a function of the valence state of a determinate element can be exploited by EF-TEM for getting valence state distributions across the specimen.^{139,147}

On the other hand, collecting the electrons scattered at high angles in a STEM instrument (by means of a high-angle annular dark field detector, HAADF) has proven most useful to obtain images (by the so-called Z-contrast imaging) of small clusters in catalysts or even single (relatively heavy) atoms or point defects.^{143,144} Considering the Mott formula for the electron scattering factor of a single atom ($f_e(s) = e[Z - f_x(s)]/16\pi^2\epsilon_0s^2$, being $s = \sin \theta/\lambda$, f_x is the X-ray scattering factor of the atom, θ is the scattering angle, and λ is the electron wavelength), it is inferred that the electrons collected at high angles give significant information directly related to the atomic number. Another application of high utility in the analysis of materials, and in which significant progress has been achieved during the last years, is in-situ TEM.^{143,152,153} Recent advances in this field are collected in the review of Wang.¹⁴³

2.1.5. STM and AFM

Since the 1980s, STM and STM-derived local probe methods have experienced a remarkable development. The seminal ideas behind these microscopies can be traced back to the early 1970s with the invention of the topographiner.^{154,155} Ten years later,

Binnig and Rohrer established the basic principles for STM.^{156,157} For this important contribution, they received the 1986 Nobel prize in physics. In a scanning tunneling microscope, the sample surface is scanned with a sharp tip located at a distance of less than a few nanometers.¹⁵⁸ The tip is mounted on a piezoelectric positioner. A voltage is applied between the sample and tip, generating a tunneling current that varies exponentially with separation.^{156,158} The tunneling current is then measured, and a feedback control system compares the actual tunneling current with a (user-adjustable) “set current”. If the actual current is too large or too small, the feedback control system moves the tip back or forward (respectively). In a first approximation, the movement of the tip represents variations in the position of the atoms in the surface of the sample. The 2D array of numbers representing the surface “height” at each point is recorded in a computer, displayed on the computer screen, and then stored on a magnetic or optical device for subsequent analysis.¹⁵⁸

Several approaches have been proposed for the analysis of STM images.^{159–164} In general, there is a relationship between the STM image and geometric and electronic properties of the surface of a sample. A precise interpretation of the image at an atomic scale can be a problem^{157,163,164} because the image is not at all a steric representation of the surface but is a view of its electronic structure at the Fermi level energy. In most cases, it is therefore not possible to directly and simply relate the bumps and shapes of the STM image to the actual lateral positions of atoms.¹⁶⁴ One must establish how the structural parameters affect the tunneling current and formation of the image.^{165,166} A good knowledge of the electronic structure of the surface and tip is a prerequisite for the calculation of the tunneling current. To obtain this electronic structure, different quantum-mechanical approaches can be used ranging from the extended Hückel method to calculations based on density functional theory.^{159,164} Various levels of approximation have been proposed for the calculation of the tunneling current.^{159–165}

Many of the methods used to calculate the current rely on perturbation theory.^{167–171} Following this formalism, the current between two electrodes (represented by μ and ν) can be described as¹⁵⁸

$$I = (2\pi|e|/h) \sum_{\mu,\nu} [f(E_\nu) - f(E_\mu)] |M_{\mu\nu}|^2 \delta(E_\nu + |e|V - E_\mu) \quad (2.1.5.a)$$

In this equation, $f(E_\nu)$ represents the Fermi-Dirac distribution function (the first factor in the summation reflects the fact that electrons must tunnel from an occupied electronic state to an unoccupied electronic state); $M_{\mu\nu}$ represents the tunneling matrix element between state μ on the sample and state ν on the tip. The δ -function term reflects energy conservation during the tunneling process. The calculation of $M_{\mu\nu}$ is not trivial.^{158,159,164} In the early work of Tersoff and Hamann, an s-wave was assumed for the tip,¹⁶⁰ but in subsequent studies tunneling matrix

elements have been calculated with p and d states as tip orbitals.¹⁵⁰ A single metal atom and clusters have been used to model the tip.^{167–171}

When using perturbation theory, the tip and the surface are treated separately, neglecting any interaction between them. Technically, this is valid only in the limit of large tip to surface distances. Methods have been proposed for the calculation of the tunneling currents that take into account interactions between the tip and sample through a scattering theory formalism.^{172,173} In principle, the tunnel event is viewed as a scattering process:¹⁶⁴ incoming electrons from the sample scatter from the tunnel junction and have a small probability to penetrate into the tip, and a large one to be reflected toward the sample. Multiple scattering events can affect the current.^{174,175} Tip-induced localized states and barrier resonances seem to play an important role in the conductance.^{176,177}

Although it may not be easy to obtain structural parameters from STM images, this microscopy can be used in a straightforward way to study the shape or morphology of oxide nanostructures as a function of temperature and under reaction conditions.^{178–183} Figure 1 illustrates how useful this technique can be.²³ Initially, Mo nanoparticles are present on a Au(111) substrate. There is Au–Mo intermixing and the nanoparticles are tridimensional. Upon oxidation and formation of MoO₃, the STM image shows a radical change in the morphology of the system. There is no more Au–Mo intermixing and 2D aggregates of MoO₃ spread out over the Au(111) substrate.²³

The dependence of STM images on applied bias can be utilized as the basis for a true atomic-resolution tunneling spectroscopy.^{158,159,181} The effects of the voltage on the tunneling current depend on the electronic properties of the sample and, thus, information can be obtained about local density of states and band gaps.¹⁸⁴ Tunneling spectroscopy data can be compared directly with area-averaging probes of electronic structure such as photoemission and inverse photoemission spectroscopies.^{185,186} Since the tunneling data can be acquired with atomic resolution, one could be able to directly visualize the spatial distribution of individual electronic states.^{185,186}

In atomic force microscopy (AFM), a tip is mounted on a cantilever.^{158,159} Forces exerted by the sample on the tip bend the cantilever, and this deflection is used in a feedback system in a manner analogous to the tunneling current in the STM. The forces relevant to AFM are of electromagnetic origin.¹⁸⁷ In the absence of external fields, the dominant forces are van der Waals interactions, short-range repulsive interactions, adhesion, and capillary forces.¹⁸⁷ The interaction between the tip and sample can be operated on either the attractive or repulsive parts of the interatomic potential curve. Most experiments for contact AFM are performed on the steeply rising repulsive part of the potential curve.¹⁵⁸ Operation in the attractive region is intrinsically more difficult because it involves weaker interactions and requires the measuring of both the force and force gradient.¹⁵⁸ However, true atomic resolution is easier to achieve

using attractive-mode contact AFM.^{158,159} Images obtained with repulsive-mode contact AFM may show atomic periodicity while not truly achieving atomic resolution.

In the past decade, AFM have experienced a significant transformation by using a vibrating probe to explore the surface morphology.¹⁸⁷ Dynamic or noncontact AFM methods are emerging as powerful and versatile techniques for atomic and nanometer-scale characterization.^{158,159,187} In dynamic AFM, there are two major modes of operation:^{188–190} amplitude modulation and frequency modulation (AM-AFM and FM-AFM, respectively). Using FM-AFM, images with very good atomic resolution have been obtained for semiconductors and insulator samples.^{191–193} Because AFM does not involve the induction of a tunneling current between the probing tip and sample, it can be applied to study oxide systems that have a low conductivity (insulators or wide band-gap semiconductors).^{194,195}

To obtain structural parameters from AFM images one must model the movement of the cantilever over the sample in an accurate way.^{159,187} To gain insight into the tip motion, several authors have considered the cantilever-tip ensemble as a point-mass spring, and thus the movement can be described by a nonlinear, second-order differential equation:^{196–198}

$$m\ddot{l} + k\dot{l} + (m\omega_0/Q)\dot{l} = F_{ts} + F_0 \cos(\omega t) \quad (2.1.5.b)$$

where F_0 and ω are the amplitude and angular frequency of the driving force. Q , ω_0 , and k are the quality factor, angular resonance frequency, and the force constant of the free cantilever, respectively. F_{ts} contains the tip–surface interaction forces. In the absence of tip–surface forces, eq 2.1.5.b describes the motion of a forced harmonic oscillator with damping.¹⁸⁷ The mathematical expressions for F_{ts} in general can be complex and contain terms for long-range attractive interactions, short-range repulsive interactions, adhesion, and capillary forces.¹⁸⁷

2.2. Analysis of Electronic Characteristics

2.2.1. XANES

As already discussed in section 2.1.2, XANES spectroscopy probes the electronic state of an absorbent atom of the X-ray radiation. The two XAS techniques are sensible to local order, making them especially suitable for analyzing nanostructured materials, but they differ in the fact that XANES is essentially not affected by thermal effects; in the absence of vibronic or specific (nonfrequent) cases of spin–orbit coupling, the recording temperature does not affect the XANES shape.^{79–81,106} Recent work on XANES concerning nanostructured oxides has been published for Al,¹⁹⁹ Mg,²⁰⁰ Ti,^{92,93,201,202} V,²⁰³ Fe,^{204–206} Ni,²⁰⁷ and Ce.^{96,98,208} containing systems, while older work is summarized in refs 106 and 107. These studies showed that bulk XANES shape is typically reached by clusters of around 80–100 atoms and, thus, solids with a typical dimension below 4 nm show a characteristic, distinctive XANES shape. This happens because, in terms of the scattering theory,

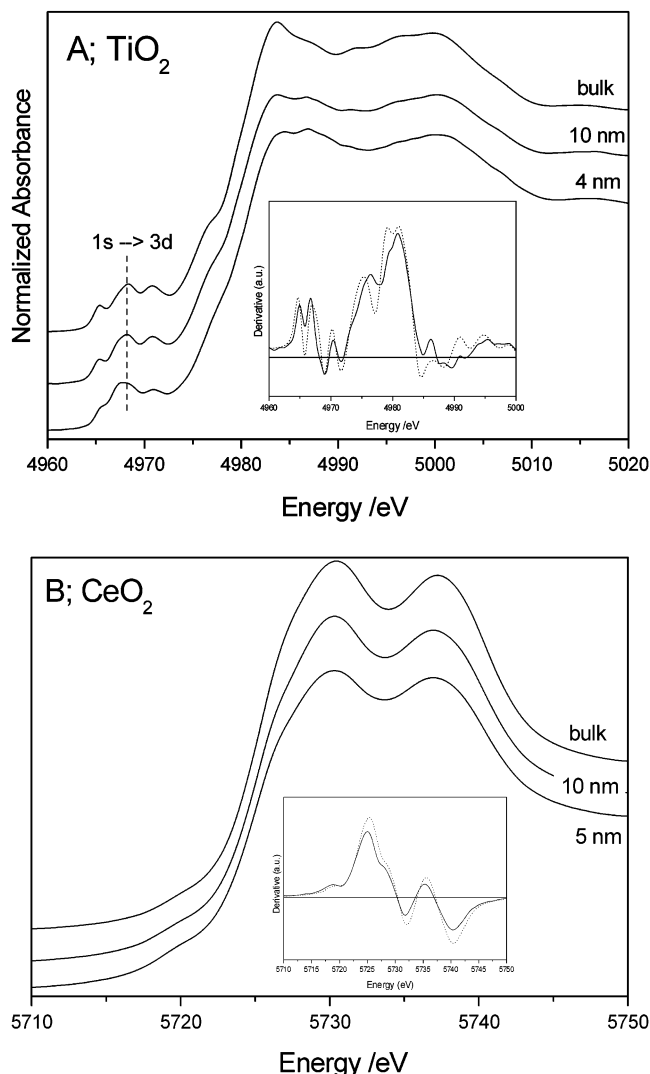


Figure 9. (A) Ti K-edge XANES spectra of bulk and nanostructured TiO_2 samples. (B) Ce L_{III} -edge XANES spectra of bulk and nanostructured CeO_2 samples. Inset, derivative spectra of bulk (dotted line) and 4–5 nm size (full line) specimens.

the different CRs are dominated by contributions corresponding to different coordination shells and may not be present or display variations in energy/shape with respect to the bulk material in the corresponding XANES spectrum of a size-limited material.^{199,201,205–207} At the moment, no precise information is available concerning differences between surface species present in nanostructured and 2D infinite surfaces. A general feature shared by all nanostructured oxide materials is that they display broader CRs with respect to well-crystallized references.^{92,93,96,105,199,202,203} This can be observed in the inset of Figure 9; the derivative spectra give evidence of a larger overlap between CRs. The reason for this can be understood in terms of the *f*-rule.²⁰⁹ This rule implies that the total absorption over all edges and energies is a constant independent of the final state nature; therefore, disorder, inherent to nanostructured materials, broadens the spectrum without altering the overall intensity.²⁰²

A strong influence of size can be also found in the $1s \rightarrow d$ pre-edge transition present at K absorption edges ($1s$ absorption spectra, see Figure 9a) of transi-

tion metal cations inserted in an oxide matrix. Both a direct $1s$ -to- nd quadrupole transition and dipole transitions to states with $(n+1)p$ character hybridized with the nd subband are possible.¹⁰⁶ Typically, the matrix element of a dipole transition (equation 2.1.2.b) is about 2 orders of magnitude larger than quadrupole ones, but, on the other hand, the amount of d character at or immediately below the Fermi region is by far larger than the p one in transition metal ions. Depending on the particular system we are dealing with, the contributions from dipole and quadrupole can be equivalent or one can be neglected. In particular, for centrosymmetric systems, like cubic systems, only a very small admixture of p states is allowed into the nd subband while in non-centrosymmetric systems p/d mixing is symmetry allowed. It is rather obvious that corners, edges, and, in general, surface positions are non-centrosymmetric and can be therefore differentiated in the case of many oxides.

The $1s \rightarrow d$ transition can be composed by several peaks, depending on the symmetry and oxidation state of the metal ion constituting the oxide. Reviews of the literature can be found in refs 106 and 210. In the first transition row, three/two peaks can be observed from Ti to Fe cations in centrosymmetric positions due to the $(s)p-d$ mixing of the absorbent/central cation orbitals as well as to the presence of quadrupole transitions to d -like states of neighboring atoms. For some low oxidation states, low spin configurations and non-centrosymmetric positions of the above-mentioned cations as well as from Co- to Cu-containing oxides a single (most often dominant but not unique as is accompanied by shoulders) peak is obtained. As an example, Figure 9a displays the presence of a characteristic peak at the left of the vertical line, indicative of 5-fold-coordinated surface Ti ions, not present in the bulk of the material, which, therefore, allows one to investigate the characteristics as well as the quantity of surface species in Titania. Data on the second and third transition row are more scarce and usually less well defined due to poor energy resolution coming from the large core-hole lifetime inherent to the high photon energy used (above 17 keV).¹⁰⁶ This however may change soon with the removal of the lifetime broadening in XANES spectra by standardizing a detection scheme using low energy X-ray photoemission, emission decay, or Auger channels.^{210,211} Of course, this will be able to give larger resolution in the complete XANES spectrum, enhancing the electronic information extracted by using this technique but at the expense of a strong decrease in signal intensity. On the other hand, a detection scheme based on X-ray emission, such as, for example, using the $1snp$ fluorescence channel, would open a window to site-selective XANES and the corresponding speciation of species by chemical, surface/bulk, or other interesting properties.²¹⁰

2.2.2. Optical Absorption

Optical techniques can be devoted to the analysis of metal oxide electronic structures. As a major part of oxides are semiconductors or insulators, we will first detail such cases. The absorbance of light $\alpha(\lambda)$

by a solid semiconductor can be calculated by using the relation:

$$T = \frac{(1 - F)^2 e^{-\alpha(\lambda)\delta}}{1 - F^2 e^{-2\alpha(\lambda)\delta}} \quad (2.2.2.a)$$

where T is the measured transmittance, F is the reflectance, and δ is the optical path length.²¹² Metal oxides can be direct or indirect semiconductors depending on whether the valence to conduction band electronic transition is dipole allowed or forbidden. In the later case, the electronic transition is vibrationally allowed through vibronic coupling and phonon assisted. The intensity of the corresponding electronic transition is several orders of magnitude lower for indirect with respect to direct band gap semiconductors.²¹³ Indirect band gap semiconductors display thus a step structure at the absorption onset originated from the momentum conserving optical phonon absorption and emission and a generally stronger dependence of the absorption coefficient with energy near the edge.^{212,213} The absorption coefficient dependence of energy is stated in eq 2.2.2.b, where n equals $1/2$ or 2 for, respectively, direct and indirect semiconductors:

$$\alpha(\lambda) = B(\hbar\nu - E_g)^n(\hbar\nu)^{-1} \quad (2.2.2.b)$$

where B is a constant and E_g is the band gap energy.

As mentioned in the introduction, the nanostructure has a strong impact on the electronic structure of oxides producing the so-called quantum size of confinement effects. From a solid-state point of view, nanostructured oxides have discrete, atom-like electronic levels which can be considered as being a superposition of bulklike states with a concomitant increase in oscillator strength.^{34,35,214} Electronic effects related to quantum confinement potentially visible by optical absorption are the shift in band gap energy as a function of primary particle size as well as the discretization of the absorption, presenting a well-defined structure instead of the featureless profile typical of bulk solids.^{35,214} In metal oxides however the influence of nanostructure in optical spectroscopy data is mostly confined to the absorption onset energy as inhomogeneous broadening resulting from the particle size distribution induces broadening of the spectrum and limits the study of the shape of the optical absorption spectrum.

The onset of the optical absorption spectrum occurs at the so-called first exciton (electron–hole pair created after light absorption) or optical band gap energy. The most widespread, simple theoretical framework to study the influence of confinement effects and, particularly, the primary particle size influence in exciton energy, is the so-called effective-mass approximation (EMA).^{35,214} This assumes parabolic energy bands, infinite confining potential at the interface of the spherical semiconductor particle, and limits main energy terms to electron–hole interaction energy (Coulomb term) and the confinement energy of electron and hole (kinetic term). From experimental work it is customary to identify three different

energy regions as a function of the average crystalline radius (R) of the semiconductor particle:

(1) $R > a_B$, where a_B is the exciton Bohr radius of the extended/bulk semiconductor, defined as $a_B = a_e + a_h$ where a_e and a_h are the electron and hole Bohr radii, respectively. This is the regime of weak confinement and the dominant energy is the Coulomb term and there occurs a size quantization of the motion of the exciton (electron–hole pair is treated as a quasi-particle). The energy of the lowest excited state is a function of R as

$$E(R) = E_g + \frac{\hbar^2\pi^2}{2MR^2} \quad (2.2.2.c)$$

where E_g is the band gap energy of the bulk semiconductor, and M is the mass of the exciton ($M = m_e^* + m_h^*$; m^* being the effective mass of electron and hole). This indicates a blue shift of $E(R)$ as a function of R^{-2} .

(2) $R < a_B$ or strong confinement region, where the Coulomb term can be treated as a perturbation, and electron and holes are treated as confined independent particles, so the exciton is not formed and separate size quantization of electron and hole is the dominant factor. In this case $E(R)$ for the lowest excited state of a spherical cluster is given by

$$E(R) = E_g + \frac{\hbar^2\pi^2}{2R^2} \left(\frac{1}{m_h^*} + \frac{1}{m_e^*} \right) - \frac{1.786 e^2}{\epsilon_2 R} + 0.248 E_R \quad (2.2.2.d)$$

where the first corrective term to E_g is the confinement term, the second is the Coulomb correction with ϵ_2 the dielectric constant of the bulk semiconductor, and the third is the spatial correlation energy correction, being E_R the exciton Rydberg energy.^{35,36,215} As well-known at present, these formulas overestimate the $E(R)$ energy and are being corrected by using an effective bond-order model (EBOM) to construct the hole Hamiltonian, include spin–orbit coupling, and finite confining potential,²¹⁶ or by introducing the effect of shape distortion from a spherical particle model.²¹⁷ Alternative methods including these novel points in the framework of the tight-binding²¹⁸ or pseudopotential^{219,220} theories have been also published. An important additional challenge to all theories is to develop consistent theoretical estimates of the ϵ_2 dependence with R .²¹⁴

(3) The region between weak and strong confinement has not been thoroughly investigated but has deserved some attempts for specific semiconductors.²²¹ In this case, the large difference between the effective mass of the electron and the much heavier hole gives the quantization of the electron motion and its interaction with the hole by a Coulomb potential.²¹⁴

From the above discussion, it can be thus concluded that metal oxide semiconductors would present, as a first rough approximation, an optical band gap energy with an inverse squared dependence of the primary particle size if quantum confinement dominates the energy behavior of the band gap. Figure 10 shows that this happens to be the case for (direct

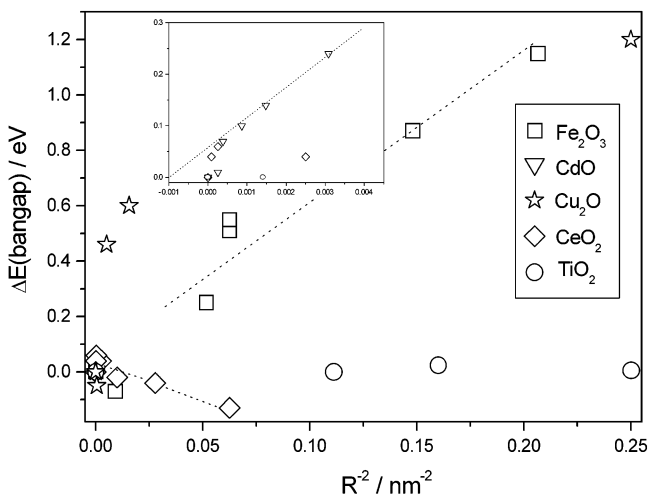


Figure 10. Optical band gap energy as a function of the inverse squared primary particle size for several metal oxides.

band gap) Fe_2O_3 ²²² or (indirect band gap) CdO ²²³ but not for Cu_2O ,²²⁴ CeO_2 ,^{29,225} and TiO_2 .^{226,227} Limited deviations from the R^{-2} behavior, as observed for ZnO ,²²⁸ can be based on the known fact that the theory (eqs 2.2.2.c and 2.2.2.d) overestimates the blue shift, while marked deviations are usually based on several chemical/physical phenomena not accounted for in the previous discussion. In the case of Cu_2O ²²⁴ or CeO_2 ,^{29,225,229} it appears to be directly related to the presence of Cu^{2+} (remarkably for very low particle size) and Ce^{3+} ions at the surface of the nanostructured materials. At the moment it is not clear if the presence of these oxidation states are intrinsic of the nanostructure or result from the specific procedure of preparation. This will be discussed at length for several oxides in section 3. Besides electronic modifications, such ions induce strain effects and concomitant structural differences in atomic positions with respect to bulk positions. The influence of strain in the absorption spectrum has been nicely demonstrated in the work of Ong et al. for ZnO ,²³⁰ showing the splitting of the first exciton peak for large values of compressive strain. Strain effects are inherent to nanostructured materials^{29,31,32} and may be comprised in the general, ambiguous term of “surface” effects usually claimed to account for significant deviations from eqs 2.2.2.c and 2.2.2.d. Surface effects related to the preparation method and particularly important for very low particle size are frequently observed for other oxides, as SnO_2 ²³¹ or ZrO_2 .²³²

TiO_2 is the other example included in Figure 10 having a band gap energy behavior with marked differences from that expected from eqs 2.2.2.c and 2.2.2.d. While bulk TiO_2 is an indirect semiconductor, nanostructured TiO_2 materials are likely direct ones.^{226,233} This may be a general result. As discussed in ref 234, the confinement of charge carriers in a limited space causes their wave functions to spread out in momentum space, in turn increasing the likelihood of radiative transitions for bulk indirect semiconductors. This may also be the case of NiO .²³⁵ The indirect nature of the absorption onset would complicate the analysis of the optical band gap energy due to the above-mentioned step structure of the

absorption onset (which includes phonon-related absorption/emission features).²³⁶ Despite this, the steady behavior shown in Figure 10 cannot be accounted for by small variations in the absorption onset and should be grounded in other physical phenomena. For small primary particle sizes, below 3–4 nm, this has been claimed to be based on a fortuitous cancellation effect between the kinetic/confinement and Coulomb terms in eq 2.2.2.d, but electronic grounds for this phenomenon still need to be understood. For indirect band gap semiconductors, recent theoretical results²¹⁹ suggest the presence of a red shift instead of a blue one with a primary particle size decrease, but recent careful experimental data corroborate the existence of the blue shift qualitatively described by eq 2.2.2.d.²³⁶

As happens with the absorption, the emission spectrum followed by photoluminescence or fluorescence from nanostructured samples has specific characteristics with respect to bulk systems.^{35,214} However, they do not usually add further insights into the main electronic structure of metal oxides and will not be treated here. A last word in this section can be said concerning semi-metallic or metallic metal oxides (as VO_2 at $T > 373$ K). Although a metal-to-insulator transition is expected as a function of size,^{34,35} this has not been analyzed in detail. Therefore, as a rough picture, we may expect the discretization of electronic levels and presence of well-defined transitions, which, however, would be typically broadened by the “size distribution” effect.

2.2.3. Valence and Core-Level Photoemission

The roots of core and valence level photoemission can be traced back to the famous article of Einstein explaining the photoelectric effect.²³⁷ In this work, he postulated the quantum hypothesis for light by the fundamental equation:

$$E_k = h\omega - \xi \quad (2.2.3.a)$$

here E_k is the maximum kinetic energy of the photoemitted electron, $h\omega$ is the energy of the exciting radiation, and ξ is the energy required to release the electron. Nowadays, eq 2.2.3.a is frequently written as

$$E_k = h\omega - E_B - WF \quad (2.2.3.b)$$

where E_B is the binding energy of the electron in the solid, and WF is the system “work function” (a catch-all term whose precise value depends on both the sample and spectrometer).²³⁸ The previous two equations assume that the photoemission process is an elastic process between matter and the external electric field. The photoemission process is the dominant de-excitation channel for atoms with atomic number Z lower than 30/50 for K/L edges, while Auger electrons dominate de-excitation for $Z > 30/50$. Thus, each characteristic excitation energy ($h\omega$) will give rise to a series of photoelectron peaks that reflect the discrete binding energies of the electrons (with energy lower or equal than the excitation one) present in the system.²³⁸ The intensity of the peak is essentially an atomic property and thus allows the

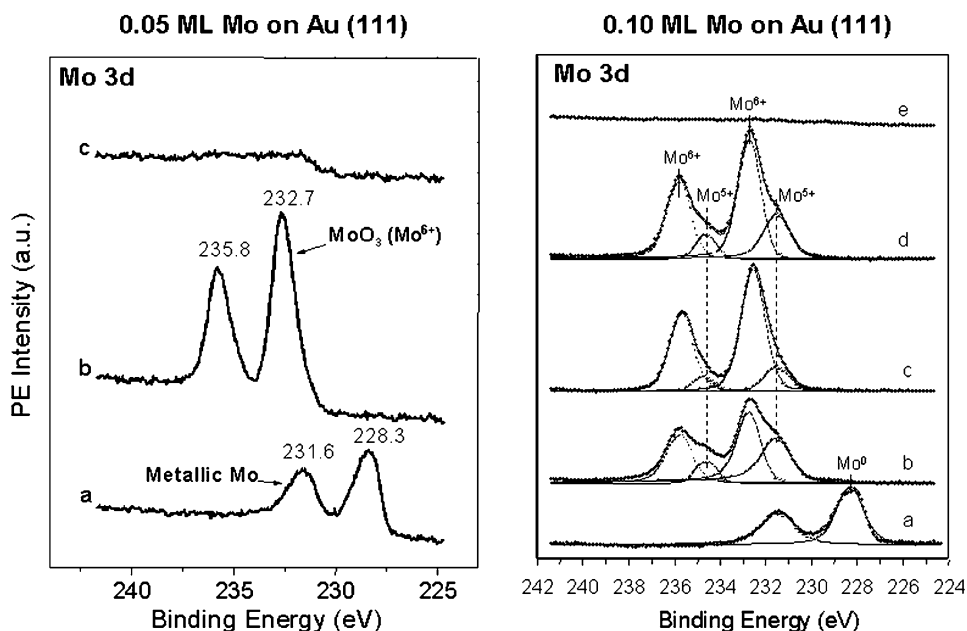


Figure 11. Left-side panel: Mo 3d photoemission spectra taken from 0.05 monolayer (ML) of Mo deposited on a Au(111) substrate: (a) before oxidation of the Mo nanoparticles, (b) after oxidation at 500 K, and (c) upon heating the sample to 700 K. Right-side panel: Mo 3d spectra taken for a Au(111) substrate covered by 0.10 ML of molybdenum: (a) before oxidation, (b) after a first oxidation at 500 K, (c) after a second oxidation at 500 K, (d) upon heating the oxidized sample to 700 K, and (e) after final heating to 800 K. Reprinted with permission from ref 23. Copyright 2003 American Chemical Society.

quantification of the absorber atom at the surface and near surface layer.²³⁸

In the period of 1950–1970, pioneer work by the groups of Siegbahn,²³⁹ Turner,²⁴⁰ and Spicer²⁴¹ showed that spectra with well-resolved ionization peaks could be obtained when using high-resolution electron energy spectrometers combined with X-ray or ultraviolet radiation for photoexcitation. The typical experiments of X-ray photoelectron spectroscopy (XPS) utilize Mg *K* (1253.6 eV) or Al *K* (1486.6 eV) radiation to excite the electrons.²³⁸ He I (21.21 eV) and He II (40.82 eV) are photon energies frequently used in ultraviolet photoelectron spectroscopy.²⁴² Synchrotrons are a very valuable tool for performing photoemission experiments.^{243–245} Electrons orbiting in a synchrotron emit radiation that spans a wide spectral region is highly collimated and polarized. Using the facilities available at synchrotrons, one can get photoemission spectra that have simultaneously a very high resolution and excellent signal-to-noise ratio.^{243,244} The acquisition of spectra can be very fast, and chemical transformations can be followed as a function of time.^{246–248}

Valence Photoemission. Depending on their energy, the levels occupied by the electrons in a nanoparticle can be labeled as core (> 50 eV), semi-core, or valence (<20 eV).²³⁸ In the valence region, the electrons occupy delocalized or bonding orbitals. The spectrum in this region consist of many closely spaced levels giving rise to a band structure.^{249–252} For large oxide nanoparticles, valence bands similar to those of the bulk materials are expected. As the size of the nanoparticles decreases, unique features could appear in the valence region,^{249,252} and eventually the valence bands could break down into discrete levels in the case of small oxide clusters.²⁵³ In their bulk states, some oxides can have metallic character,

but most frequently these systems behave as semiconductors or insulators and have a significant gap between the valence and conduction bands. Due to size effects, a nanoparticle could have a band gap energy differing from that of its bulk state (see section 2.2.2 for a detailed analysis), and this could be detected in valence photoemission.^{249,253,254} This technique is also very useful to verify the presence of O vacancies in an oxide nanoparticle. Electronic states associated with O vacancies usually appear above the valence band of the oxide in the band gap.^{255,256}

Core Photoemission. The discovery, during the early days of XPS,²³⁹ that nonequivalent atoms, either by symmetry or oxidation state, of the same element in a solid gave rise to core-level peaks with different binding energies had a stimulating effect in the development of the field.²³⁸ Core-level photoemission can be very sensitive to changes in the oxidation state of an element. Thus, different oxides of the same metal element in many cases have substantially different core-level binding energies.²⁵⁷ Figure 11 illustrates the utility of core-level photoemission for the characterization of oxide nanoparticles. These XPS data were acquired in experiments similar to those that produced the STM images in Figure 1.²³ MoO₃ and Mo₂O₅ were prepared by the oxidation of Mo nanoparticles present on a Au(111) substrate. Initially, there is intermixing of Mo and Au. The formation of the MoO_x nanoparticles induces migration of Mo from inside the Au substrate to the surface, and, thus, there is a big increase in the intensity of the signal for the Mo 3d core levels.^{23,25} A Mo → MoO₃ transformation is accompanied by a shift of ~ 4.3 eV in the Mo 3d levels. At small concentrations of molybdenum (~ 0.05 monolayer), the Mo nanoparticles can be fully oxidized (left-side

panel in Figure 11, spectrum b). On the other hand, after oxidizing a larger concentration of molybdenum (~ 0.10 monolayer), photoemission shows a mixture of MoO_3 and Mo_2O_5 (right-side panel in Figure 11, spectra b, c, and d).²³

Core-level binding-energy shifts constitute one of the most widely used diagnostic tools for routine chemical analysis in industrial laboratories.⁸² A lot of effort has been focused on the interpretation of these shifts.^{82,238} A core-level binding energy is fundamentally a difference in total energy between the ground and unbound continuum excited states of a system. This difference can have initial- and final-state contributions.⁸² To induce a core-level shift with respect to a well-defined reference, one can modify the initial or final state. Thus, a change in the oxidation state of an element can lead to a shift in its core-level binding energies (initial state effect), but a core-level shift also can be produced by a variation in the screening of the hole left by the emitted electron (final state effect).⁸² A priori, it is not easy to evaluate final-state contributions to core-level binding-energy shifts.^{82,238}

Several models, based on physical simplifications of the photoemission process, have been proposed for the analysis of core-level shifts in oxide compounds.^{82,258–264} The physical basis for a core-level shift can be illustrated by a simple charge potential model:^{238,239}

$$E_i = E_i^R + kq_i + \sum q_j/r_{ij} \quad (2.2.3.c)$$

where E_i is the binding energy of a particular core level on atom i , E_i^R is an energy reference, q_i is the charge on atom i , and the final term of eq 2.2.3.c sums the potential at atom i due to “point charges” on surrounding atoms j . The last term can be expressed as $V_i = \sum q_j/r_{ij}$. Then, the shift in binding energy for a given core level of atom i in two different chemical environments is:²³⁸

$$E_i^{(1)} - E_i^{(2)} = k(q_i^{(1)} - q_i^{(2)}) + (V_i^{(1)} - V_i^{(2)}) \quad (2.2.3.d)$$

The first term, $k\Delta_i$, indicates that an increase in binding energy accompanies a decrease in the valence electron density on atom i . The second term depends on the charge distribution of the whole system, is related to the Madelung potential of the oxide, and has an opposite sign to Δ_i in eq 2.2.3.d.^{238,239} For highly ionic oxides, the effects of the Madelung potential can be quite strong and dominate the overall direction of the core-level shifts.^{238,259} Thus, Hartree–Fock self-consistent field calculations for BaO clusters show that the removal of two s electrons leads to an increase of the core-level binding energies in Ba^{2+} over neutral Ba (as expected), but this increase is offset by the Madelung potential and the XPS measurements show a net negative core-level shift. The dominance of these two electrostatic effects in the core-level shifts of all alkaline-earth oxides was also demonstrated.²⁵⁹ From eq 2.2.3.d, it is clear that one can have a core-level shift in an oxide nanoparticle by changing the oxidation state of atom i , by

modifying the Madelung potential, by the creation of O vacancies, or by just moving the atom i to a nonequivalent position (like surface ones) within the structure of the system.

Equation 2.2.3.d is a first approximation of the problem of core-level shifts, and in general should be used only in qualitative terms.^{82,238} A major simplification of the charge potential model is that it neglects relaxation effects, e.g., it does not take into account the polarization effect of the core hole on the surrounding electrons, both intra-atomic (on atom i) and extra-atomic (on atoms j).^{82,238} A precise interpretation of core-level binding energy shifts frequently requires the use of quantum-mechanical calculations.^{258,259,264} This is the best way to separate contributions from initial and final state effects.^{265–267} Initial state effects are frequently calculated by the Koopman’s theorem which essentially depends on the “sudden approximation”, explained in section 2.1.2, to describe the photoemission process as being realized by one electron while the remaining $N - 1$ electrons of the system are “frozen”. The use of the full electron (final-state) wave functions yields the core-hole energy. Note that several final-state wave functions corresponding to a localized/delocalized nature of the hole and the existence of hole-induced charge transfer ($\text{M}^{(n+1)+} - \text{L}^{-1}$) are usually possible. The latter typically produces the presence of secondary peaks, close to the main but with lower intensity, for transition metals oxides having d holes in the final state. The difference between these two quantities, e.g., the initial state and the core-hole energies, is the relaxation energy.^{82,238} The relaxation energy may vary from one oxide to another and with the size of the particle, since it is affected by the Madelung potential.⁸²

Charging is a phenomenon that can occur when the conductivity of the oxide nanoparticles or nanostructures is too low to replenish the photoemitted electron.^{82,238} This means that a significant net positive charge accumulates in the system, and eventually produces a shift in the binding energy position of the core and valence levels. Unfortunately, a fully satisfactory solution to charging problems is not yet available. Several approaches have been proposed.^{82,238} A flood gun is one of the easiest and most common solutions to charging problems. It produces a huge increase in the concentration of low-energy electrons. One must verify that these “extra” electrons do not induce any structural or chemical transformation in the sample. Whenever possible, it is highly advantageous to deposit the oxide nanoparticles on a conducting support.^{268,269} During the photoemission process, electrons spill from the support and neutralize the charging effects. The data in Figure 11 show how effective this approach can be.²³

2.2.4. Theoretical Studies

In the last 10 years, computational chemistry has become a valid and practical approach for studying fundamental physical and chemical properties of molecules, solids, and surfaces.^{270–272} Some concepts are useful for explaining the chemical behavior of a broad range of systems.^{48,49} In several areas, theo-

retical methods have evolved to the point that they are not only useful for explaining experimental data, but also have predictive power.^{273–276} When dealing with oxide nanoparticles or nanostructures, one needs a methodology that is robust, flexible, and fast enough to handle systems that range from a few atoms to bulklike materials. The ultimate goal is the prediction of reliable structural features, force fields, and vibrational frequencies (IR and Raman spectra), electronic properties (photoelectron, ESR, and UV spectra), thermochemical data, and parameters associated with chemical reactions (activation barriers, transition state structures, etc.). This is an enormous and very complex task that cannot be achieved using a single theoretical method. In general, two different classes of theoretical approaches have been employed in the study of oxide nanoparticles and nanostructures: quantum-mechanical methods and atomistic models mainly based in electrostatic interactions.

The quantum-mechanical methods can be divided into those based on Hartree–Fock or post-Hartree–Fock formalisms (wave function techniques)^{277,278} and those based on density functional theory (DFT).^{279,280} The main interest is to find approximate solutions to the time-independent nonrelativistic Schrödinger's equation:

$$H\Psi = E\Psi \quad (2.2.4.a)$$

where H is the Hamiltonian of the system, and Ψ is the corresponding electronic wave function. Within the Born–Oppenheimer approximation, the Hamiltonian contains terms for the kinetic energy of the electrons, attractive interactions between the electrons and nuclei, and repulsive interactions that involve the electrons or the nuclei.²⁸¹ In the Hartree–Fock method,^{277,278} every electron is regarded to be moving in an effective single-particle potential $v_{\text{hf}}(r)$ that takes into account interactions with the nuclei and other electrons. Each electron obeys a single particle Schrödinger's equation:

$$\{-(1/2)\nabla^2 + v_{\text{hf}}(r)\}\psi_i(r) = \epsilon_i\psi_i(r) \quad (2.2.4.b)$$

that leads to the molecular orbitals ψ_i and corresponding energy ϵ_i . The wave function of the system is then written in terms of a set of n molecular orbitals ψ_i ($i = 1, \dots, n$):

$$\Psi = (n!)^{-1/2} \det[(\psi_1\alpha)(\psi_1\beta)(\psi_2\alpha)\dots] \quad (2.2.4.c)$$

Here the ψ_i are taken to be orthonormal and the α and β are spin functions. This single-configuration wave function is usually described as a Slater determinant (in the spin-restricted formalism).^{277,278,281} The orbitals ψ_i are varied to minimize the energy, calculated as the expectation value of the full Hamiltonian:

$$E = \langle \Psi | H | \Psi \rangle \quad (2.2.4.d)$$

The Hartree–Fock orbitals are usually expressed as a linear combination of atomic basis functions φ_u ($u = 1, 2, \dots, N$, $N > n$):

$$\psi_i = \sum_u c_{ui}\varphi_u \quad (u = 1 \dots N) \quad (2.2.4.e)$$

Variation of the total energy (eq 2.2.4.d) is then carried out with respect to the coefficients c_{ui} . This leads to a set of algebraic equations that can be written in matrix form (Roothaan equations):^{8,9,282}

$$\text{FC} = \text{SCE} \quad (2.2.4.f)$$

These nonlinear equations provide a complete mathematical model once a set of functions φ_u is defined. They are also referred to as self-consistent field (SCF) equations and are solved using iterative procedures until autoconsistency is achieved.^{277,278}

The major fault implicit in all Hartree–Fock models is the neglect of electron correlation between the motions of electrons of antiparallel spin ($\alpha\beta$ correlation).^{277,278} This leads to severe underestimation of bond dissociation energies. The neglect of $\alpha\beta$ correlation is the result of using a single-determinant wave function. In most post-Hartree–Fock correlation procedures, the improved wave functions necessarily involve the use of many determinants. The method of configuration interaction (CI) starts with the Hartree–Fock determinant and forms a linear combination with other determinants obtained by promotion of electrons into the virtual or unoccupied ψ_i orbitals.^{277,278,281} The single-determinant functions using the ψ_i orbitals may be classified as unsubstituted (i.e., Hartree–Fock) ψ_0 , singly substituted ψ_{SS} , doubly substituted ψ_{DS} , and so forth. A general multideterminant wave function is then written as

$$\Psi = a_0\Psi_0 + 3a_I\Psi_{\text{SS}} + 3a_{II}\Psi_{\text{DS}} + \dots \quad (2.2.4.g)$$

where the a coefficients are determined by variation to minimize the calculated energy. The simplest effective form of CI allows only for double substitutions in eq 2.2.4.f and is frequently denoted as CID. If single substitutions are also included, the method is CISD.

A second general method of incorporating electron correlation is to treat its effects by perturbation theory.^{277,283} A perturbed Hamiltonian is defined as

$$H(\lambda) = F_0 + \lambda\{H - F_0\} \quad (2.2.4.h)$$

in which F_0 is the Fock Hamiltonian, then ψ_0 is the appropriate wave function if $\lambda = 0$ and the exact (full CI) Ψ is obtained if $\lambda = 1$. The Moeller–Pleset method expands the computed energy in powers of λ :^{277,278}

$$E(\lambda) = E_0 + \lambda E_1 + \lambda^2 E_2 + \lambda^3 E_3 + \dots \quad (2.2.4.i)$$

The series is cut off at some level (denoted as MP n at order n), and λ is set equal to 1. The MP1 energy ($E_0 + E_1$) is identical to the Hartree–Fock value. MP2 is the simplest practical perturbative procedure for electron correlation and incorporates only effects of double substitutions. MP3 also involves only double substitutions. At the fourth-order level, MP4 includes a description of the (indirect) effects of single substitutions, the leading contributions of triple substitutions, and some treatment of certain quadrupole substitutions.^{277,278,283}

The post-Hartree–Fock methods described above are characterized by the need for a substantial amount of computer power. For complete geometry

optimization, this makes difficult their application to oxide nanoparticles that contain a large number of metal atoms in the oxide structure (>20). As an alternative, semi-empirical methods have been developed based on the Hartree–Fock approach.^{284–289} These make use of approximations and neglect certain classes of multicenter two-electron Coulomb integrals present in the \mathbf{F} matrix of eq 2.2.4.f. Other integrals are replaced by empirical formulas that include adjustable parameters, which are optimized to reproduce properties within a given set of reference data. The net effect of this is to reduce the computer time significantly, and, thus, it is now possible to treat oxide nanoparticles containing on the order of 200–500 atoms. A disadvantage of the Hartree–Fock-based semiempirical methods is the fact that they are only useful to evaluate the properties for which they have been parametrized. Methods based on density functional theory are able to calculate a large set of physical and chemical properties, and do not need as much computer power as post-Hartree–Fock methods.^{270–275}

DFT provides a complimentary perspective to the wave function approach. It focuses on quantities in the real, three-dimensional coordinate space, principally on the electron density $\rho(\mathbf{r})$.²⁹⁰ The first Hohenberg–Kohn theorem states that the electron density, $\rho(\mathbf{r})$, determines the external (i.e., due to the nuclei) potential, $v(\mathbf{r})$.²⁹¹ The Hamiltonian of the system depends on $v(\mathbf{r})$, and thus the energy of the system (E in eq 2.2.4.a) is a functional of ρ ²⁹²

$$E = E_v[\rho] = \int v(\mathbf{r})\rho(\mathbf{r})d\mathbf{r} + F_{\text{HK}}[\rho] \quad (2.2.4.j)$$

here F_{HK} is the Hohenberg–Kohn functional containing the electronic kinetic energy functional, $T[\rho]$, and the electron–electron interaction functional, $V_{\text{ee}}[\rho]$

$$F_{\text{HK}}[\rho] = T[\rho] + V_{\text{ee}}[\rho] \quad (2.2.4.k)$$

The $V_{\text{ee}}[\rho]$ term can be separated in two components:^{279,292}

$$V_{\text{ee}}[\rho] = J[\rho] + E_{\text{XC}}[\rho] \quad (2.2.4.l)$$

$J[\rho]$ represents the classical Coulombic interaction energy, and the remaining energy components are assembled in the $E_{\text{XC}}[\rho]$ functional: the exchange correlation energy, the nonclassical part of $V_{\text{ee}}[\rho]$, and self-interaction corrections. In general, the exact form of the $E_{\text{XC}}[\rho]$ functional is unknown.

If N electrons occupy N molecular orbitals ψ_i , the electron density can be written as

$$\rho = \sum_i \psi_i^* \psi_i \quad (i = 1 \dots N) \quad (2.2.4.m)$$

and the molecular orbitals can be obtained from the Kohn–Sham equations²⁹³

$$\{-\frac{1}{2}\nabla^2 + v_{\text{eff}}(\mathbf{r})\}\psi_i(\mathbf{r}) = \epsilon_i\psi_i(\mathbf{r}) \quad (2.2.4.n)$$

$$v_{\text{eff}}(\mathbf{r}) = v(\mathbf{r}) + \int \rho(\mathbf{r}')d\mathbf{r}'/|\mathbf{r} - \mathbf{r}'| + v_{\text{xc}}(\mathbf{r}) \quad (2.2.4.o)$$

which contain the exchange correlation potential, $v_{\text{xc}}(\mathbf{r})$, defined as

$$v_{\text{xc}}(\mathbf{r}) = \delta E_{\text{XC}}/\delta \rho \quad (2.2.4.p)$$

The Kohn–Sham equations (eq 2.2.4.n) are one-electron equations, just as the Hartree–Fock equations, and must be solved iteratively. The cost of incorporating electron correlation is the appearance of the exchange correlation potential, v_{xc} , the form of which is unknown.^{279,292}

The simplest approximation for $E_{\text{XC}}[\rho]$ is the so-called local-density approximation (LDA).^{293,294}

$$E_{\text{XC}} = \int e_{\text{xc}}(\rho(\mathbf{r}))\rho(\mathbf{r})d\mathbf{r} \quad (2.2.4.q)$$

where $e_{\text{xc}}(\rho)$ is the exchange-correlation energy per particle of a uniform electron gas of density ρ . It has been found that the LDA can give reasonable geometries but substantially overestimates bonding energies. In the next step, the so-called generalized gradient approximation (GGA), it is assumed that E_{XC} depends on ρ and its gradient. Several GGA functionals have been proposed: Becke–Perdew,^{295,296} Perdew–Wang,²⁹⁷ Becke–Lee–Yang–Parr,^{295,298} Perdew–Burke–Ernzerhof,²⁹⁹ B3LYP,³⁰⁰ etc. The hybrid B3LYP functional is one of the most popular, and its performance has been extensively tested for molecular geometries,³⁰¹ ionization energies and electron affinities,^{302–304} dipole and quadrupole moments,^{305,306} atomic charges,³⁰⁵ vibrational frequencies,³⁰⁷ and infrared intensities.³⁰⁵ New approaches using the exact-exchange formalism may be important for the correct analysis of band gap energy in oxides.³⁰⁸

Atomistic simulations can be useful to study the structure and stability of big oxide nanoparticles that will require an excessive amount of computer time when studied with post-Hartree–Fock or DFT-based methods.^{309–311} In these theoretical studies, a large degree of ionicity in the metal–oxygen bonds of the nanoparticle is assumed, and the total energy is determined by electrostatic interactions between the cations and the anions. Thus, the lattice energy of the oxide system contains three main contributions:³¹²

$$E_{\text{latt}} = E_{\text{coul}} + E_{\text{sr}} + E_{\text{sh}} \quad (2.2.4.r)$$

E_{coul} is the purely electrostatic (Coulombic) interaction energy and on average makes the largest contribution to E_{latt} . For small to moderate-sized systems, E_{coul} is most efficiently evaluated by means of Ewald sums.^{310,312} The E_{sr} term introduces the effects of overlap repulsion between ions, plus dispersion and covalence effects, collectively described as short-range interactions. It usually has the form of the Buckingham potential,^{309–311} which includes a repulsive (Born) term and an attractive (van der Waals) term:

$$E_{\text{sr}} = \sum_{ij}[A_{ij} \exp(-r_{ij}/\delta_{ij}) - C_{ij}/r_{ij}^6] \quad (2.2.4.s)$$

where r_{ij} is the interionic distances. For each atomic pair (i, j), δ_{ij} defines the distance scale of the Born repulsion, while A_{ij} and C_{ij} characterize the magnitudes of Born and van der Waals interactions.³¹⁰ The Buckingham potential is a valid approximation for strongly ionic materials. In the case of more covalent

systems, other short-range interaction potentials must be used,³¹² and three-body contributions cannot be neglected. The third term in eq 2.2.4.r, E_{sh} , simulates the effects of electronic polarizability, and different expressions have been suggested to evaluate it.^{309–311} The problem of finding the equilibrium structure of an oxide nanoparticle is equivalent to finding the global minimum of E_{latt} . The search for this minimum can be done using “simulated annealing”, and Monte Carlo or molecular dynamics simulations.^{309–312}

3. Oxide Systems

The study of the influence of the nanoscale on structural and electronic parameters and chemical reactivity has been only addressed systematically for a small number of oxides. From a simple point of view, such oxides can be divided into two groups. The first would contain materials in which the nanostructure stabilizes a specific polymorph which is not the stable phase for a bulk material, while the second can contain oxides that share the fact that nanostructured and bulk samples display the same phase. The first group is typical but not exclusive of oxide systems in which the stable bulk polymorph phase has an oxygen close-packed structure; we will detail here the case of TiO_2 and ZrO_2 and, to a lesser extent, Al_2O_3 . CeO_2 appears as the main target of studies in the case of the second group due to its industrial use, but a significant effort has been also done for MgO , which, besides its industrial application, is a model for highly ionic compounds. We will finish this section with a brief review of data concerning other oxide systems containing Fe, Ni, Sn, and Zn.

3.1. Ti-Containing Oxides

3.1.1. Pure Titania Nanoparticles

Titanium dioxide (TiO_2) is one of the most prominent materials in performing various kinds of industrial applications related to catalysis, e.g., the selective reduction of NO_x in stationary sources,^{313,314} photocatalysis for pollutant elimination³¹⁵ or organic synthesis,³¹⁶ photovoltaic devices,³¹⁷ sensors,³¹⁸ and paintings.³¹⁹ Additional applications of importance include its use as a food additive,³²⁰ in cosmetics,³²¹ and as a potential tool in cancer treatment.³²² The (n-type) semiconductor properties of TiO_2 materials are essential in accomplishing these functions. The Ti–O bond appears to have an increasing covalent character with the oxygen content of the oxide, so the departure of Ti^{n+} from the formal oxidation state grows from +2 to +4.³²³ Experimental approaches to scale down the primary or intrinsic particle size of TiO_2 to the nanometer scale are now actively investigated to improve its current applications and to reach more advanced ones such as its use in electrochromic devices.³²⁴ As a general result, the nanostructure induces an increase in surface area with concomitant enhancement of the chemical activity and also of the photochemical and photophysical activities with a potential reduction of light scattering.

TiO_2 occurs in nature in three different polymorphs, which, in order of abundance, are rutile,

anatase, and brookite. An additional synthetic phase is called $\text{TiO}_2(\text{B})$,³²⁵ while several high-pressure polymorphs have been also reported.^{6,326} Mesoporous amorphous materials have been additionally prepared having a Ti local structure similar, at least to a first approximation, to that present in surface/bulk nanostructured anatase samples.¹⁰⁰ As an extended (bulk) system, rutile is thought to be the thermodynamic stable phase, although, based in calorimetric and theoretical investigations, there is a controversy in the literature about whether the rutile or the anatase is in fact the stable polymorph (see ref 326 for a recent discussion). The surface properties of these extended materials are summarized in the excellent review of Diebold.¹⁷⁸ When the primary particle size is scaled down, a thermodynamic analysis of phase stability indicates that surface free energy and stress contributions stabilize anatase below a certain size close to 15 nm.²¹ Above such limit, brookite and rutile appear to have very close free energy values up to a size close to 35 nm, above which rutile seems the stable phase.^{21,327} In these nano- TiO_2 materials, surface energy appears to be related with the presence of undercoordinated Ti cations; the surfaces with 4-fold-coordinated centers have larger energy than those with 5-fold coordination, and the surface energy approximately increases with the number of undercoordinated positions.³²⁸ XAS measurements seem in agreement with this as only 5-fold-coordinated Ti centers are observed at the surface of nanostructured materials.^{92,93,94} First principles analysis of surface energy also suggests that the average surface energy of an anatase crystal may be lower than that of a rutile phase.³²⁷ In contrast, experimental measurements of the surface stress contribution give, for a similar particle size, a larger value for the anatase than the rutile matrix.³²⁹ There seems to be therefore a “compensation-type” effect between surface and stress energy contributions to the two TiO_2 polymorphs that is not well understood at this moment.^{21,327,329} In any case, although nanostructured anatase,^{330–334} rutile,^{331–335} and brookite³³⁶ materials have been prepared, it seems that a single phase with an average particle size in the 2–15 nm range is only possible with the anatase structure. Rutile is most often obtained with the help of mineralizers (such as SnCl_4 , NH_4Cl , NaCl , or SnO_2) or in the presence of Cl ions (from HCl or the precursor salt), and the presence of this Cl^- or another ions may be of importance to get this particular polymorph but with a minimum size in the 10–20 nm range.^{333–335} Brookite samples are usually obtained with larger dimensionality.³³⁶

The nanostructure of the TiO_2 material strongly affects the phase behavior, tuning the thermal stability and corresponding phase transformation of the polymorphs. Concerning anatase samples, the anatase \rightarrow rutile phase transformation occurs in a broad temperature range, from around 723 to 1273 K.^{337–340} As it is obvious, grain/particle size growth and phase transformation are parallel phenomena during a thermal treatment of a nanostructured solid, but in TiO_2 the size-dependent relative stability of the polymorphs²¹ interrelates these two variables, in turn

making difficult the identification of thermodynamic and kinetic parameters present in the phase transition. In ref 337, it was shown that a smaller average primary particle size decreases the onset and the rate of the phase transformation, displaying thus a broader range of coexistence between anatase and rutile with decreasing particle size. Further analyses³³⁸ indicate however that not only the primary but also the secondary particle size (e.g., the porosity of the sample) are key properties to modulate the anatase-to-rutile phase transformation. As could also happen with ceria and zirconia (see sections 3.2, 3.3), the high temperature phase may initially form on the surface of the low temperature counterpart (independently of the exact growth mechanism and the importance of surface energy/stress and/or ion mobility contributions)^{338,340} and grows at the expense of the latter. Therefore, specific geometrical details of the surface anatase or even the presence of diffraction-silent amorphous or poorly crystalline (mainly brookite) phases may also exert a definitive influence in this phase transformation. In brief, although it is clear that surface properties plus primary and secondary particle sizes are important parameters in governing the behavior of the anatase \rightarrow rutile transformation, their exact influence is still a matter of debate. An even more complicated behavior is observed for brookite; the presence of anatase as an intermediate phase to a final conversion into rutile also appears an up-to-date unveil function of the above-mentioned variables.^{21,327,338}

The nanostructure also affects other important properties of the TiO_2 material, of importance in its technological applications. As a semiconductor used in photochemical and photophysical applications, one critical parameter is the band gap energy and characteristics. Although the extended/bulk anatase material is an indirect band gap semiconductor, the nanostructured anatase TiO_2 samples are likely direct semiconductors.^{226,233} For indirect band gap semiconductors, the valence to conduction band electronic transition is electrical dipole forbidden, vibrationally allowed, and photon assisted (i.e., both energy and momentum of the electron-hole pair change) while direct band gap transitions are dipole allowed. The absorption at threshold but particularly the emission of light is thus stronger for the direct systems, resulting in a more efficient management of light and in potentially improved photochemical or physical performances for nanostructured materials. Additionally, measurements of the optical band gap give a variety of results; papers dedicated to optical measurements^{21,235} give evidence of a steady behavior of the optical band gap energy as a function of primary particle size. In contrast, other works display the expected (based on a R^{-2} dependence of the optical band gap energy, eq 2.2.2.d) blue shift of the exciton energy with decreasing particle size.⁹³ Although no conclusive conclusion can be at the moment reached for this apparent contradiction, the latter behavior could be connected with the presence of impurities³⁴¹ and/or amorphous phases and thus be a consequence of the preparation method.

Electrical/ionic conductivity is the other type of property of TiO_2 materials that can be modulated by nanostructure and has current technological applications in the field of sensors or electronic devices. The metal/ TiO_2 contact is used at low temperatures in sensor devices. At high temperatures, TiO_2 can be easily reduced, and this decisively influences conductivity. The titanium-oxygen phase diagram is very rich with many stable phases with a variety of crystal structures. As an example, the region TiO_2 – Ti_2O_3 contains Ti_2O_3 , Ti_3O_5 , seven discrete phases of the homologous series $\text{Ti}_n\text{O}_{2n-1}$ (Magnelli phases), and TiO_2 .³⁴² Bulk defects result in n-type doping and high conductivity,³⁴³ and are of various types such as doubly charged oxygen vacancies, $\text{Ti}^{3+}/\text{Ti}^{4+}$ interstitials, and planar defects such as crystallographic shear planes,^{343,344} while surface defects are mostly ascribed to undercoordinated Ti anions and (doubly charged) oxygen vacancies.³²⁶ Their presence, characteristics, and development under reductive atmospheres as a function of temperature are less defined for nanostructured materials. Grain boundaries, on the other hand, strongly influence electrical conductivity as measured by impedance spectroscopy.³⁴⁵ A limited number of oxygen vacancies in nano- TiO_2 have been reported on the basis of several Raman works,^{118,346} but its presence in a significant number is dubious on the basis of EXAFS⁹³ or other Raman¹¹⁹ results. As suggested, the presence of “intrinsic” vacancies may be an effect of the preparation variables rather than an intrinsic property originated from the nanostructure, although more work is required to definitively set this question. The onset temperature of the material reduction is expected to depend on defect concentration and thus would be dependent on primary particle size,^{337,346} however, this has not been fully analyzed in the literature.

3.1.2. Ti-Containing Mixed-Metal Oxides

The doping of TiO_2 structures constitutes an extensive field of research and requires a separate mention. Surface and bulk doping have been used to stabilize the anatase or rutile phases, influence the temperature of the anatase \rightarrow rutile phase transformation, modulate the optical band gap, or alter the ionic/electrical conductivity by the presence of intrinsic vacancies. The properties of the mixed oxide depend primarily on the doping process nature; substitutional mixed oxides have been shown to be formed in the case of Ta, Nb, and W,^{347,348} while V^{349} and Fe^{350} appear to occupy (partially in the case of V) interstitial positions. Analysis of XRD/neutron data indicate that the presence of anion vacancies for substitutional doping with trivalent/divalent ions and cation vacancies for W/Nb substitutional or V/Fe interstitial doping seems to be formed together with, for example, Ti lattice defects related to the presence of hydroxyls in the case of nanostructured Fe-doped TiO_2 calcined at $T < 673$ K,³⁵⁰ or strong structural modifications in the oxygen sublattice in the case of nanostructured W-doped TiO_2 .³⁵¹ Thus, charge neutrality appears to be a rather complex phenomena with elaborated structural/electronic implications, at least with respect to the simplest case of cerium oxide hereafter detailed (section 3.3). This difference could

be related to energetics effects in turn related to the more "open" (cation-deficient) structure of the anatase-TiO₂ phase with respect to CeO₂. On the other hand, the doping process typically decreases primary particle size when comparing with TiO₂ samples prepared in a similar way, while the presence of heteroatoms at the surface usually (but not always) favors coalescence of grains/particles, with a concomitant increase of the secondary particle size and loss of surface area.^{348–351} Concerning the influence in the phase stability and transformation, summaries of literature reports can be found in refs 329, 347, and 352. These papers indicate that doping with Al, Ni, Ga, Nb, Ta, and W retards grain/particle growth of anatase and rutile phases and delays the anatase to rutile phase transformation, while Mn, Fe, Cu, and Zn generally promote the phase transformation. The theoretical basis of the different cation effect is however not known. It must be recalled that such effect strongly depends, among other things, on the surface characteristics of the material and, therefore, of several phenomena like surface segregation or enrichment which are largely influenced by the preparation procedure; this limits the usefulness of the above generalization. Apart from that, the stable bulk phase is expected to have a lower solubility limit for dopants as it is "cation-rich" with respect to the stable nanostructured polymorph. This means that, for a total level of dopant, the degree of segregation at surface/grain boundaries will presumably increase as the primary size increases, limiting again the mentioned generalization until a detailed surface/bulk characterization of nanostructured materials is performed. Other dopant atoms such as Ca, Sr, and Ba,³⁵³ or Sn³⁵⁴ produce blue shifts of the optical band gap energy which may, at least, partially be due to a decrease in primary particle size and concomitant quantum confinement effect, likely associated with the presence of the heteroatom in the TiO₂ structure. In the case of V, Cr, Nb, Mo, and W,³⁵⁵ or rare earth atoms³⁵⁶ a red shift of the optical band gap appears to be observed. Appearance of heterometal states at the bottom of the conduction band seems a possible explanation in the last case. Some of these cations, when present in the adequate oxidation state, can additionally introduce detectable d–d transitions in the UV–vis spectra.^{355,356}

3.2. Zr-Containing Oxides

Zirconia-based materials are most interesting from a technological point of view, mainly as a consequence of their outstanding electrical, chemical, and mechanical properties that make them useful materials in the fields of ceramics, solid electrolytes, gas sensors, and catalysis.^{357–361} Decreasing the size of the zirconia-based particles to nanometric levels provides changes in such properties due to the modifications produced at structural or electronic levels, as will be analyzed below. Thus, aspects such as the stabilization of the tetragonal structure (presenting higher ionic conductivity and strength with respect to the monoclinic polymorph), improved sintering characteristics, increased surface area, or modified mechanical properties (possibility of achiev-

ing superplastic characteristics, decreased fracture toughness, etc.) are characteristic of the zirconia-based nanoparticles and most relevant for their practical use.^{361–368}

Pure bulk zirconia exhibits three structures in different ranges of temperature at atmospheric pressure (other different orthogonal-type structures can be stabilized at high pressure).³⁶⁹ The most stable thermodynamic form is monoclinic and transforms to unquenchable tetragonal and cubic (fluorite) structures at ca. 1400 and 2700 K (up to the melting point of ca. 2950 K), respectively.^{6,370} The stability of the monoclinic phase in the extended material has been explained on the basis of covalency effects since a simple ionic model is inadequate to explain the observed structures.³⁷¹ A significant consequence of decreasing the size of pure zirconia is the possibility of stabilizing the tetragonal phase for particles of less than ca. 30 nm.^{362,363} First approaches to this effect were given in the works of Garvie and Clearfield,^{362,363} while a survey of the work done earlier on this crystallite size effect is given in the review article of Garvie.³⁶⁵ Garvie advanced the hypothesis that the tetragonal form had a lower surface free energy than the monoclinic one, thereby explaining the spontaneous occurrence of the former structure below a certain critical size of the crystalline particle.³⁶² Later, it was proposed that the presence of internal stresses within the particles or agglomerates could be responsible or contribute to the stabilizing effect.^{364,365} Recent results based on neutron diffraction studies show the presence of such size-dependent strain in the nanoparticles pointing out that the stabilization of the tetragonal phase is related to the coupling between primary and secondary order parameters in the Landau free energy expansion, affected by both strain and surface free energy factors.³⁶⁵ The characteristics of the tetragonal–monoclinic transition in the nanoparticles are affected by a number of intrinsic or extrinsic factors such as the particle size, the pressure or the presence of phase stabilizers either in the bulk (usually as rare-earth cationic dopants with intrinsic defects associated to them) or at the surface (like water-derived or sulfate groups).^{365,372–379} In this sense, discrepancies observed in the literature with respect to the stabilization of either of the phases in the nanoparticles can be essentially attributed to differences at compositional (due to the presence of impurities) or morphological (within primary or secondary particle sizes, causing different intergrain stresses) levels between the samples.^{364,366} Whatever the case, it is agreed that the tetragonal–monoclinic transformation in nanosized pure zirconia is favored upon increasing the particle size or decreasing the pressure.^{372–375} Concerning morphologic and dynamic aspects of the phase transition, recent results comparing UV and visible Raman results show that the phase transformation takes place initially at the surface regions of the nanoparticles.^{380,381} Furthermore, it is proposed that stabilization of tetragonal phases at the surface of La- or Y-doped zirconia can prevent the phase transition from developing into the bulk of the material.³⁸¹ Concerning the cubic-to-tetragonal transformation in the nanoparticles, re-

cent results based on TEM observations point toward a ca. 2 nm critical size for the occurrence of such transformation.³⁸² In addition to strain and surface energy factors, the presence of anion vacancies is pointed out (with the help of first principles quantum-mechanical simulations) as an additional relevant factor in this transformation.³⁸²

Irradiation-induced changes in the structure of the materials is a field of large interest for the design of protective shields in the spacecraft industry or for the use of the materials in nuclear-derived irradiation environments, for which advantage can be taken of the refractory properties of zirconia.^{383,384} In this respect, an important particularity of zirconia nanoparticles with respect to the extended crystals is the fact that significant levels of amorphization can be induced in very small particles (ca. 3 nm average diameter), which can somewhat limit its use in the mentioned applications.³⁸³ This size-dependent difference is essentially attributed to the radiation-induced formation of accumulated oxygen vacancies in the material (proposed to be responsible of monoclinic \rightarrow tetragonal \rightarrow cubic transformations, without loss of the crystallinity in the extended system);³⁸⁴ the higher total free energy in the nanoparticles, as a consequence of the relatively higher surface free energy contribution, makes easier reaching a high free energy value (induced by the contribution of the formed defects) required to stabilize the amorphous state.³⁸³

As mentioned, stabilization of the tetragonal phase of zirconia can be achieved upon introduction of cationic dopants.^{378,385–387} Interestingly, and as expected from the above exposed results observed on pure zirconia, the minimum dopant content above which the tetragonal phase appears depends on the particle size, being clearly lower when employing nanometer-sized particles in comparison with micrometer-sized ones.³⁸⁵ The amount of dopant required for the tetragonal stabilization in the nanoparticles generally depends on the nature of the dopant; a comparative study employing different rare-earth M^{3+} dopants shows that it decreases with increasing the ionic size of the dopant.^{385–387} The nature of the dopant also affects the oxide ion conductivity in the nanoparticles, which, as observed for the extended systems,³⁸⁶ increases with decreasing the ionic radius of the rare-earth dopant.³⁸⁷

The use of zirconia nanoparticles as starting material in the preparation of dense oxygen permeation membranes presents advantages since they exhibit improved sintering behavior with almost full density being achieved at ca. 1273 K, 100–200 K lower than for microcrystalline powders.^{386,388} In addition, as pointed out for other oxide materials,³⁸⁹ unique transport properties have been shown for membranes constituted by nanograins of stabilized zirconia.^{390,391} Thus, in nanosized yttria-stabilized zirconia (YSZ), the activation energies of intragrain and grain boundary oxide ion conductivities were found to be slightly lower than in comparable microsize samples.³⁹⁰ In that case, the fact that both types of conductivities were in the same range as those of more extended samples indicated a 1–2 orders of magnitude higher

specific grain boundary conductivity than that of the microcrystalline samples. This enhanced conductivity has been mainly attributed to the presence of complete tetragonal structures in the nanoparticles and to the absence of appreciable amounts of Si impurities, which usually produce blocking effects in the intergrain boundary region.³⁸⁸ In the same sense, a 3 orders of magnitude higher oxygen diffusivity in the grain boundaries has been reported for nanocrystalline YSZ in comparison with extended single crystals.³⁸⁹ In contrast with these results, comparison of oxygen diffusivities between dense specimens constituted by grains of undoped monoclinic zirconia of either 80 or 300 nm indicated no important size-dependent differences on either intragrain or grain boundary diffusion coefficients, while the activation energies for either process were considerably higher than those observed in (doped) stabilized zirconia samples.³⁹²

Modification of the optical absorption properties upon decreasing particle sizes to sub-micrometric scale has also been observed.²³² An increase in the band gap energy observed for particles lower than 100 nm (0.25 eV shift upon decreasing the size to 1 nm) is well explained by quantum confinement effects (see expression 2.2.2.d) except for particles lower than ca. 10 nm; deviations in such a small size range are likely attributable to a crystalline \rightarrow amorphous transition occurring for such very low size particles.²³² Another approach for modification of the optical properties of zirconia (applied also for TiO_2 and Fe_2O_3) consists of surface modification of the nanocrystalline metal oxide particles with enediol ligands, resulting in red shifts of the optical absorption with respect to the unmodified nanocrystallite.³⁹³ Such shifts are found to be proportional to the density of delocalized π electrons and the dipole moment of the surface oxide–ligand complex, decreasing with the ligand size. Coupling of this ligand-dependent (ligand to metal oxide) charge-transfer interaction with the adjustable quantum size effects in the nanoparticles is interesting for tuning of electronic properties in frequency-selective photochemical applications. In turn, another possible application pointed out by Rajh et al., as a consequence of the observed ligand–metal oxide charge separation and its low temperature reversibility, is related to the use of the ligands as possible conducting leads that could eventually link the nanoparticle to molecular circuits.³⁹³

3.3. Ce-Containing Oxides

3.3.1. Pure Ceria Nanoparticles

Ceria (CeO_2) is an oxide with important applications in areas of catalysis, electrochemistry, photochemistry, and materials science.^{394,395} In its most stable phase, bulk CeO_2 adopts a fluorite-type $Fm\bar{3}m$ crystal structure in which each metal cation is surrounded by eight oxygen atoms.^{6,395} The band gap of pure ceria is ~ 5 eV,^{3,396} but crystal defects or impurities can transform the material in a good n-type semiconductor.³⁹⁵ Experimental and theoretical studies indicate that bulk CeO_2 is not a fully ionic oxide.^{397–401} Experiments of photoelectron spec-

troscopies and optical reflectivity measurements show a strong hybridization of the metal and oxygen orbitals,^{397–399} and the valence band, although dominated by O 2p character, still contains a significant amount of metal character.^{400,401} Thus, the charge on the metal cations is probably much smaller than the formal value of “+4” frequently assigned,^{400,401} and CeO₂ is best described as an ionocovalent compound or covalent insulator.^{399,401} One of the most interesting properties of ceria is its ability to undergo a facile conversion between “+4” and “+3” formal oxidation states.⁸ Because of this, ceria is a key component in the so-called three-way catalysts (TWC) commonly used to reduce the emissions of CO, NO_x, and hydrocarbons from automobile exhaust,⁴⁰² or is used as a base material of electrolytes and electrodes in solid oxide fuel cells.^{358,394} Ceria-supported noble-metal catalysts are capable of storing oxygen under oxidizing conditions and releasing oxygen under reducing conditions through a transformation between “Ce⁴⁺” and “Ce³⁺” oxidation states.⁴⁰³

In the area of catalysis, nanoparticles of ceria have been studied since the early 1970s, but they were poorly characterized.^{402,403} In recent years, substantial progress has been made thanks the use of better synthetic methods and sophisticated techniques for characterizing structural and electronic properties.^{404–409} In a theoretical study from the mid 1990s, simulated annealing and interionic potentials were used to investigate the structure and reducibility of ceria nanoparticles (Ce_nO_{2n}, $n = 2–50$).³⁰⁹ The lattice energy decreased with increasing n . Only for the largest nanoparticles was the fluorite structure clearly observed. Small nanoparticles exhibited a nearly amorphous structure. In general, the energy required to reduce the Ce_nO_{2n} systems increased with particle size, but large fluctuations were also observed. The reduction of the ceria nanoparticles was structure sensitive, being easier in systems that had a low degree of crystallinity.³⁰⁹ Several of these theoretical predictions have been verified by subsequent experimental studies, as we will see below.

It is not easy to find synthetic methods that allow the preparation of ceria nanoparticles that are small (<3 nm) and have a narrow distribution of sizes.^{404,405,407} This makes difficult a direct comparison between experiment and theory.³⁰⁹ But, experimentally, it is known that very small particles of ceria may deviate from the fluorite structure of the bulk oxide.^{125,410} For particles that are a little bit larger (4–7 nm), measurements of XAS, Raman, and XRD would suggest the existence of local distortions on the cubic fluorite structure as a consequence of defects in the oxide lattice.^{76,406,408,411} Depending on the method of preparation, and, particularly, of the Ce oxidation state of the precursor salt, the content of O vacancies and concomitant presence of Ce³⁺ in a ceria nanoparticle can change; this has been shown by using Raman and XRD.^{29,404,405,407} Since “Ce³⁺” is significantly bigger than “Ce⁴⁺” (atomic sizes 1.14 and 0.97 Å, respectively),⁴¹² the presence of O vacancies increases the size of the unit cell,^{76,409} and can distort it.^{406,407} In addition to O vacancies, other structural imperfections as well as surface effects can be present

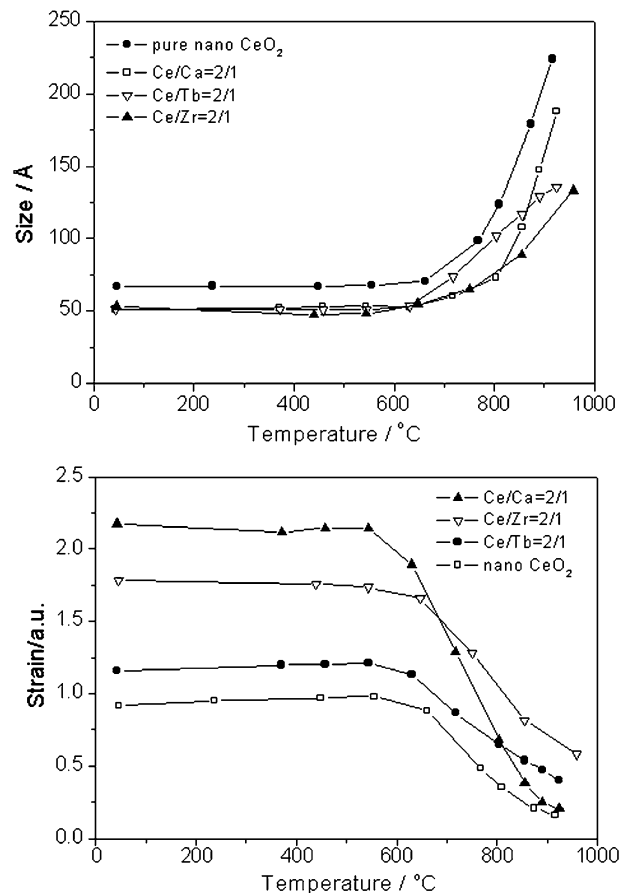


Figure 12. Size (top) and strain (bottom) for nanoparticles of CeO₂, Ce_{0.66}Ca_{0.33}O₂, Ce_{0.66}Tb_{0.33}O₂, and Ce_{0.66}Zr_{0.33}O₂ as a function of temperature. From ref 32. Copyright 2004 American Institute of Physics.

in a ceria nanoparticle introducing strain in the lattice.^{29,413} Part of this strain can be removed by annealing at high temperatures, but sintering may concomitantly occur.^{409,413} Figure 12 shows results of time-resolved XRD for the heating of ceria nanoparticles in air.^{409,413} This experiment was similar to that shown in Figure 3 (section 2.1.1). Initially, the size of the ceria nanoparticles was ~7 nm (top panel in Figure 12) and remained constant up to ~600 C when sintering started. In this case, the starting material is fully oxidized, and Ce³⁺ was below the detection limit of XANES.²⁹ The sintering was accompanied by a substantial reduction in the strain. Defects such as dislocations, edges, or cuts were probably removed during the sintering process. The O vacancies and defects present in ceria nanoparticles can lead to special electronic properties, introducing electronic states within the band gap of the oxide.^{401,409} Ceria particles with diameters of less than 10 nm have a substantially higher electronic conductivity than bulk ceria⁴¹⁴ (see details in section 4.1).

Bulk ceria is able to absorb and store hydrogen.^{415,416} Ceria nanoparticles have the same property.^{76,409} The absorption of hydrogen causes an expansion in the lattice constant of the oxide detected by using XRD. Theoretical calculations (DFT) indicate that the H atoms do not remain at a high-symmetry position in the center of the cavities of the ceria lattice but instead move toward the O sites forming hydroxyl species.^{76,416} These species can be

seen as the precursors for the removal of oxygen during a reduction process. Results of temperature-programmed reduction and time-resolved XRD indicate that ceria nanoparticles are reduced at temperatures that are lower than those seen for the reduction of bulk ceria.⁷⁶ This is consistent with the prediction of theoretical studies.³⁰⁹ During the reduction process, before the appearance of Ce_2O_3 , there is a substantial expansion in the unit cell of the CeO_2 nanoparticles as a consequence of the embedding of hydrogen and the formation of O vacancies.⁷⁶

3.3.2. Ce-Containing Mixed-Metal Oxides

The performance of ceria in automotive catalysts and fuel cells can be enhanced by doping this oxide with a second metal ($M = \text{Zr}, \text{Ca}, \text{Cu}, \text{Au}, \text{Pt}, \text{Tb}, \text{La}, \text{Mn}, \text{etc.}$).^{417–419} Mixed-oxides maintain fluorite-type structures, particularly the cation sublattice, up to a high level of doping. The doping element in many cases enhances the thermal stability of the support system or favors the transport of oxygen (conversion between “ Ce^{3+} ” and “ Ce^{4+} ” oxidation states). In some situations, the doped-ceria nanoparticles become very active catalysts for reactions such as the water–gas shift or the destruction of SO_2 .^{403,417} This effect is achieved by doping with noble metals such as Cu, Au, or Pt, and the phenomenon is not fully understood.^{420–422} However, as described below, these properties of ceria-based systems are mainly driven by two physicochemical phenomena: the local M–O ordering and distance and the way the systems achieve charge neutrality, which in the case of ceria is mainly through the presence of oxygen vacancies.

The CeO_2 – ZrO_2 system is one of the most studied mixed-metal oxides in the literature due to its important role in the operation of automotive catalysts.^{394,402,403} To enhance the redox properties and thermal stability of pure ceria, zirconia (ZrO_2) is often mixed as an additive to form solid solutions of the $\text{Ce}_{1-x}\text{Zr}_x\text{O}_2$ type ($x \approx 0.5$).^{423–425} Typically, cations are randomly distributed in a cubic-type subcell, whereas the total symmetry is governed by the anion subcell.⁴⁰³ For these materials, several tetragonal (called t, t', t'') and cubic (c) structures are possible.^{403,411,412} The work of Yashima et al.⁴²⁶ indicates the presence of t'/t'' metastable phases for Ce:Zr atomic ratios near to unity, which are presumed to be stabilized by particle size (surface) effects in the nanometer regime (below ca. 15 nm).⁴²⁷ In some cases, the mixed oxide lacks complete homogeneity, having microregions where the content of Ce or Zr varies from the overall average composition,⁷² while in others it seems to have reasonable homogeneity.⁴²⁸ Homogeneity at a local scale seems a crucial (although not unique) parameter to get improved thermal stability. Figure 3 (section 2.1.1) shows XRD data for $\text{Ce}_{0.9}\text{Zr}_{0.1}\text{O}_2$ nanoparticles as a function of temperature.⁷⁶ Similar results were found for $\text{Ce}_{0.66}\text{Zr}_{0.33}\text{O}_2$ and $\text{Ce}_{0.5}\text{Zr}_{0.5}\text{O}_2$ systems.⁷⁶ Table 2 lists room temperature lattice constants determined from a Rietveld refinement of XRD data for CeO_2 and $\text{Ce}_{1-x}\text{Zr}_x\text{O}_2$ nanoparticles.⁷⁶ The small size of these systems puts a limit on the accuracy of the structural analysis, and the “a” parameters listed in some cases in fact represent an

Table 2. XRD Results for $\text{Ce}_{1-x}\text{Zr}_x\text{O}_2$ at 25 °C^a

| compound | lattice constant, a (Å) |
|--|---------------------------|
| CeO_2 | 5.40 (5.41) ^b |
| $\text{Ce}_{0.9}\text{Zr}_{0.1}\text{O}_2$ | 5.40 |
| $\text{Ce}_{0.66}\text{Zr}_{0.33}\text{O}_2$ | 5.36 |
| $\text{Ce}_{0.5}\text{Zr}_{0.5}\text{O}_2$ | 5.31 |

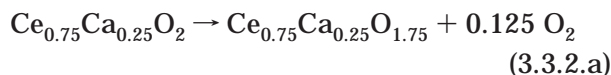
^a From ref 76. Errors in lattice constant < 0.01 Å. ^b XRD value for bulk CeO_2 .

average value for a pseudocubic phase with a slight tetragonal distortion.⁷⁶ In Table 2, as the content of Zr increases, there is a reduction in the lattice constant of the oxide. An identical result has been found in XRD studies for bulk $\text{Ce}_{1-x}\text{Zr}_x\text{O}_2$.^{411,419} The lattice constant decrease is a consequence of the small size of “ Zr^{4+} ” (0.87 Å) with respect to “ Ce^{4+} ” (0.97 Å).⁴¹² DFT calculations indicate that this difference in size is quite important for the local structure of the metal cations.⁷⁶ Even within a cubic structure, the Zr atoms exhibit different types of Zr–O distances and nonequivalent O atoms in the $\text{Ce}_{1-x}\text{Zr}_x\text{O}_2$ compounds. In essence, it is very difficult for the Zr atoms to adopt the large metal–oxygen distances expected in the lattice of CeO_2 . Upon the addition of Zr to CeO_2 , the Zr positive charge in $\text{Ce}_{1-x}\text{Zr}_x\text{O}_2$ is smaller than in pure ZrO_2 , whereas the Ce positive charge is larger than in pure CeO_2 . The combination of these geometrical and electronic effects produces Zr L_{III}-edge and O K-edge XANES spectra with a distinctive line-shape not seen in pure ZrO_2 or CeO_2 .⁷⁶ The perturbations in the Zr–O coordination sphere could be responsible for the high oxygen mobility seen in ceria–zirconia mixed oxides.^{412,419}

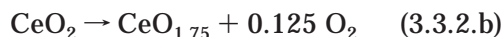
In Figure 3 (section 2.1.1), the diffraction lines clearly gain intensity and become better defined when the temperature is raised. No phase transformation is visible. From the change in the width of the diffraction lines, one can see that around 600 °C a sintering process starts. This is accompanied by a decrease of the strain in the lattice of the $\text{Ce}_{1-x}\text{Zr}_x\text{O}_2$ nanoparticles (for a typical case, see Figure 12).^{76,413} Apart from thermodynamic reasons, some additional kinetic factors in turn related to morphological properties (porosity and secondary particle size) of the material are of relevance in limiting crystal growth and therefore in the thermal stability of the nanostructured metastable phases.⁴²⁷ In general, the results of time-resolved XRD indicate that doping with Zr enhances the thermal stability of ceria nanoparticles.^{76,413} This is true even in the presence of hydrogen as a reducing agent.⁷⁶

One problem of Zr as a doping agent is the fact that it induces a very limited concentration of O vacancies in the ceria nanoparticles⁷⁶ and, thus, has a moderate effect on the redox properties of the system under oxidizing environment. To improve this aspect, one can try doping using Ca.^{409,429} The introduction of Ca into a CeO_2 – ZrO_2 oxidic network strongly modifies surface and bulk oxygen handling properties,⁴¹⁸ and CaO– CeO_2 catalysts are used for the destruction of SO_2 .⁴²⁹ The radii of atomic Ca (1.97 Å) and the “ Ca^{2+} ” cation (1.06 Å) are somewhat bigger than the corresponding radii of atomic Ce (1.83 Å) and the “ Ce^{4+} ”

cation (0.97 Å).⁴³⁰ According to formal oxidation states, a charge imbalance is produced in $\text{Ce}_{1-x}\text{Ca}_x\text{O}_2$ after replacing “ Ce^{4+} ” ions with “ Ca^{2+} ” ions.^{409,429} In principle, this should induce the formation of O vacancies. However, the situation is more complex, because the $\text{Ce}_{1-x}\text{Ca}_x\text{O}_2$ systems are far from being fully ionic.⁴⁰⁹ Cation charges derived from DFT calculations indicate that these systems obey the Barr model^{431,432} for charge redistribution in mixed-metal oxides. The Ca atoms in $\text{Ce}_{1-x}\text{Ca}_x\text{O}_2$ are more electropositive than the cations in CaO, while the Ce cations of $\text{Ce}_{1-x}\text{Ca}_x\text{O}_2$ are less electropositive than those of CeO_2 .⁴⁰⁹ These trends are consistent with XANES measurements at the Ca K- and Ce L_{III}-edges.⁴⁰⁹ When taking a metal cation from a CaO matrix into a CeO_2 matrix, a gain in lattice strain occurs due to differences in metal–oxygen bond distances and in the number of oxygen neighbors per metal cation.⁴⁰⁹ All these electronic and structural perturbations favor the creation of O vacancies. DFT calculations⁴⁰⁹ and molecular dynamics simulations⁴²⁹ indicate that the formation of O vacancies in $\text{Ce}_{0.75}\text{Ca}_{0.25}\text{O}_2$



is a much more exothermic reaction than the formation of O vacancies in CeO_2



Consistent with this prediction, the analysis of XRD/Thermogravimetric data for $\text{Ce}_{0.8}\text{Ca}_{0.2}\text{O}_2$ and $\text{Ce}_{0.66}\text{Ca}_{0.33}\text{O}_2$ nanoparticles proves that their real compositions are $\text{Ce}_{0.8}\text{Ca}_{0.17}\text{O}_{1.82}$ and $\text{Ce}_{0.66}\text{Ca}_{0.29}\text{O}_{1.72}$, respectively.⁴⁰⁹

The XRD results show that doping with calcium leads to slightly distorted tetragonal structures, with relatively minor variations (<0.025 Å) in the cell dimensions of ceria.^{409,429} In a ceria lattice, the presence of Ca (associated with O vacancies) introduces a larger strain than the presence of Zr (for an example, see results for $\text{Ce}_{0.66}\text{Zr}_{0.33}\text{O}_2$ and $\text{Ce}_{0.66}\text{Ca}_{0.33}\text{O}_{1.72}$ in the bottom panel of Figure 12). This can be problematic at high temperatures.⁴⁰⁹ For $\text{Ce}_{1-x}\text{Ca}_x\text{O}_{2-x}$ nanoparticles that contain a substantial amount of Ca ($x > 0.2$), experiments of time-resolved XRD (for an example see Figure 13) show new diffraction lines around 750 °C due to the segregation of CaO.⁴⁰⁹ The “expulsion” of the Ca from the ceria lattice causes a significant drop in the strain of the system that is not seen during the annealing of $\text{Ce}_{1-x}\text{Zr}_x\text{O}_2$ nanoparticles (Figure 12), where there is no phase segregation up to temperatures above 1000 °C.

For technological applications at high temperature, one wants a dopant agent that introduces a reasonable amount of O vacancies in the lattice of ceria and produces a mixed-metal oxide that has a high thermal stability.³⁹⁴ The compromise between these two properties depends on a significant number of variables. In any case, doping with Zr or Ca fully satisfies only one of these two requirements. Doping with Tb and other lanthanides as Pr may be a solution to this

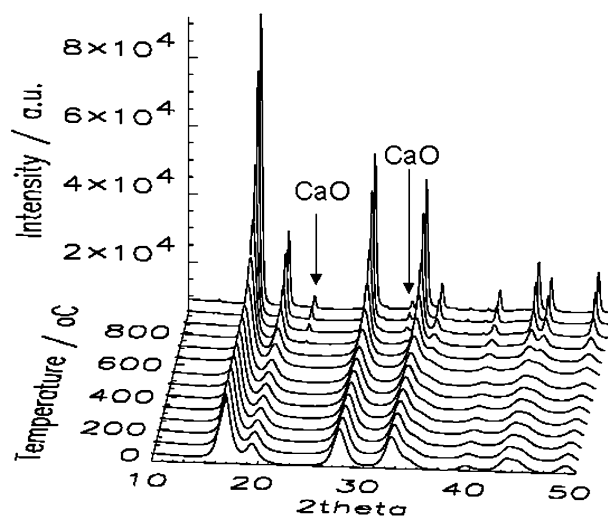


Figure 13. Time-resolved XRD results obtained after heating a sample of $\text{Ce}_{0.66}\text{Ca}_{0.33}\text{O}_2$ nanoparticles from 25 to 925 °C. Heating rate = 6 °C/min. Reprinted with permission from ref 409. Copyright 2003 American Institute of Physics.

Table 3. XRD results for $\text{Ce}_{1-x}\text{Tb}_x\text{O}_2$ at 25 °C^a

| compound | lattice constant, <i>a</i> (Å) |
|---|--------------------------------|
| CeO_2 | 5.40 |
| $\text{Ce}_{0.9}\text{Tb}_{0.1}\text{O}_2$ | 5.38 |
| $\text{Ce}_{0.66}\text{Tb}_{0.33}\text{O}_2$ | 5.36 |
| $\text{Ce}_{0.5}\text{Tb}_{0.5}\text{O}_2$ ^b | 5.34 |

^a From ref 32. Errors in lattice constant < 0.01 Å. ^b The actual composition is $\text{Ce}_{0.5}\text{Tb}_{0.5}\text{O}_{1.76}$.

complex problem.^{127,413,433} In the case of Tb, the relative stabilities of the “ Tb^{3+} ” and “ Tb^{4+} ” states favor the formation of O vacancies in $\text{Ce}_{1-x}\text{Tb}_x\text{O}_2$. In Table 3 are listed room temperature lattice constants determined from a Rietveld refinement of XRD data for CeO_2 and $\text{Ce}_{1-x}\text{Tb}_x\text{O}_2$ nanoparticles.³² Terbium produces a small decrease in the lattice constant of the ceria host. The $\text{Ce}_{0.5}\text{Tb}_{0.5}\text{O}_2$ sample is expected to have the highest concentration of O vacancies, and an XRD analysis shows that its real composition is $\text{Ce}_{0.5}\text{Tb}_{0.5}\text{O}_{1.76}$.³² Ternary oxides with presence of La or Y seems also good candidates to achieve optimal properties.⁴³⁴

Structural properties for nanoparticles of CeO_2 , $\text{Ce}_{0.66}\text{Zr}_{0.33}\text{O}_2$, $\text{Ce}_{0.66}\text{Ca}_{0.33}\text{O}_2$, and $\text{Ce}_{0.66}\text{Tb}_{0.33}\text{O}_2$ are compared in Figure 12.^{32,76,409} All the samples start to sinter at temperatures above 600 °C (top panel). The agglomeration rate determined by the slope increased following the order: $\text{Ce}_{0.66}\text{Zr}_{0.33}\text{O}_2 < \text{Ce}_{0.66}\text{Tb}_{0.33}\text{O}_2 < \text{Ce}_{0.66}\text{Ca}_{0.33}\text{O}_2 \approx$ nano ceria. This indicates that both Tb and Zr cations improve the thermal stability of the ceria nanoparticles, while Ca cations did not. A strain comparison is shown in the bottom panel of Figure 12. Interestingly, the magnitude of the strain at room temperature increases according to the sequence: $\text{Ce}_{0.66}\text{Ca}_{0.33}\text{O}_2 > \text{Ce}_{0.66}\text{Zr}_{0.33}\text{O}_2 > \text{Ce}_{0.66}\text{Tb}_{0.33}\text{O}_2 >$ nano ceria. A reduction in the strain begins to occur at around 600 °C, and it is larger for the $\text{Ce}_{0.66}\text{Ca}_{0.33}\text{O}_2$ due to phase separation (see Figure 13).⁴⁰⁹ Among the three types of doped ceria nanoparticles in Figure 12, the Tb-doped system has an intermediate thermal stability and concentration of

O vacancies.³² The combination of these two properties makes Tb-doped ceria nanoparticles special for applications in automotive catalysts.

In addition, pure ionic conduction can be achieved upon doping of ceria with M^{3+} cations. In particular, doping with Gd^{3+} has shown important applications as oxygen conduction membranes in solid oxide fuel cells.³⁵⁸ Some aspects of particle size effects on the electrical conduction properties of Ce–Gd mixed oxides will be treated in section 4.1.

3.4. MgO and Other Alkaline-Earth Oxides

Magnesium oxide (MgO) is widely used in the chemical industry as a scrubber for air pollutant gases (CO_2 , NO_x , SO_x) and as a catalyst support.⁴³⁵ It exhibits a rock salt structure like oxides of other alkaline earth metals.⁶ The nonpolar (100) face is by far the most stable surface,^{436,437} and particles of MgO usually display a cubic shape. For example, when Mg metal is burned in air or oxygen, the MgO smoke particles that are formed are almost perfect cubes having (100) faces.⁴³⁸ Special procedures to prepare MgO nanoparticles exhibiting (110) and (111) faces have been partially successful,⁴³⁹ but in general they tend to facet to surfaces containing (100) planes.⁴⁴⁰ The rock salt (110) surface is also nonpolar, but its surface energy is twice that of a (100) surface.^{436,439} In the case of a (111) surface, the situation is more complex because it will contain either a layer of Mg cations or a layer of O anions. Neither of these planes is charge neutral (a net dipole moment exists).¹ Thus, MgO nanoparticles exhibiting (111) faces are intrinsically unstable and should undergo a structural transformation.

Recently, highly porous (~90%), high-surface area (~1000 m²/g), thermally stable (1200 K) crystalline films of magnesium oxide nanostructures were prepared using a novel ballistic deposition technique (a collimated atomic beam of Mg was deposited on a silica support under a background pressure of O₂).⁴⁴¹ The films consisted of a tilted array of porous nanoscale crystalline filaments. Surprisingly, the individual filaments exhibited a high degree of crystallographic order with respect to each other.⁴⁴¹ The films had chemical binding sites analogous to those of MgO(100) surfaces. However, the fraction of chemically active, high-energy binding sites was greatly enhanced on the nanoporous film. Such properties make these materials attractive candidates for applications as sensors and heterogeneous catalysts.⁴⁴¹

In its bulk state, MgO is a highly ionic compound and a wide band gap (~7 eV) insulator. For small nanoparticles of MgO, a reduction in the band gap could be measured by using optical absorption techniques.^{1,41,42} and the effects of the electrostatic Madelung potential could not be as strong as those in bulk MgO.^{37,38} The Mg cations in a (100) face are penta-coordinated and have a charge that is close to that found for the cations in the bulk.⁴¹ These atoms are expected to have a low activity^{37,38,41,42} and may not be of interest in chemical applications of MgO nanoparticles. On the other hand, Mg atoms located at corner or edge sites of MgO nanoparticles have a

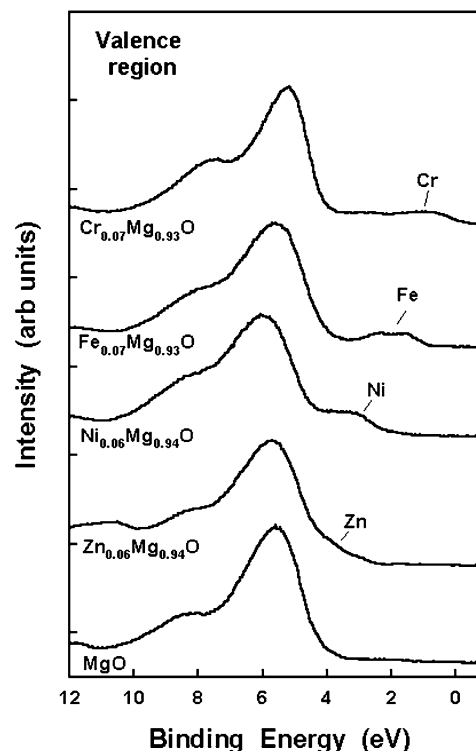


Figure 14. Valence photoemission spectra for pure and doped magnesium oxide. Reprinted with permission from ref 454. Copyright 2001 American Institute of Physics.

relatively low coordination number and a positive charge that is substantially smaller than that in the bulk.^{41,42} These cations are expected to be the chemically active sites of the nanoparticles.^{442,443}

An important aspect to consider when dealing with MgO nanoparticles is the possible presence of O vacancies.⁴⁴⁴ These can have a tremendous influence on the electronic and chemical properties of the nanoparticles. The anionic vacancies in MgO are known as F centers; depending on the charge one can have F, F⁺, and F²⁺ centers which correspond to the removal of a neutral O atom, of an O⁻ or of an O²⁻ anion, respectively.⁴⁴⁴ The F centers can be described as an electron pair trapped in the cavity left by the missing oxygen.⁵⁵ They can produce electronic states localized well above the valence band of MgO.⁴⁴⁵ The F⁺ centers consist of a single electron associated with the vacancy and give rise to a typical signal in EPR.⁴⁴⁶ Finally, F²⁺ centers are strongly electron deficient and have a tendency to ionize bonded molecules.⁴⁴⁷

For several industrial applications MgO is doped with small amounts of a transition metal.⁴³⁵ Such doping can induce structural transformations and be used to stabilize MgO nanoparticles that expose (110) or (111) faces.⁴⁴⁰ The doping also can lead to perturbations in the electronic properties of the nanoparticles by favoring the formation of O vacancies or by introducing new occupied states above the valence band of MgO as shown in Figure 14.⁴⁴⁸ The position of the new occupied states depends on the nature of the dopant element. This phenomenon is particularly important when the doping is done with metals such as Fe or Cr that induce states 2–3 eV above the MgO valence band. In general, the $TM_xMg_{1-x}O$ systems

(TM = Ni, Fe, Mn, Cr) exhibit electronic and chemical properties different from those of pure MgO.^{449–455}

Recently, the preparation of nanoparticles of CaO and BaO is receiving a lot of attention due to their potential use in the control of NO_x emissions from automotive engines.^{456,457} As in the case of MgO, nanoparticles of CaO and BaO usually prefer to adopt a nearly perfect or somewhat distorted cubic shape, exposing the (100) face of a rock salt crystal structure.^{52,458,459} Nanoparticles exhibiting (110) and (111) faces are much less common and are not stable at high temperatures.⁴⁴⁰ In nanoparticles of CaO and BaO, the chemical activity is mainly associated with Ca, Ba, or O atoms located at corner or edge positions in the cubic structure.^{460,461}

3.5. Other Oxides

Nanostructures have been prepared for many oxide systems, but they have not been studied in a systematic way as described above for nanoparticles of TiO₂, ZrO₂, CeO₂, and MgO. Some additional interesting cases will be discussed in this section. Here we will briefly describe some sparse work devoted to other single oxide systems containing Al, Fe, Sn, Ni, and Zn. Much less is known for nanostructured mixed oxides, although a recent review on the catalytic use of solid solutions has been published.⁴⁶²

Attention in the Al–O system is centered on the Al₂O₃ stoichiometry due to its importance as a catalyst component or absorbent and ceramic material in a multitude of industrial processes. There are seven Al₂O₃ polymorphs, although only four, called α , δ , θ , and γ , are typically involved in such processes.⁴⁶³ The γ -Al₂O₃ is the nanostructured phase commonly yielded by most synthetic methods but also the α -Al₂O₃ polymorph is now synthesized having high surface area.²⁰ The corundum, α -Al₂O₃ structure is the bulk thermodynamically stable phase, but the calorimetry work of McHale et al.²⁰ gives conclusive evidence that γ -Al₂O₃ has a lower surface energy and becomes energetically stable at size below a point close to 10 nm (surface BET area ca. 75 m² g⁻¹). They also showed the importance of surface hydroxyls or water molecules in the energetics of surfaces.^{20,464} The surface characteristics of the gamma phase have been extensively studied by Knozinger and Ratnasamy.⁴⁶⁵ This polymorph suffers a complex phase excursion in reaching the alpha phase by increasing the temperature; the delta alumina is typically observed between 973 and 1273 K, evolving in the theta phase, which finally yields the alpha polymorph at temperatures between 1273 and 1373 K. The γ - δ - θ transformation occurs topotactically with extensive sintering and loss of surface area but maintaining the fcc cubic packing of the oxygen sublattice. This complex transformation has been theoretically addressed, confirming the simple idea that occurs through aluminum atom migration while oxygen atoms remain essentially fixed.⁴⁶⁶ The number and nature of the intermediates as well as the temperature(s) of the γ -to- θ transformation depends on a wide number of parameters as the nature of the precursors or preparation pH⁴⁶⁷ and, certainly, the initial size of the gamma phase.⁴⁶⁸ The α phase is obtained by a

nucleation growth mechanism by which the key step is the anion packing reordering from the cubic to a hexagonal structure.^{20,464,465} The analysis of the $\theta \rightarrow \alpha$ phase transformation mechanism, whether it is a shear mechanism with the shear in an oxygen lattice direction or a diffusional one as a part of the typical “nucleation and growth” model mechanism, has the subject of many studies and recently reviewed.⁴⁶⁹ Temperature of phase transformation to end into the alpha phase and the presence of some of the mentioned intermediates phases not only depend on size but also on the presence of impurities as Si⁴⁷⁰ or presence of surface stabilizers.⁴⁰⁵ Doping is an obvious route to modify all the phase transformations mentioned, presumably by the initial occupation of some interstitial positions of the polymorphs, altering in this way the above-mentioned cation movement paths⁴⁶⁶ and being progressively at the surface layer of grain boundaries of the material as the temperature increases. Typically, Ti and Mg do not alter the temperature of the phase transformation⁴⁷¹ while Y, Zr,⁴⁷¹ Er,⁴⁷² Ba, La, and Pr⁴⁷³ delay it, and Fe,⁴⁷⁴ Y, and Cr⁴⁷¹ decrease it. As already noted for other oxides, the K, Ba, or La presence at the surface is also known to retard the phase transformation to alpha; the exact mechanism depends primarily on the heteroatom concentration as above a certain limit the occurrence of binary phases is detected.^{471,475} An alternative method to control the phase transformation temperature and alpha primary particle size involves the seeding of the starting material with well-controlled nanosized germs of the alpha polymorph.⁴⁷¹ Unfortunately, full details of the influence of all these variables in the phase behavior have not been addressed to date, although some attempts are reported.^{468,469,471}

Fe and O form a number of phases, e.g., FeO (wustite), Fe₃O₄ (magnetite), α -Fe₂O₃ (hematite), γ -Fe₂O₃ (maghemite), and ϵ -Fe₂O₃.⁴⁷⁶ The latter two phases are synthetic while remaining oxides occur in nature. The Fe–O phase diagram shows the predominance of the Fe₂O₃ stoichiometry for most temperature and pressure preparation conditions.⁴⁷⁷ The magnetic properties of the Fe oxides have been extensively studied, in particular, the enhancing magnetic recording properties of magnetite⁴⁷⁸ and maghemite⁴⁷⁹ for nanostructured materials or the use of the latter in Fe₂O₃–SiO₂ composite materials having magneto-optical properties^{480,481} should be here mentioned. Most physicochemical studies are centered on the alpha (corundum structure with a distorted hexagonal anion closed-packed) and gamma (cubic inverse spinel) phases.^{27,205,478,480,482} As occurs with Ti-containing oxides, it appears that the presence of some anions, like Cl⁻, strongly favors the production of a specific polymorph, γ -Fe₂O₃,²⁰⁵ while nitrate precursors yielded γ -Fe₂O₃.^{480–482} at low concentration of the precursor in the preparation solution but a mixture of these two phases at higher concentrations.²⁷ A significant difference between these two polymorphs comes from their surface structure as measured by XAS techniques. In the case of the alpha phase, Fe surface ions have a lowered local symmetry (possibly 5-fold coordinated)

from the C_{3v} of the bulk,²⁰⁵ while the gamma phase appears to have minimal modifications at the surface, even though two different local symmetries (O_h ; T_d) can be encountered in such a polymorph,⁴⁸² one of which would be likely favored at the surface. The γ - Fe_2O_3 converts to the alpha phase at rather low temperatures, above 623 K,^{27,483,484} by a shear mechanism,⁴⁷¹ and the incorporation of gamma nanoparticles in polymeric, ceramic, or glassy matrixes have been shown to stabilize the thermal evolution of the maghemite polymorph.^{481,482} The influence of dopants has been also addressed in a few cases.⁴⁸⁵ However, the influence of size, which is certainly presumed in the above-mentioned stabilization mechanism, has not been fully addressed to date.

Nickel oxide is a magnetic insulator⁴⁸⁶ and a well-known catalyst²⁶ that prefers a cubic rock salt structure in its bulk state. Studies of STM for the deposition of NiO films on a Ag(100) substrate show that at submonolayer coverages the oxide overlayer can form 2D planar structures instead of three-dimensional cubic particles.⁴⁸⁷ The results of theoretical studies have shown that this behavior is not a consequence of interactions between the oxide and silver but an intrinsic property of NiO nanoparticles and nanostructures.²⁶ Thus, clusters that range in size from Ni_4O_4 to $\text{Ni}_{32}\text{O}_{32}$ are more stable as planar layers than as nearly perfect cubic structures. Surface properties of NiO and CuO nanoparticles with respect to the bulk materials have also been analyzed.⁴⁸⁸

Tin (IV) oxide adopts the tetragonal rutile structure (cassiterite in its mineral form) with the (110) surface being the most stable one.^{57,489–491} SnO_2 is a semiconductor with a direct but forbidden wide band gap of ca. 3.6 eV.⁴⁹² The presence of oxygen deficiency in the nominally pure material induces n-type conductivity attributable to the appearance of shallow donor levels at ca. 0.03 and 0.15 eV below the conduction band.⁴⁹³ Tin oxide is widely applied (in association with other metals to improve gas selectivity) as a sensor component, which is a consequence of the high sensitivity of its conductivity to the surrounding atmosphere.⁴⁹⁴ Another application of SnO_2 -based materials is in selective oxidation catalysis, in particular when combined with Sb.⁴⁹⁵ Achievement of nanostructured configurations in the tin oxide particles is of high relevancy for both types of applications, in which the surface properties play a major role.^{489,494–496} Thus, higher sensitivities and lower operation temperatures have been shown to be achieved upon lowering the particle size to the nanoscale in SnO_2 -based sensors.^{493,497} Such properties are closely related to strong variations of the surface electrical conductivity with deviation from stoichiometry.⁴⁹³ In fact, nonstoichiometric surface layers of about 1-nm thick (with crystalline stoichiometric cores) are proposed to be present in SnO_2 nanoparticles from Raman results.⁵⁷ On the other hand, the variation observed in the electrical conductivity with oxygen pressure ($P^{-1/4}$ dependence) is compatible with singly ionized oxygen vacancies as the main structural defect in SnO_2 nanoparticles.⁴⁹⁴

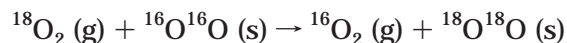
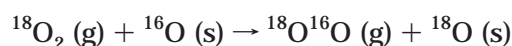
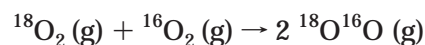
Zinc oxide presents the wurtzite structure.¹¹⁷ ZnO nanostructures have applications in luminescent devices, photocatalysis, photoelectrochemistry, and nonlinear optical devices.^{117,498,499} Surface and quantum size effects have been described as responsible of compressive strain and band gap blue shift in nanostructured ZnO particles.^{53,228,230} Improvement of the photocatalytic activities in the nanosized system has been attributed to the formation of surface defects such as oxygen deficiencies and hydroxyl groups.⁴⁹⁹

4. Physicochemical Properties

4.1. Charge-Related Phenomena: Transport and Photochemistry

4.1.1. Transport Properties and Techniques Employed for their Analysis

Gas–solid isotopic exchange makes use of ^{18}O labeled molecules, mainly O_2 and CO_2 , and analyzes the exchange process between such isotopomer and the $^{16}\text{O}^{2-}$ ions of the oxide. From the work of Boresov⁵⁰⁰ and Novakova,⁵⁰¹ it is known that three different processes can be detected: (a) homoexchange (mechanism I or R^0), occurring without participation of the oxide, (b) simple heteroexchange (mechanism R^1 or R') with participation of one oxide ion, and (c) multiple heteroexchange (mechanism R^2 or R''), which involves two oxygen ions of the solid. In the case of using oxygen as the tracer molecule, these three processes are described by the following three equations:



where suffixes g and s refer to the gas and solid phases, respectively. The overall rate constant of the exchange process, K , is usually defined by the sum of the three process rates, while the exchange rate constant, R , is the sum of the individual rate constants of R^1 and R^2 mechanisms. In metal oxides, the rate constants of the isotopic exchange published so far are either the overall or some individual rate constants.^{500–504} More importantly, from these data it appears that most of the oxides display exchange activity through the three mechanisms, with relative weights depending on the temperature of the experiment, while V_2O_5 , δ - VOPO_4 , CeO_2 and, in specific conditions, CuO and Ag_2O , appear to be the only cases dominated by the R^2 mechanism. This difference could be related to the presence/stability of binuclear O_2^- or O_2^{2-} species at the solid surface and their exchange with vacancy clustering centers of the metal oxide at relatively low temperatures.⁵⁰⁵

Using isotopic exchange, a considerable effort has been dedicated to the measurements of oxygen diffusivities in metal oxides, either by analyzing the exchange rate with the gas phase as a function of

Table 4. Oxygen Surface (D_s) and Bulk (D_b) Diffusion Coefficients Measured for Metal Oxides^a

| metal oxide | D_s (cm ² s ⁻¹)/T (K) | D_b (cm ² s ⁻¹)/T (K) | ref |
|---|--|--|----------|
| SiO ₂ | $3 \times 10^{-24}/673$ | | 508 |
| γ -Al ₂ O ₃ | $2 \times 10^{-22}/673$ | $7 \times 10^{-27}/723$ | 508 |
| MgO | $1 \times 10^{-21}/673$ | | 508 |
| ZrO ₂ | $(2-6) \times 10^{-18}/673$ | $\approx 1 \times 10^{-24}/673$ | 508, 510 |
| PdO | | $(1-20) \times 10^{-18}/573-673$ | 507 |
| CeO ₂ | $6 \times 10^{-20}-8 \times 10^{-22}/673$ | $4 \times 10^{-20}/573; 5 \times 10^{-26}/623$ | 127, 508 |
| CeO ₂ /Al ₂ O ₃ | | $4 \times 10^{-22}/673$ | 508 |
| Ce _{0.5} Zr _{0.5} O ₂ | | $8 \times 10^{-20}/573$ | 418 |
| Ce _{0.9} Ca _{0.2} O _{1.8} | | $2 \times 10^{-21}/573$ | 511 |
| Ce _{0.66} Ca _{0.33} O _{1.67} | | $8 \times 10^{-21}/573$ | 511 |
| Ce _{0.8} Tb _{0.2} O _{1.8} | | $3 \times 10^{-20}/573$ | 127 |
| Ce _{0.5} Tb _{0.5} O _{1.8} | | $2 \times 10^{-20}/573$ | 127 |

^a Measurement temperature is indicated.

time at constant temperature^{502,503,506-508} or by obtaining the ¹⁸O depth profile on the solid after a pretreatment with isotopically labeled oxygen-containing molecules.⁵⁰⁹ All works share the common feature to consider that oxygen exchange with the solid occurs through a process with two well-differentiated rate constants: one ascribed to a “fast” process occurring at or near the surface region and a “slow” one characteristic of the bulk. In the adequate experimental conditions surface and bulk oxygen diffusion coefficients can be independently measured,^{500-503,506-508} but here it is pertinent to mention that the conceptual difference between bulk and surface is somewhat lost in nanostructured materials.

Surface diffusion coefficients are scarce in the open literature, but a series of measurements taken from refs 508 and 510 are displayed in Table 4. The interval reported for CeO₂ gives values corresponding to a sample calcined at different temperatures, 773–1173 K. This suggests that particle size has a profound impact on surface diffusion; the CeO₂ values range in more than 2 orders of magnitude interval while all metal oxides vary in five orders.^{508,510} Of course, as no detailed information on the surface impurities of the samples is known, this last factor may also contribute to the results. Some other works analyzed the surface contribution to the anion mobility as a function of the temperature.^{506,507} Measurements of the oxygen bulk diffusion coefficient^{127,418,508,510-512} are also displayed in Table 4. Again, a correlation with structural properties and, particularly, with average primary particle size is lacking and must be delayed until enough data become available. On the other hand, comparison of the bulk diffusion coefficient measured from isotopic exchange and electrical conductivity are routinely used to check whether the electrical conductivity is associated with anion or hole/electronic contributions.⁵⁰⁹

Impedance spectroscopy is a widely used technique for the study of electrical properties of materials.^{513,514} In this technique, an ac voltage ($V(\omega) = V_0 e^{i\omega t}$) is applied to the sample. The system will respond with the generation of an ac current of the same frequency but showing in general a phase shift ϕ ($I(\omega) = I_0 e^{i(\omega t + \phi)}$). The complex impedance is defined by Ohm's law as

$$Z(\omega) = V(\omega)/I(\omega) = Z_0 e^{-i\phi} = Z_0 \cos \phi - iZ_0 \sin \phi \quad (4.1.1.a)$$

Impedance spectra are collected as a function of the ac frequency ω and are usually presented in the form of Nyquist (or Cole–Cole) plots in which the imaginary part of the impedance is plotted versus the real part of the impedance. The impedance of a material can be assimilated to simple equivalent circuits consisting of resistors, capacitors, or inductances for which nonlinear least-squares-fit routines are used to extract the corresponding components.⁵¹³ In a general ideal case, a compacted polycrystalline solid (along with the contact measuring electrodes) is fitted with three RC circuits (resistance and capacitor in parallel) connected in series corresponding to contributions from the different structural elements of the complete circuit (grain bulk, grain boundaries, and electrodes); this appears in the Nyquist plot as three distinct semicircles at decreasing frequency, respectively, and allows one thus to separate bulk and interfacial contributions to the overall conductivity.⁵¹⁴ In a real case, discrimination between the different semicircles can be difficult when the characteristic frequencies do not differ strongly. This can occur most frequently in nanocrystalline materials in which bulk and interface contributions can appear as overlapping semicircles in the impedance plot as a consequence of the increased grain boundary contribution with respect to micro-sized particles.^{513,514}

On the other hand, discrimination between different possible charge carriers (electrons, holes, or ions) can be done by employing electrodes blocking the charge carriers selectively.⁵¹⁴ This is particularly useful in cases in which the electronic contribution largely dominates the conductivity as a consequence of the higher electron mobility, as it occurs for CeO_{2-x}.^{414,515,516} Thus, the use of a YSZ electronic blocking electrode (complete cell configuration Pt/CeO_{2-x}/YSZ/Pt) has allowed the independent study of the ionic conduction in nanocrystalline CeO_{2-x}.⁵¹⁶ Another possibility to analyze the nature of the charge carrier is to compare the results of impedance and tracer diffusion (or isotopic exchange, see above) measurements, which are connected through the Haven ratio H_R as

$$D^T = H_R D^f \quad (4.1.1.b)$$

where D^T is the tracer diffusion coefficient (or diffusivity) and D^V is the diffusion coefficient obtained from conductivity measurements (note that the diffusion coefficient and the conductivity are connected by the Nernst–Einstein equation $D^V = \sigma k_B T / N q^2$).⁵¹⁴ Thus, $H_R = 1$ in the special case that single ions are the only carriers and follow random (uncorrelated) hopping motion. $H_R < 1$ when correlations occur in the movement of charge carriers or when electronic conduction is present. $H_R > 1$ when defects such as vacancy pairs or impurity–vacancy associations which do not give rise to conductivity contributions (but participate in tracer exchange processes) are present. A further possibility, most useful in the case of oxygen conductor oxide materials, consists of the analysis of the oxygen partial pressure dependence of the conductivity. A clear example in this respect is provided by the n-type conductor CeO_{2-x} .^{414,514–516} While the electronic conductivity decreases with increasing $p\text{O}_2$ as a consequence of the associated decrease in the electron concentration, the ionic conduction is independent of $p\text{O}_2$.^{414,514–516}

Generally speaking, the analysis of electrical conduction properties of materials by impedance spectroscopy (or isotopic exchange-tracer methods) is strongly affected by the presence of (uncontrolled in some cases) impurities in the samples. Such impurities can show a trend to segregate to the surface of the samples (Si is a typical example) producing increased grain boundary resistance or can remain as ionic dopants in the samples bulk producing new ionic conduction paths.^{390,414,516} Nevertheless, some general conclusions can be pointed out concerning the electrical properties of nanostructured oxides, in particular from studies comparing nano- and micro-sized samples.^{345,390,516–518} Thus, in pure ceria it looks clear that the nanostructured sample shows increased electronic conductivity compared to micro-sized or monocrystalline samples on the basis of impedance spectroscopy analyses.^{414,513–516} The ionic conductivity could however be decreased in the nanosized sample.⁵¹⁶ Theoretical explanation for this behavior is based on the space charge model,^{511,519,520} proposing that the space charge potential results in depletion of oxygen vacancies and accumulation of conduction electrons.⁵¹⁵ The presence of electronic conduction is also observed for lightly doped nanosized $\text{Ce}_{0.985}\text{Gd}_{0.015}\text{O}_{2-x}$, which is normally an ionic conductor in the extended crystal form.⁵²⁰ No particular conductivity enhancement is however observed for ionically conducting nanosized $\text{Ce}_{0.74}\text{Gd}_{0.26}\text{O}_{1.87}$ in comparison with the coarse-grain sample.⁵²⁰ Enhanced electronic conductivity is also observed in the case of nanosized TiO_2 , while the nanosized ceramics show an uncommon domain of ionic conductivity at high oxygen pressure.^{345,519} In the case of YSZ, as mentioned before, an enhanced grain boundary conductivity is observed in the nanostructured sample.³⁹⁰

4.1.2. Photochemical Properties

Photochemical properties of metal oxides are mainly related to their use in electrochromic devices, photovoltaic cells, and as heterogeneous catalysts. Con-

trolling light transmission in windows or reflection in mirrors and displays constitutes an active field of research. Multitude of solid electrochromic devices based on metal oxides has been tested, but tungsten oxide (WO_3) seems the only stable enough under visible and UV excitation at the expense, however, of having a poor time and color intensity response.⁵²¹ The WO_3 properties depend on a series of factors among which the structural properties and presence of W^{5+} entities on the oxide network appear as capital.⁵²² The nanostructure has notable implications for this problem, but, up to now, no clear thermodynamic study of the nanophase stability as a function of size has been reported for W trioxide. Through the high surface/volume ratio characteristic of nanostructured materials, this latter property also influences the degree of color change attained by the solid by following the W oxidation state change under cycling reductive/oxidizing conditions.^{324,523}

The conversion of sunlight to electric power is dominated by solid-state junction devices mainly based on silicon but is currently being challenged by photovoltaic cells based on nanocrystalline TiO_2 and conducting polymer films.⁵²⁴ TiO_2 is, as mentioned in section 3.1, stable to photocorrosion, but its wide band gap does not allow it to absorb the visible region of the sunlight spectrum. To do it, the TiO_2 surface is in this case covered by a monolayer of a dye, which under excitation goes into an excited-state relaxing through the injection of the electron into the conduction band of TiO_2 . The backward reaction, e.g., electron–hole charge pair recombination, occurs at a much lower rate. The hole is, at the same time, transferred to a redox mediator present between the TiO_2 -containing electrode and the counter electrode. In the photovoltaic cell, operating voltage of the cell is given by the potential difference between the conduction band of TiO_2 and the redox potential (relative to an SCE electrode) of the redox mediator. The nanostructure of the semiconductor has important consequences in the photoelectrochemical properties of interest for photovoltaic cells. Comparing with a classical, bulklike TiO_2 electrode, the depletion layer cannot be formed and the photoresponse of the electrode is directly determined by the rates of reaction of the positive and negative charge carriers with the redox mediator couple. An additional positive effect arises from quantum confinement and the expected blue-shifted band gap energy; the lowering/increasing of the conduction/valence band allows reduction/oxidation reactions than cannot proceed on bulk semiconductor for thermodynamic reasons. Finally, the photocurrent conversion efficiency is very high and about 3–4 orders that of micro-sized systems.

Heterogeneous photocatalysis is mainly performed with TiO_2 -based systems due to its mentioned stability against photocorrosion and concerns the degradation of organic/inorganic pollutants^{315,525} or organic synthesis.³¹⁶ The anatase structure is considered by far the most efficient among TiO_2 polymorphs, although the physicochemical background of this fact is not well understood. The photocatalytic process involves the separation of the electron–hole charge

pair, their transport and trapping to/at the surface, and, finally, their reaction with the desired molecules. These processes always compete with the charge pair recombination. The nanostructure profoundly affects these elemental processes based on several reasons. Apart from a high surface-to-volume ratio, which must be beneficial for all chemical processes, the first factor is, as mentioned in the previous paragraph, the quantum confinement and improved reduction/oxidation power. The second is the practical absence of band bending and the consequent easier access of both charged particles to the surface. Connecting with the latter, some photocatalysts improve charge pair separation with contact between two different phases which physically can separate electrons and holes.⁵²⁶ A drawback of a limited size is that the charge pair recombination generally displays higher rates as it appears that a direct relationship can be established with the number of defective sites.⁵²⁷ Concerning photocatalysis, it can be also noted that the above-mentioned limitation of the TiO₂ wide band gap and limited use of sunlight spectrum is here resolved by using several techniques mainly based in the doping of the materials with heterocations^{355,528} or C and/or N.⁵²⁹ The use of visible light sensitizers containing sulfur^{530,531} present at the surface of anatase or ABO₄-type oxides^{532,533} has been also described to reach this goal.

4.2. Chemical Reactivity and Surface Properties

The chemical reactivity of the surface sites of an oxide nanoparticle is a very important issue for applications in catalysis, and the control of environmental pollution, electrochemistry, fuel cells, sensor devices, etc.¹⁻³ A goal in the emerging field of nanotechnology is to make nanostructures or nanoarrays with a very large surface area.^{15,16,441} In an oxide nanoparticle, the ratio of surface atoms to nonsurface atoms is usually much larger than in a bulk material and surface species display local geometry differing from the bulk and strongly influencing chemical reactivity.⁵² The adsorption of molecules or atoms on the surface of a nanoparticle can be studied using many of the experimental techniques described in section 2 (XANES/EXAFS, STM/AFM, Raman, optical spectroscopy, valence, and core-level photoemission) and other techniques not covered like infrared spectroscopy, EPR, or NMR.^{1-3,534} The combination of these techniques provides information about adsorption sites, adsorbate bonding characteristics, local order, coverage effects, coadsorption effects, and surface reactions.^{1-3,52,534} Particular attention has received the use of CO,⁵³⁴⁻⁵³⁶ NO,^{534,536,537} methanol,^{127,538,539} and other (pyridine, ammonia, etc.)^{534-536,540} probe molecules coupled with infrared detection and, in a parallel way, with thermal desorption techniques, to characterize the nature, acid/basic, and general redox properties of oxide surfaces. The use of sum-frequency generation, which is intrinsically surface sensitive, will be able to extend the power of the infrared technique, particularly to frequency regions (below 1000 cm⁻¹) where the absorption of the oxide solid does not allow obtaining information by using conventional techniques.⁵⁴¹ Acid/basic prop-

erties are also investigated in oxides⁵⁴² and zeotypes and zeolites⁵⁴³ by using ¹H, ¹³C NMR. The use of O₂ as a probe molecule and the important effect of surface vacancies is mainly followed by using EPR detection.^{544,545} On the other hand, theoretical studies are useful for the interpretation of experimental outcomes with probe molecules and, in many cases, can predict chemical behavior of surface species.^{37,46}

In principle, several factors can make the chemical activity of an oxide nanoparticle unique.^{16,23,26,546} Nanostructures of metal compounds can adopt geometries not seen in the bulk state. Also there could be important variations in the oxygen/metal ratio. O vacancies not common in the bulk state could be present in the nanoparticle enhancing its reactivity. In the other extreme, a nanoparticle could have an oxygen/metal ratio larger than observed for bulk oxides of a given metal. This could lead to perturbations in the chemical activity as a result of ligand effects (bigger positive charge on the metal cations, smaller negative charge on the oxygen anions) or ensemble effects (variation in the relative number of cation and anion centers exposed in the surface). From an electronic viewpoint, perturbations in the chemical activity can arise from changes in the size of the band gap^{46,48,232} or from a redistribution of atomic charges^{40,53} when going from large periodic structures to small nanostructures. An important factor to consider when dealing with the chemical properties of a bulk oxide surface are the long-range effects of the Madelung field, which are not present or limited in an oxide nanoparticle.³⁷⁻³⁹ In nanoparticles of pure metals, the existence of corner or edge sites usually implies high reactivity.⁵⁴⁷⁻⁵⁵⁰ The situation can be more complex in an oxide nanoparticle due to the presence of voluminous Oxygen centers. Even when metal cations are at edge or corner sites, lacking a full sphere of coordination, the nearby oxygens can make difficult interactions with big molecules by steric repulsion.⁵⁵¹

Probably, the most complete study of chemisorption properties in nanosized materials is dealing with MgO-based systems. Experimental and theoretical studies have been performed that allow one to compare the chemical reactivity and surface properties of MgO nanoparticles, MgO bulk powders, and extended MgO(100) surfaces.^{38,41,42,45,52,53,459,552} Films of MgO nanostructures can have a surface area much larger than that of bulk powders of the material.^{52,441,459} They are also rich in defect sites that are more reactive than the atoms in the highly stable (100) face of crystalline MgO.^{52,451} Figure 15 compares CO desorption temperatures from a series of MgO (top panel) and Mg_{1-x}Cr_xO₂ (bottom panel) systems.⁵⁵² Thermal desorption spectra for CO on a MgO(100) single-crystal surface cleaved in a vacuum exhibit a peak at ~60 K.⁵⁵³ The adsorption energy on flat terraces of MgO is ~3.2 kcal/mol.⁵⁵³ On defects or imperfections of MgO(100), the desorption temperature of CO can increase to ~120 K.^{451,554} Cubic nanoparticles of MgO with a size larger than 150 nm (bulklike systems) have a CO desorption temperature of ~135 K, while a CO desorption temperature of

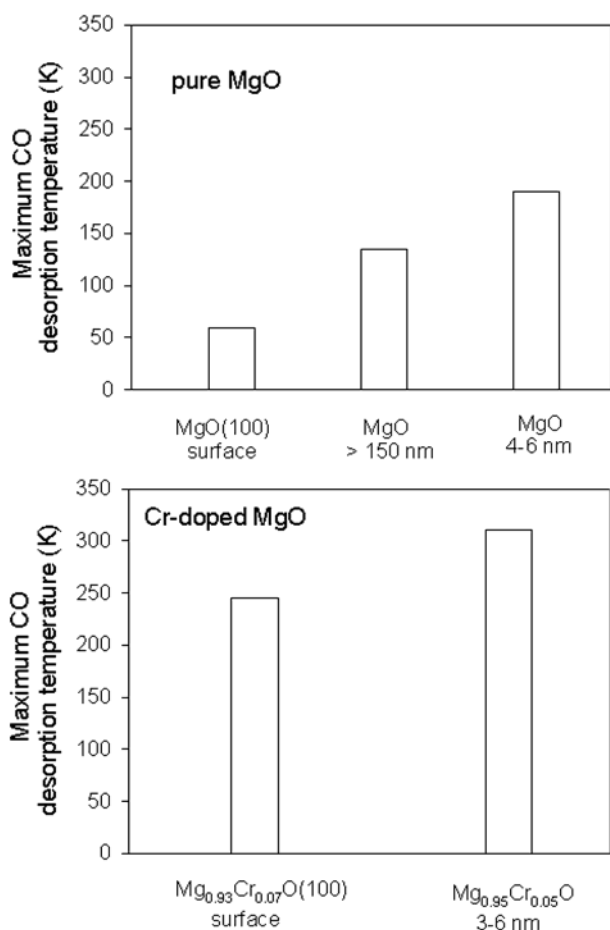


Figure 15. Maximum CO desorption temperatures for nanoparticles and extended surfaces of pure MgO (top) and $\text{Mg}_{1-x}\text{Cr}_x\text{O}_2$ (bottom). Data taken from refs 451, 552, and 553.

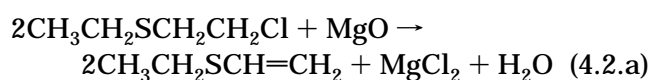
~190 K is seen for MgO nanoparticles in the range of 4–6 nm.⁵⁵² This last temperature implies an increase of ~5 kcal/mol with respect to the CO adsorption energy on a perfect MgO(100) surface. In the top panel of Figure 15, the reactivity of the oxide systems increases following the sequence: MgO(100) surface < bulklike MgO particles < MgO nanoparticles. An identical trend is found when comparing the corresponding NO desorption temperatures.⁵⁵² In the MgO nanoparticles, one can expect a substantial percentage of Mg cations that have only four or three oxygen neighbors.⁵⁴² Theoretical studies have shown that these sites interact better with CO and NO than the pentacoordinated Mg cations present in a perfect MgO(100) surface.^{38,443,444,555}

The bottom panel in Figure 15 displays CO desorption temperatures from a $\text{Mg}_{0.93}\text{Cr}_{0.07}\text{O}$ (100) surface⁴⁵¹ and $\text{Mg}_{0.95}\text{Cr}_{0.05}\text{O}$ nanoparticles (3–6 nm in size).⁵⁵⁰ The Cr-doped MgO systems adsorb CO stronger than pure MgO. Doping with Cr introduces occupied electronic states above the valence band of MgO (see Figure 14, section 3.4) which are very efficient for bonding interactions with CO.⁴⁵¹ The adsorption energies of CO are ~15 and 19 kcal/mol on the $\text{Mg}_{0.93}\text{Cr}_{0.07}\text{O}$ (100) surface and $\text{Mg}_{0.95}\text{Cr}_{0.05}\text{O}$ nanoparticles, respectively.^{451,552} Again, the nanoparticles bond CO better than the surface of the bulk oxide, probably due to the presence of corner or edge sites.⁵⁵²

For the case of water adsorbed on MgO(100), several experimental techniques show no evidence for hydroxylation of this surface.^{556–558} Periodic Hartree–Fock calculations indicate that the dissociation of the adsorbed H_2O is a highly endothermic process.⁴⁵ A significant amount of defect sites or imperfections is necessary to induce the cleavage of O–H bonds and the hydroxylation of MgO(100).^{45,559} Water adsorbs and dissociates readily on small nanoparticles of MgO.^{440,459,560} The interaction of one and two H_2O molecules with three-coordinated sites of Mg_4O_4 and Mg_8O_8 clusters has been investigated using post Hartree–Fock calculations (Møller–Plesset second-order perturbation theory).⁵³ The results indicate that water chemidissociates without a barrier onto the adjacent three-coordinate sites of the nanoparticles. The chemidissociation energy per water molecule is observed to be greater upon the dissociation of two neighboring H_2O molecules compared to the dissociation of a single water molecule: a positive cooperative effect.⁵³

The adsorption of SO_2 on nanoparticles of MgO at 300 K mainly produces SO_4 groups, $\text{SO}_2(\text{gas}) + 2\text{O}(\text{oxide}) \rightarrow \text{SO}_4(\text{adsorbed})$, with a very small amount of SO_3 and without cleavage of S–O bonds (i.e., no deposition of atomic sulfur on the Mg cations).⁵⁵² In contrast, the adsorption of SO_2 on a MgO(100) crystal under similar conditions mainly yields SO_3 with SO_4 as a secondary product.⁴⁶⁰ Calculations based on the Hartree–Fock method and DFT indicate that the formation of SO_4 on MgO(100) is not spontaneous and requires a major reconstruction of the surface with the participation of defect sites.^{454,461,561} In the calculations, the interaction of SO_2 with MgO(100) produces a SO_3 -like species.^{454,553} For SO_2 on the MgO nanoparticles, the existence of corner and edge sites in the oxide substrate facilitates the structural changes necessary for the formation of SO_4 .⁵⁶² The doping of the MgO nanoparticles with Cr produces a system that is extremely efficient for the destruction of SO_2 .⁴⁴⁹ The $\text{Mg}_{1-x}\text{Cr}_x\text{O}_2$ nanoparticles are able to cleave the S–O bonds at temperatures below 300 K, while bulk MgO and Cr_2O_3 only adsorb the molecule to form SO_3 or SO_4 species.^{449,552} The Cr atoms in the $\text{Mg}_{1-x}\text{Cr}_x\text{O}_2$ nanoparticles are trapped in a “+2” formal oxidation state and have occupied electronic states that appear well above the MgO valence band (see Figure 14, section 3.4). These properties facilitate interactions with the LUMO of SO_2 and make the nanoparticles more chemically active than bulk MgO or Cr_2O_3 .^{449,562}

Nanoparticles of MgO, CaO, Al_2O_3 , CuO, NiO, and ZnO with sizes in the range of 4–7 nm exhibit unparallel destructive adsorption properties for acid gases, polar organics, and even chemical/biological warfare agents.^{52,459,460} For example, bulk MgO is not useful for removing chlorine from chloroethylethyl sulfide (a mimic of mustard gas), whereas nanocrystals of MgO are highly reactive:⁴⁵⁹



These nanoparticles were prepared by specially designed sol-gel or aerogel processes.⁴⁵⁹ Depending on the exact procedure followed for the preparation, nanoparticles of MgO and CaO with polyhedral or hexagonal shapes can be prepared, but they also contain OH groups. In these morphological shapes, the nanoparticles possess more defects than expected for the typical cubic shape of MgO and CaO.^{52,458,459} Such defects could be of the Frenkel- or Schottky-type (vacancies), or be manifested as unusual configurations of edges, corners, or crystal planes.⁴⁵⁹ Adsorption data for AlEt₃, CO₂, SO₂, HCl, CCl₄, and other molecules are conclusive that the polyhedral or hexagonal nanocrystals of MgO and CaO are more reactive than cubic microcrystals of these oxides.⁵² This has been mainly attributed to morphological differences, including the concentration of defects. However, intrinsic electronic effects due purely to “smallness” (confinement) could not be ruled out.⁵² The surface properties of nanostructured materials have been also tuned by using the egg-shell methodology.^{563–565}

One method frequently employed for the preparation of active oxide catalysts involves partial reduction under hydrogen at elevated temperatures.^{2,566} For bulk oxides, this process is usually associated with an induction time.^{567,568} During the induction time, defect sites are probably created that eventually accelerate the rate of H₂ dissociation.^{566,567} A priori, the edge and corner sites in oxide nanoparticles should favor the dissociation of H₂ leading to small induction times during the reduction process. Indeed, recent experimental and theoretical results indicate that it is much easier to reduce small particles of NiO (size < 5 nm) than bulklike powders of the material or the NiO(100) surface.^{558,559} The same trend is found when comparing the reduction rates of CeO₂ nanoparticles and bulk CeO₂.⁷⁶ In the case of ceria, doping with elements such as Zr or Ca accelerates the reduction process by introducing strain in the lattice of the nanoparticles.^{76,413}

Nanoparticles of pure or metal-doped MgO, TiO₂, Fe₂O₃, NiO, CuO, ZrO₂, and CeO₂ can be very useful as catalysts for the control of environmental pollution and the conversion of hydrocarbons.^{7,8,52,138,145,417,418,420,429,458,569} In general, the high catalytic activity of these oxide systems is a consequence of combining a very high surface area and a large number of active sites that are not common in the surfaces of the corresponding bulk oxides.

5. Concluding Remarks and Future Work

The studies described in the previous sections show oxide systems that have unique properties with a tremendous potential for technological applications. In recent years, the progress made in the development of methods and techniques for the preparation, and characterization of oxide nanostructures has been very impressive, but clearly much more research is necessary to produce the type of knowledge and understanding necessary for a rational design of these systems.

“Size effects” have not been studied for many oxides in a systematic way. For a vast number of oxide

compounds, this comes from the fact that the preparation procedures are not able to give a size distribution approaching the delta function; this contrasts with the significant degree of control reached for other materials of technological interest as metals or chalcogenides. Although a tremendous progress has been reached in the past decades, particularly with the use of chemical-like methods for obtaining mixed oxides, the “fine-tuning” of the number of atoms in an oxide nanoparticle is still a challenge. A particular problem when dealing with studies of nanostructured oxides as a function of size is the presence of amorphous material together with the crystalline phase and, typically, in growing quantities as low as the primary particle size. This and other factors are dependent on the preparation method and a better control of experimental variables is needed to gain further insight into the effects of nanostructure on oxides.

Better and faster techniques for structural and electronic characterization have to be devised. One must be able to monitor and follow the behavior of oxide nanostructures when their surrounding chemical environment rapidly changes as a function of time. A real challenge is the characterization of oxide nanoparticles in-situ under the harsh conditions employed in many industrial chemical processes. Single-particle characterization techniques may be the only valuable option when dealing with nanosystems that have a wide distribution of sizes and shapes.

At a conceptual level, we need a better understanding of the subtle links among size, shape, and structure, and how these properties affect the electronic and chemical behavior of oxide nanoparticles. For many applications, a conceptual framework must be established to predict and control the performance of oxide nanoparticles. This can only be achieved through a close coupling of experiment with theory. In this sense, the use of new DFT exact-exchange methods and the use of time-dependent theoretical analysis of experimental observables would definitively contribute to the understanding of oxide properties and the influence of size.

6. Acknowledgment

J.H. and J.A.R. are grateful for the financial support of the US Department of Energy, Division of Chemical Sciences (DE-AC02-98CH10886 contract). M.F.G. and A.M.A. thank the Spanish “Ministerio de Ciencia y Tecnología” and CSIC for financial support.

7. References

- (1) Noguera, C. *Physics and Chemistry at Oxide Surfaces*; Cambridge University Press: Cambridge, UK, 1996.
- (2) Kung, H. H. *Transition Metal Oxides: Surface Chemistry and Catalysis*; Elsevier: Amsterdam, 1989.
- (3) Henrich, V. E.; Cox, P. A. *The Surface Chemistry of Metal Oxides*; Cambridge University Press: Cambridge, UK, 1994.
- (4) Wells, A. F. *Structural Inorganic Chemistry*, 6th ed.; Oxford University Press: New York, 1987.
- (5) Harrison, W. A. *Electronic Structure and the Properties of Solids*; Dover: New York, 1989.
- (6) Wyckoff, R. W. G. *Crystal Structures*, 2nd ed.; Wiley: New York, 1964.

- (7) *Handbook of Heterogeneous Catalysis*; Ertl, G.; Knozinger, H.; Weitkamp, J., Ed.; Wiley-VHC: Weinheim, 1997.
- (8) Shelef, M.; Graham, G. W.; McCabe, R. W. In *Catalysis by Ceria and Related Materials*; Trovarelli, A., Ed.; Imperial College Press: London, 2002; Chapter 10.
- (9) Stirling, D. *The Sulfur Problem: Cleaning Up Industrial Feedstocks*; Royal Society of Chemistry: Cambridge, 2000.
- (10) Sherman, A. *Chemical Vapor Deposition for Microelectronics: Principles, Technology and Applications*; Noyes publications: Park Ridge, NJ, 1987.
- (11) Gleiter, H. *Nanostructured Mater.* **1995**, *6*, 3.
- (12) Valden, M.; Lai, X.; Goodman, D. W. *Science* **1998**, *281*, 1647.
- (13) Rodriguez, J. A.; Liu, G.; Jirsak, T.; Hrbek, Chang, Z.; Dvorak, J.; Maiti, A. *J. Am. Chem. Soc.* **2002**, *124*, 5247.
- (14) Baumer, M.; Freund, H.-J. *Prog. Surf. Sci.* **1999**, *61*, 127.
- (15) Trudeau, M. L.; Ying, J. Y. *Nanostructured Mater.* **1996**, *7*, 245.
- (16) *Nanomaterials: Synthesis, Properties and Applications*; Edelstein, A. S.; Cammarata, R. C., Eds.; Institute of Physics Publishing: London, 1998.
- (17) Khaleel, A.; Richards, R. M. in *Nanoscale Materials in Chemistry*; Kladunde, K. J., Ed.; Wiley: New York, 2001, Chapter 4.
- (18) Ayyub, P.; Palkar, V. R.; Chattopadhyay, S.; Multani, M. *Phys. Rev. B* **1995**, *51*, 6135.
- (19) (a) Millot, N.; Aymes, D.; Bernard, F.; Niepce, J. C.; Traverse, A.; Bourée, F.; Cheng, B. L.; Perriat, P. *J. Phys. Chem. B*, **2003**, *107*, 5740. (b) Schoiswohl, J.; Kresse, G.; Surnev, S.; Sock, M.; Ramsey, M. G.; Netzer, F. P. *Phys. Rev. Lett.* **2004**, *92*, 206103.
- (20) McHale, J. M.; Auroux, A.; Perrota, A. J.; Navrotsky, A. *Science* **1997**, *277*, 788.
- (21) Zhang, H.; Bandfield, J. F. *J. Mater. Chem.* **1998**, *8*, 2073.
- (22) Samsonov, V. M.; Sdobnyakov, N. Yu.; Bazulev, A. N. *Surf. Sci.* **2003**, *532–535*, 526.
- (23) Song, Z.; Cai, T.; Chang, Z.; Liu, G.; Rodriguez, J. A.; Hrbek, J. *J. Am. Chem. Soc.* **2003**, *125*, 8060.
- (24) Mezey, L. Z.; Gibeil, J. *J. Appl. Phys.* **1982**, *21*, 1569.
- (25) Liu, P.; Rodriguez, J. A.; Muckerman, J. T.; Hrbek, J. *Phys. Rev. B*, **2003**, *67*, 155416.
- (26) Rodriguez, J. A.; Rodriguez, L.; Ruetter, F.; Gonzalez, L., manuscript in preparation.
- (27) Ayyub, P.; Multani, M.; Barma, M.; Palkar, V. R.; Vijayaraghavan, R. *J. Phys. C: Solid State Phys.* **1988**, *21*, 229.
- (28) Garvie, R. C.; Goss, M. F. *J. Mater. Sci.* **1986**, *21*, 1253.
- (29) Hernández-Alonso, M. D.; Hungria, A. B.; Coronado, J. M.; Martínez-Arias, A.; Conesa, J. C.; Soria, J.; Fernández-García, M. *Phys. Chem. Chem. Phys.* **2004**, *6*, 3524.
- (30) Skandan, G.; et al. *Nanostructured Mater.* **1992**, *1*, 313.
- (31) Cammarata, R. C.; Sieradski, K. *Phys. Rev. Lett.* **1989**, *62*, 2005.
- (32) Wang, X.; Hanson, J.; Rodriguez, J. A.; Iglesias-Juez, A.; Fernandez-Garcia, M. *J. Chem. Phys.*, (in press, DOI: 10.1063/1.1781116).
- (33) Surnev, S.; Kresse, G.; Ramsey, M. G.; Netzer, F. P. *Phys. Rev. Lett.* **2001**, *87*, 86102.
- (34) Moriarty, P. *Rep. Prog. Phys.* **2001**, *64*, 297.
- (35) Yoffe, A. D. *Adv. Phys.* **1993**, *42*, 173.
- (36) Brus, L. *J. Phys. Chem.* **1986**, *90*, 2555.
- (37) Pacchioni, G.; Ferrari, A. M.; Bagus, P. S. *Surf. Sci.* **1996**, *350*, 159.
- (38) Mejias, J. A.; Marquez, A. M.; Fernandez-Sanz, J.; Fernandez-Garcia, M.; Ricart, J. M.; Sousa, C.; Illas, F. *Surf. Sci.* **1995**, *327*, 59.
- (39) Fernández-García, M.; Conesa, J. C.; Illas, F. *Surf. Sci.* **1996**, *349*, 207.
- (40) Albaret, T.; Finocchi, F.; Noguera, C. *Faraday Discuss.* **2000**, *114*, 285.
- (41) Rodriguez, J. A.; Maiti, A. *J. Phys. Chem. B*, **2000**, *104*, 3630.
- (42) Rodriguez, J. A.; Jirsak, T.; Chaturvedi, S. *J. Chem. Phys.* **1999**, *111*, 8077.
- (43) Bredow, T.; Apra, E.; Catti, M.; Pacchioni, G. *Surf. Sci.* **1998**, *418*, 150.
- (44) Casarin, M.; Maccato, C.; Vittadini, A. *Surf. Sci.* **1997**, *377–379*, 587.
- (45) Scamehorn, C. A.; Harrison, N. M.; McCarthy, M. I. *J. Chem. Phys.* **1994**, *101*, 1547.
- (46) Rodriguez, J. A. *Theor. Chem. Acc.* **2002**, *107*, 117.
- (47) Rodriguez, J. A.; Chaturvedi, S.; Kuhn, M.; Hrbek, J. *J. Phys. Chem. B*, **1998**, *102*, 5511.
- (48) Hoffmann, R. *Solids and Surfaces: A Chemist's View of Bonding in Extended Structures*; VCH: New York, 1988.
- (49) Albright, T. A.; Burdett, J. K.; Whangbo, M. H. *Orbital Interactions in Chemistry*; Wiley-Interscience: New York, 1985.
- (50) Luth, H.; *Surface and Interface of Solid Materials*; Springer, Berlin, 1997.
- (51) Bardeen, J. *Phys. Rev.* **1947**, *71*, 717.
- (52) Lucas, E.; Decker, S.; Khaleel, A.; Seitz, A.; Futlz, S.; Ponce, A.; Li, W.; Carnes, C.; Klabunde, K. *J. Chem. Eur. J.* **2001**, *7*, 2505.
- (53) Anshell, J. L.; Hess, A. C. *J. Phys. Chem.* **1996**, *100*, 18317.
- (54) Rodriguez, J. A.; Hrbek, J.; Dvorak, J.; Jirsak, T.; Maiti, A. *Chem. Phys. Lett.* **2001**, *336*, 377.
- (55) Ferrari, A. M.; Pacchioni, G. *J. Phys. Chem.* **1995**, *99*, 17010.
- (56) Richards, R.; Li, W.; Decker, S.; Davidson, C.; Koper, O.; Zaikovski, V.; Volodin, A.; Rieker, T. *J. Am. Chem. Soc.* **2000**, *122*, 4921.
- (57) Diéguez, A.; Romano-Rodríguez, A.; Vilá, A.; Morante, J. R. *J. Appl. Phys.* **2001**, *90*, 1550.
- (58) Rush, G. E.; Chadwick, A. V.; Kosacki, I.; Anderson, H. U. *J. Phys. Chem. B* **2000**, *104*, 9597.
- (59) Xijuan, Y.; Pingbo, X.; Qingde, S. *Phys. Chem. Chem. Phys.* **2001**, *3*, 5266.
- (60) Stout, G.; Jensen, L. *X-ray Structure Determination A Practical Guide*; John Wiley & Sons: New York, 1989.
- (61) *Defect and Microstructure Analysis by Diffraction*; Snyder, R. L.; Fiala, J.; Bunge, H. J., Eds.; Oxford University Press: New York, 1999.
- (62) Egami, T.; Billinge, S. J. L. *Underneath the Bragg Peaks Structural Analysis of Complex Materials*; Elsevier: Oxford, 2003; Vol. 7.
- (63) (a) Guinier, A. *X-ray Diffraction in Crystals, Imperfect Crystals and Amorphous Bodies*; Dover: Mineola, NY, 1994. (b) Deb, B.; Biswas, T.; Sen, D.; Basumallick, A.; Mazumder, S. *J. Nanoparticle Res.* **2002**, *4*, 91. (c) Ohnuma, M.; Hono, K.; Onodera, H.; Ohnuma, S.; Fujimori, H.; Pedersen, J. *J. Appl. Phys.* **2000**, *87*, 817.
- (64) Jenkins, R.; Snyder, R. L. *Introduction to X-ray Powder Diffraction*; John Wiley & Sons: New York, 1996.
- (65) Azaroff, L. V. *Introduction to Solids*; McGraw-Hill: New York, 1960.
- (66) Kim, J. Y.; Rodriguez, J. A.; Hanson, J. C.; Frenkel, A. I.; Lee, P. L. *J. Am. Chem. Soc.* **2003**, *125*, 10684.
- (67) Warren, B. *X-ray Scattering*; Dover: Mineola, NY, 1990.
- (68) Toby, B. H.; Egami, T. *Acta Crystallogr.* **1992**, *A48*, 336.
- (69) Proffen, T.; Billinge, S. J. L. *J. Appl. Crystallogr.* **1999**, *32*, 572.
- (70) Mamontov, E.; Egami, T. *J. Phys. Chem. Solids* **2000**, *61*, 1345.
- (71) Chupas, P. A.; Hanson, J. C.; Lee, P. L.; Rodriguez, J. A.; Iglesias-Juez, A.; Fernandez-Garcia, M., in preparation.
- (72) Mamontov, E.; Brezny, R.; Koranne, M.; Egami, T. *J. Phys. Chem. B* **2003**, *107*, 13007.
- (73) Norby, P.; Hanson, J. *Catal. Today* **1998**, *39*, 301.
- (74) Grunwaldt, J.-D.; Clausen, B. S. *Top. Catal.* **2002**, *18*, 37.
- (75) Walton, R. I.; O'Hare, D. *Chem. Commun.* **2000**, 2283.
- (76) Rodriguez, J. A.; Hanson, J. C.; Kim, J.-Y.; Liu, G.; Iglesias-Juez, A.; Fernandez-Garcia, M. *J. Phys. Chem. B* **2003**, *107*, 3535.
- (77) Chupas, P. J.; Qiu, X.; Hanson, J. C.; Lee, P. L.; Grey, C. P.; Billinge, S. J. L. *J. Appl. Cryst.* **2003**, *36*, 1342.
- (78) Fuggle, J. C.; Inglesfield, J. E. *Unoccupied Electronic States*; Springer-Verlag: Berlin, 1992.
- (79) See *X-ray Absorption*; Koningsberger, D. C., Prins, R., Eds.; Wiley: New York, 1987.
- (80) See articles in *Chem. Rev.* **2001**, *101*.
- (81) Rehr, J. J.; Albers, J. C. *Rev. Mod. Phys.* **2000**, *72*, 621.
- (82) Egelhoff, W. G. *Surf. Sci. Rep.* **1987**, *6*, 253.
- (83) Lytle, F. W. *Synchrotron Rad.* **1999**, *6*, 123.
- (84) Levine, I. N. *Molecular Spectroscopy*; Wiley: New York, 1975.
- (85) Aberg, T. *Phys. Rev.* **1967**, *16*, 14201.
- (86) Muller, J. E.; Jepen, O.; Andersen, O. K.; Wilkins, J. W. *Phys. Rev. Lett.* **1978**, *40*, 720.
- (87) Natoli, C. R.; Benfatto, M.; Doniach, S. *Phys. Rev. B* **1986**, *34*, 4682.
- (88) Rehr, J. J.; Albers, R. C. *Phys. Rev. B* **1996**, *41*, 8139.
- (89) Sayers, D. E.; Stern, E. A.; Lytle, F. W. *Phys. Rev. Lett.* **1971**, *21*, 1204.
- (90) Poiarkova, A. V.; Rehr, J. J. *Phys. Rev. B* **1999**, *59*, 948.
- (91) Bunker, G. *Nucl. Instrum. Methods Phys. Res.* **1983**, *207*, 437.
- (92) Chen, L. X.; Rajh, T.; Wang, Z.; Thurnauer, M. C. *J. Phys. Chem. B* **1997**, *101*, 10688.
- (93) Yeung, K. L.; Maira, A. J.; Stolz, J.; Hung, E.; Hu, N. K.-C.; Wei, A. C.; Soria, J.; Chao, K.-J. *J. Phys. Chem. B* **2002**, *106*, 4608.
- (94) Luca, V.; Djajanti, S.; Howe, R. F. *J. Phys. Chem. B* **1998**, *102*, 10650.
- (95) Winterer, M.; Nitsche, R.; Hahn, H. *Nanostructured Mater.* **1997**, *9*, 397.
- (96) Nachimuthu, P.; Shih, W.-C.; Liu, R.-S.; Jang, L.-Y.; Chem, J.-M.; *J. Solid State Chem.* **2000**, *149*, 408.
- (97) Zhu, Z.; Zhang, X.; Benfield, R. E.; Ding, Y.; Gandjean, D.; Zhang, Z.; Xu, X. *J. Phys. Chem. B* **2002**, *106*, 4569.
- (98) Nagai, Y.; Yamamoto, T.; Tanaka, T.; Yoshida, S.; Nonaka, T.; Okamoto, T.; Suda, A.; Sugura, M. *Catal. Today* **2002**, *74*, 225.
- (99) Lemaux, S.; Bansaddik, A.; van der Eerden, A. M. J.; Bitter, J. H.; Koningsberger, D. C. *J. Phys. Chem. B* **2001**, *105*, 4810.
- (100) Oshitake, H.; Suguhara, T.; Tatsumi, T. *Phys. Chem. Chem. Phys.* **2003**, *5*, 767.
- (101) Rockenberger, J.; Troger, L.; Kornowski, A.; Vossmeier, T.; Eychmuller, A.; Feldhaus, J.; Weller, H. *J. Phys. Chem. B* **1997**, *101*, 2691.
- (102) Clausen, B. S.; Norskov, J. K. *Topics Catal.* **2000**, *10*, 221.
- (103) Jentys, A. *Phys. Chem. Chem. Phys.* **1999**, *1*, 4059 and references therein.

- (104) Yang, P.; Cai, X.; Xie, X.; Xie, Y.; Hu, T.; Zhang, J.; Liu, T. *J. Phys. Chem. B* **2003**, *107*, 6511.
- (105) Asuka, K.; Iwasawa, Y. in *X-ray Absorption Fine Structure for Catalysts and Surfaces*; Iwasawa, Y., Ed.; World Scientific: Singapore, 1996; Chapter 7.
- (106) Fernández-García, M. *Catal. Rev. Sci. Eng.* **2002**, *44*, 59.
- (107) Kizler, P. *Phys. Lett. A* **1992**, *172*, 66.
- (108) Loudon, R. *Adv. Phys.* **2001**, *50*, 813.
- (109) See, for instance, Ferraro, J. R.; Nakamoto, K.; *Introductory Raman Spectroscopy*; Academic Press: New York, 1994.
- (110) Wachs, I. E. in *Handbook of Raman Spectroscopy*; Lewis, I. R., Edwards, H. G. M., Eds.; Marcel Dekker: New York, 2001; p 799.
- (111) Richter, H.; Wang, Z. P.; Ley, L. *Solid State Commun.* **1981**, *39*, 625.
- (112) Parayantal, P.; Pollak, F. H. *Phys. Rev. Lett.* **1984**, *52*, 1822.
- (113) Campbell, I. H.; Fauchet, P. M. *Solid State Commun.* **1986**, *58*, 739.
- (114) Spanier, J. E.; Robinson, R. D.; Zhang, F.; Chan, S.; Herman, I. P. *Phys. Rev. B* **2001**, *64*, 245407.
- (115) Kelly, S.; Pollak, F. H.; Tomkiewicz, M. *J. Phys. Chem. B* **1997**, *101*, 2730.
- (116) Fangxin, L.; Jinlong, Y.; Tianpeng, Z. *Phys. Rev. B* **1997**, *55*, 8847.
- (117) Rajalakshmi, M.; Arora, A. K.; Bendre, B. S.; Mahamuni, S. *J. Appl. Phys.* **2000**, *87*, 2445.
- (118) Zhang, W. F.; He, Y. L.; Zhang, M. S.; Yin, Z.; Chen, Q. *J. Phys. D: Appl. Phys.* **2000**, *33*, 912.
- (119) Bersani, D.; Lottici, P. P.; Ding, X. *Appl. Phys. Lett.* **1998**, *72*, 73.
- (120) Xu, J. F.; Ji, W.; Shen, Z. X.; Li, W. S.; Tang, S. H.; Ye, X. R.; Jia, D. Z.; Xin, X. Q. *J. Raman Spectrosc.* **1999**, *30*, 413.
- (121) Zuo, J.; Xu, C.; Hou, B.; Wang, C.; Xie, Y.; Qian, Y. *J. Raman Spectrosc.* **1996**, *27*, 921.
- (122) Zuo, J.; Xu, C.; Liu, Y.; Qian, Y. *Nanostructured Mater.* **1998**, *10*, 1331.
- (123) Kim, Y. K.; Jang, H. M. *Solid State Commun.* **2003**, *127*, 433.
- (124) Zhen, Z.; Tan, S.; Zhang, S.; Wang, J.; Jin, S.; Zhang, Y.; Sekine, H. *Jpn. J. Appl. Phys.* **2000**, *39*, 6293.
- (125) Tsunekawa, S.; Ishikawa, K.; Li, Z.-Q.; Kawazoe, Y.; Kasuya, A. *Phys. Rev. Lett.* **2000**, *85*, 3440.
- (126) McBride, J. R.; Hass, K. C.; Poindexter, B. D.; Weber, W. H. *J. Appl. Phys.* **1994**, *76*, 2435.
- (127) Hungria, A. B.; Martínez-Arias, A.; Fernández-García, M.; Iglesias-Juez, A.; Guerrero-Ruiz, A.; Calvino, J. J.; Conesa, J. C.; Soria, J. *Chem. Mater.* **2003**, *15*, 4309.
- (128) Weber, W. H.; Hass, K. C.; McBride, J. R. *Phys. Rev. B* **1993**, *48*, 178.
- (129) Siu, G. G.; Stokes, M. J.; Liu, Y. *Phys. Rev. B* **1999**, *59*, 3173.
- (130) Diéguez, A.; Romano-Rodríguez, A.; Morante, J. R.; Bårsan, N.; Weimar, U.; Göpel, W. *Appl. Phys. Lett.* **1997**, *71*, 1957.
- (131) Jouanne, M.; Morhange, J. F.; Kanehisa, M. A.; Haro-Poniatowski, E.; Fuentes, G. A.; Torres, E.; Hernández-Tellez, E. *Phys. Rev. B* **2001**, *64*, 155404.
- (132) Hinrichs, K.; Schierhorn, A.; Haier, P.; Esser, N.; Richter, W.; Sahn, J. *Phys. Rev. Lett.* **1997**, *79*, 1094.
- (133) Glinka, Y. D.; Jaroniec, M. *J. Phys. Chem. B* **1997**, *101*, 8832.
- (134) Glinka, Y. D.; Jaroniec, M. *J. Appl. Phys.* **1997**, *82*, 3499.
- (135) Williams, D. B.; Carter, C. B. *Transmission Electron Microscopy*; Plenum Press: New York, 1996.
- (136) Reimer, L. *Transmission Electron Microscopy*, 4th ed.; Springer Series in Optical Sciences; Berlin, 1997; Vol. 36.
- (137) Spence, J. C. H. *Mater. Sci. Eng. R* **1999**, *26*, 1.
- (138) Yacamán, M. J.; Díaz, G.; Gómez, A. *Catal. Today* **1995**, *23*, 161.
- (139) Wang, Z. L. *J. Phys. Chem. B* **2000**, *104*, 1153.
- (140) Thomas, J. M.; Terasaki, O.; Gai, P. L.; Zhou, W. Z.; Gonzalez-Calbet, J. *Acc. Chem. Res.* **2001**, *34*, 583.
- (141) Bernal, S.; Baker, R. T.; Burrows, A.; Calvino, J. J.; Kiely, C. J.; López-Cartes, C.; Pérez-Omil, J. A.; Rodríguez-Izquierdo, J. M. *Surf. Interface Anal.* **2000**, *29*, 411.
- (142) Yacamán, M. J.; Ascencio, J. A.; Liu, H. B.; Gardea-Torresdey, J. *J. Vac. Sci. Technol. B* **2001**, *19*, 1091.
- (143) Wang, Z. L. *Adv. Mater.* **2003**, *15*, 1497.
- (144) Datye, A. K. *J. Catal.* **2003**, *216*, 144.
- (145) Martínez-Arias, A.; Fernández-García, M.; Iglesias-Juez, A.; Anderson, J. A.; Conesa, J. C.; Soria, J. *Appl. Catal. B* **2000**, *28*, 29.
- (146) Iglesias-Juez, A.; Hungria, A. B.; Martínez-Arias, A.; Fuerte, A.; Fernández-García, M.; Anderson, J. A.; Conesa, J. C.; Soria, J. *J. Catal.* **2003**, *217*, 310.
- (147) Yin, J. S.; Wang, Z. L. *Phys. Rev. Lett.* **1997**, *79*, 2570.
- (148) O'Keefe, M. A.; Buseck, P. R.; Iijima, S. *Nature* **1978**, *274*, 322.
- (149) Bernal, S.; Botana, F. J.; Calvino, J. J.; López-Cartes, C.; Pérez-Omil, J. A.; Rodríguez-Izquierdo, J. M. *Ultramicroscopy* **1998**, *72*, 135.
- (150) Klenov, D.; Kryukova, G. N.; Plyasova, L. M. *J. Mater. Chem.* **1998**, *8*, 1665.
- (151) Sun, K.; Liu, J.; Browning, N. D. *J. Catal.* **2002**, *205*, 266.
- (152) Hansen, P. L.; Wagner, J. B.; Helveg, S.; Rostrup-Nielsen, J. R.; Clausen, B. S.; Topsoe, H. *Science* **2002**, *295*, 2053.
- (153) Gai, P. L. *Top. Catal.* **2002**, *21*, 161.
- (154) Young, R.; Ward, J.; Scire, F. *Phys. Rev. Sci. Instrum.* **1972**, *43*, 999.
- (155) Young, R.; Ward, J.; Scire, F. *Phys. Rev. Lett.* **1971**, *27*, 922.
- (156) Binnig, G.; Rohrer, H. *Rev. Mod. Phys.* **1987**, *59*, 615.
- (157) Rohrer, H. *Ultramicroscopy* **1992**, *42-44*, 1.
- (158) Hamers, R. J. *J. Phys. Chem.* **1996**, *100*, 13103.
- (159) Magonov, S. N.; Whangbo, M.-H. *Surface Analysis with STM and AFM*; VCH: New York, 1996.
- (160) Tersoff, J.; Hamann, D. R. *Phys. Rev. B* **1985**, *31*, 805.
- (161) Hamers, R. J. *J. Vac. Sci. Technol. B* **1988**, *6*, 1462.
- (162) Feenstra, R. M. *Phys. Rev. B* **1991**, *44*, 13791.
- (163) Kubby, J. A.; Boland, J. J. *Surf. Sci. Rep.* **1996**, *26*, 61.
- (164) Sautet, P. *Chem. Rev.* **1997**, *97*, 1097.
- (165) Carlisle, C. I.; King, D.; Bocquet, M.-L.; Cerdá, J.; Sautet, P. *Phys. Rev. Lett.* **2000**, *84*, 3899.
- (166) Golloway, H.; Sautet, P.; Salmeron, M. *Phys. Rev. B* **1996**, *54*, R11 145.
- (167) Tersoff, J.; Hamann, D. R. *Phys. Rev. Lett.* **1983**, *50*, 1998.
- (168) Tersoff, J. *Phys. Rev. B* **1989**, *40*, 11990.
- (169) Chen, C. J. *J. Vac. Sci. Technol. A* **1991**, *9*, 44.
- (170) Tsukada, M.; Kobayashi, K.; Isshiki, N.; Kageshima, H.; Uchiyama, T.; Watanabe, S.; Schimizu, T. *Surf. Sci. Rep.* **1991**, *13*, 265.
- (171) Tsukada, M.; Kageshima, H.; Isshiki, N.; Kobayashi, K. *Surf. Sci.* **1992**, *266*, 253.
- (172) Sacks, W.; Noguera, C. *Ultramicroscopy* **1992**, *42-44*, 140.
- (173) Tekman, E.; Ciraci, S. *Phys. Rev. B* **1989**, *40*, 10286.
- (174) Sacks, W.; Noguera, C. *J. Vac. Sci. Technol. B* **1991**, *9*, 488.
- (175) Sacks, W.; Noguera, C. *Phys. Rev. B* **1991**, *43*, 11612.
- (176) Ciraci, S.; Baratoff, A.; Batra, I. P. *Phys. Rev. B* **1990**, *42*, 7618.
- (177) Kubby, J. A.; Wang, Y. R.; Greene, W. J. *Phys. Rev. Lett.* **1991**, *65*, 2165.
- (178) Diebold, U. *Surf. Sci. Rep.* **2003**, *48*, 53.
- (179) Li, M.; Hebenstreit, W.; Gross, L.; Diebold, U.; Henderson, M. A.; Jennison, D. R.; Schultz, P. A.; Sears, M. P. *Surf. Sci.* **1999**, *437*, 173.
- (180) Surnev, S.; Kresse, G.; Sock, M.; Ramsey, M. G.; Netzer, F. P. *Surf. Sci.* **2001**, *495*, 91.
- (181) Surnev, S.; Kresse, G.; Ramsey, M. G.; Netzer, F. P. *Phys. Rev. Lett.* **2001**, *87*, 086102.
- (182) Norenberg, H.; Briggs, G. A. D. *Phys. Rev. Lett.* **1997**, *79*, 4222.
- (183) Batzill, M.; Beck, D. E.; Koel, B. E. *Phys. Rev. B* **2001**, *64*, 245402.
- (184) Valden, M.; Lai, X.; Goodman, D. W. *Science* **1998**, *281*, 1647.
- (185) Hamers, R. J.; Tromp, R. M.; Demuth, J. E. *Phys. Rev. Lett.* **1986**, *56*, 1972.
- (186) Hamers, R. J. *Annu. Rev. Phys.* **1989**, *40*, 531.
- (187) García, R.; Pérez, R. *Surf. Sci. Rep.* **2002**, *47*, 197.
- (188) Martin, Y.; Williams, C. C.; Wickramasinghe, H. K. *J. Appl. Phys.* **1987**, *61*, 4723.
- (189) Anselmetti, D.; Lüthi, R.; Meyer, E.; Richmond, T.; Dreier, M.; Frommer, J. E.; Güntherodt, H.-J. *Nanotechnology* **1994**, *5*, 87.
- (190) Albrecht, T. R.; Grütter, P.; Horne, D.; Rugar, D. *J. Appl. Phys.* **1991**, *69*, 668.
- (191) Giessibl, F. J. *Science* **1995**, *267*, 68.
- (192) Sugawara, Y.; Othna, M.; Ueyama, H.; Morita, S. *Science* **1995**, *270*, 1646.
- (193) Kitamura, S.; Iwatsuki, M. *Jpn. J. Appl. Phys.* **1995**, *35*, L145.
- (194) Smith, R. L.; Rohrer, G. S. *J. Catal.* **1996**, *163*, 12.
- (195) Smith, R. L.; Rohner, G. S. *MRS Symposium Proc.* **1997**, *497*, 53.
- (196) Chen, J.; Workman, R. K.; Sarid, D.; Hoper, R. *Nanotechnology* **1994**, *5*, 199.
- (197) García, R.; San Paulo, A. *Phys. Rev. B* **1999**, *60*, 4961.
- (198) Sahin, O.; Atalar, A. *Appl. Phys. Lett.* **2001**, *78*, 2973.
- (199) Cabaret, D.; Sainterit, P.; Idelfonse, P.; Flank, A. M. *J. Phys. Condens. Matter* **1996**, *8*, 3691.
- (200) Mozoguchi, T.; Tanaka, I.; Yoshida, M.; Oba, F.; Ogasawara, K.; Adachi, H. *Phys. Rev. B* **2000**, *61*, 2180.
- (201) Wu, Z. Y.; Ouward, G.; Gressier, P.; Natoli, C. R. *Phys. Rev. B* **1997**, *55*, 10383.
- (202) Farges, F.; Brown, G. E., Jr.; Rehr, J. J. *Phys. Rev. B* **1997**, *56*, 1809.
- (203) Sipr, O.; Simunek, A.; Bocharov, S.; Kirchner, Th.; Drager, G. *Phys. Rev. B* **1999**, *60*, 14115.
- (204) Wu, Z. Y.; Gota, S.; Jollet, F.; Pollak, M.; Gautier-Soyer, M.; Natoli, C. R. *Phys. Rev. B* **1997**, *55*, 2570.
- (205) Chen, L. X.; Liu, T.; Thurmauer, M.; Csencsits, R.; Rajh, T. *J. Phys. Chem. B* **2002**, *106*, 8539.
- (206) Wu, Z.; Xian, D. C.; Natoli, C. R.; Marcelli, A.; Paris, E.; Mollans, A. *Appl. Phys. Lett.* **2001**, *79*, 1918.
- (207) Van der Laan, G. V.; Zaanen, J.; Sawatzky, G. A.; Karnatak, R.; Estern, J. M. *Phys. Rev. B* **1986**, *33*, 4253.
- (208) Soldatov, A. V.; Ivanchenko, T. S.; Della Longa, S.; Kotani, A.; Iwamoto, Y.; Bianconi, A. *Phys. Rev. B* **1994**, *50*, 5074.
- (209) Altearelli, M.; Dexter, D. L.; Nussenzweig, H. M. *Phys. Rev. B* **1972**, *6*, 4502.
- (210) De Groot, F. M. F. *Chem. Rev.* **2001**, *101*, 1779.

- (211) Hamalainen, K.; Siddons, P.; Hastings, J. B.; Berman, L. E. *Phys. Rev. Lett.* **1991**, *67*, 2850.
- (212) Pannkov, J. I. *Optical Processes in Semiconductors*; Dover: Mineola, NY, 1971.
- (213) Alivisatos, A. P. *J. Phys. Chem.* **1996**, *100*, 13226.
- (214) Yoffe, A. D. *Adv. Phys.* **2001**, *50*, 1.
- (215) Bawendi, M. G.; Wilson, W. L.; Rothberg, L.; Carroll, P. J.; Jedji, T. M.; Steigerward, M. L.; Brus, L. E. *Phys. Rev. Lett.* **1990**, *65*, 1623.
- (216) Laheld, V. E. H.; Einevoll, G. T. *Phys. Rev. B* **1997**, *55*, 5184.
- (217) Efron, A. L.; Rosen, M.; Kuno, M.; Normal, M.; Norris, D. J.; Bawendi, M. *Phys. Rev. B* **1996**, *54*, 4843.
- (218) Von Grumber, H. H. *Phys. Rev. B* **1997**, *55*, 2293.
- (219) Tomasulo, A.; Ramakrisna, M. V. *J. Chem. Phys.* **1996**, *105*, 3612.
- (220) Wang, L.-W.; Kim, J.; Zunger, A. *Phys. Rev. B* **1999**, *59*, 5678.
- (221) Uzomi, T.; Kayanuma, Y.; Yamanaka, K.; Edamatsu, K.; Itoh, T. *Phys. Rev. B* **1999**, *59*, 9826.
- (222) Iwamoto, M.; Abe, T.; Tachibana, Y. *J. Mol. Catal. A* **2000**, *55*, 143.
- (223) Vigil, O.; Cruz, F.; Morales-Acabedo, A.; Contreras-Puente, G.; Vaillant, L.; Santana, G. *Mater. Chem. Phys.* **2001**, *68*, 249.
- (224) Borgohain, K.; Morase, N.; Mahumani, S. *J. Appl. Phys.* **2002**, *92*, 1292.
- (225) Suzuki, T.; Kosacki, I.; Petrovsky, V.; Anderson, H. U. *J. Appl. Phys.* **2001**, *91*, 2308.
- (226) Serpone, N.; Lawless, D.; Khairutdinov, R. *J. Phys. Chem.* **1995**, *98*, 16646.
- (227) Monticone, S.; Tufeu, R.; Kanaev, A. V.; Scolan, E.; Sánchez, C. *Appl. Surf. Sci.* **2000**, *162–163*, 565.
- (228) Viswanaha, R.; Sapra, S.; Satyani, B.; Der, B. N.; Sarma, D. D. *J. Mater. Sci.* **2004**, *14*, 661.
- (229) Tsunekawa, S.; Fukuda, T.; Kasuya, A. *J. Appl. Phys.* **2000**, *87*, 1318.
- (230) Ong, H. C.; Zhu, A. X. E.; Du, G. T. *Appl. Phys. Lett.* **2002**, *80*, 941.
- (231) Kang, J.; Tsunekawa, S.; Kasuya, A. *Appl. Surf. Sci.* **2001**, *174*, 306.
- (232) Kosacki, I.; Petrovsky, V.; Anderson, H. U. *Appl. Phys. Lett.* **1999**, *74*, 341.
- (233) Reddy, K. M.; Manorama, S. V.; Reddy, A. R. *Mater. Chem. Phys.* **2002**, *78*, 239.
- (234) Iyer, S. S.; Xie, Y.-H. *Science* **1993**, *260*, 40.
- (235) Mahmood, S. A.; Akl, A. A.; Kand, H.; Abdel-Had, K. *Phys. B* **2002**, *111*, 366.
- (236) Matsumoto, T.; Suzuki, J.-I.; Ohmura, M.; Kanemitsu, Y.; Masumoto, Y. *Phys. Rev. B* **2001**, *63*, 195322.
- (237) Einstein, A. *Ann. Phys. Leipzig* **1905**, *17*, 132.
- (238) Briggs, D.; Seah, M. P. *Practical Surface Analysis by Auger and X-ray Photoelectron Spectroscopy*; Wiley: New York, 1983.
- (239) Siegbahn, K.; Nordling, C.; Fahlman, A.; Nordberg, H.; Hamrin, K.; Hedman, J.; Johansson, G.; Bergmark, T.; Karlsson, S. E.; Lindgren, J.; Lindberg, B. *Electron Spectroscopy for Chemical Analysis*; Almqvist and Wiksells: Stockholm, 1967.
- (240) Turner, D. W.; Baker, C.; Baker, A. D.; Brundle, C. R. *Molecular Photoelectron Spectroscopy*; Wiley: London, 1970.
- (241) Spicer, W. E. *Phys. Rev.* **1962**, *125*, 1297.
- (242) Rabalais, J. W. *Principles of Ultraviolet Photoelectron Spectroscopy*; Wiley: New York, 1977.
- (243) Hrbek, J. In *Chemical Applications of Synchrotron Radiation*; T. K. Sham, Ed.; World Scientific: New Jersey, 2002.
- (244) *Synchrotron Radiation, Techniques and Applications*; Kunz, C., Ed.; Springer-Verlag: Berlin, 1979.
- (245) Ferrer, S.; Petroff, Y. *Surf. Sci.* **2002**, *500*, 605.
- (246) Polcik, M.; Wilde, L.; Haase, J.; Brenna, B.; Cocco, D.; Comelli, G.; Paolucci, G. *Phys. Rev. B* **1996**, *53*, 13720.
- (247) Hrbek, J.; Yang, Y. W.; Rodriguez, J. A. *Surf. Sci.* **1993**, *296*, 164.
- (248) Lee, A. F.; Wilson, K.; Middleton, R. L.; Baraldi, A.; Goldoni, A.; Paolucci, G.; Lambert, R. M. *J. Am. Chem. Soc.* **1999**, *121*, 7969.
- (249) Soriano, L.; Abbate, M.; Fernández, A.; González-Elipse, A. R.; Sirotti, F.; Rossi, G.; Sanz, J. M. *Chem. Phys. Lett.* **1997**, *266*, 184.
- (250) Smith, K. E.; Mackay, J. L.; Henrich, V. E. *Phys. Rev. B* **1987**, *35*, 5822.
- (251) Rodriguez, J. A.; Pérez, M.; Jirsak, T.; González, L.; Maiti, A.; Larese, J. Z. *J. Phys. Chem. B* **2001**, *105*, 5497.
- (252) Soriano, L.; Abbate, M.; Fernández, A.; González-Elipse, A. R.; Sirotti, F.; Sanz, J. M. *J. Phys. Chem. B* **1999**, *103*, 6676.
- (253) Rodriguez, J. A.; Campbell, C. T. *J. Phys. Chem. B* **1987**, *91*, 6648.
- (254) Chaturvedi, S.; Rodriguez, J. A.; Hrbek, J. *J. Phys. Chem. B* **1997**, *101*, 10860.
- (255) Liu, G.; Rodríguez, J. A.; Hrbek, J.; Dvorak, J.; Peden, C. H. F. *J. Phys. Chem. B* **2001**, *105*, 7762.
- (256) Rodriguez, J. A.; Azad, S.; Wang, L.-Q.; García, J.; Etxebarria, A.; González, L. *J. Chem. Phys.* **2003**, *118*, 6562.
- (257) Wagner, C. D.; Riggs, W. M.; Davis, L. E.; Moulder, J. F.; Muilenberg, G. E. *Handbook of X-ray Photoelectron Spectroscopy*; Perkin-Elmer: Eden Prairie, Minnesota, 1978.
- (258) Yeh, J.-J.; Lindau, I.; Sun, J.-Z.; Char, K.; Missert, N.; Kapitulnik, A.; Geballe, T. H.; Beasley, M. R. *Phys. Rev. B* **1990**, *42*, 8044.
- (259) Bagus, P. S.; Pacchioni, G.; Sousa, C.; Minerva, T.; Parmigiani, F. *Chem. Phys. Lett.* **1992**, *196*, 641.
- (260) Wertheim, G. K. *J. Electron. Spectrosc.* **1984**, *34*, 309.
- (261) Hill, D. M.; Meyer, H. M.; Weaver, J. H. *Surf. Sci.* **1990**, *225*, 63.
- (262) Vazquez, R. P. *J. Electron. Spectrosc.* **1991**, *56*, 217.
- (263) Sangaletti, L.; Depero, L. E.; Bagus, P. S.; Parmigiani, F. *Chem. Phys. Lett.* **1995**, *245*, 463.
- (264) Bagus, P. S.; Freund, H. J.; Minerva, T.; Pacchioni, G.; Parmigiani, F. *Chem. Phys. Lett.* **1996**, *251*, 90.
- (265) Bagus, P. S.; Pacchioni, G.; Parmigiani, F. *Chem. Phys. Lett.* **1993**, *207*, 569.
- (266) Hennig, D.; Ganduglia-Pirovano, M. V.; Scheffler, M. *Phys. Rev. B* **1996**, *53*, 10344.
- (267) Wu, R.; Freeman, A. J. *Phys. Rev. B* **1995**, *52*, 12419.
- (268) Wu, M.-C.; Truong, C. M.; Goodman, D. W. *Phys. Rev. B* **1992**, *46*, 12688.
- (269) Borgohain, K.; Singh, J. B.; Rao, M. V. M.; Shripathi, T.; Mahamuni, S. *Phys. Rev. B* **2000**, *61*, 11093.
- (270) Jensen, F. *Introduction to Computational Chemistry*; Wiley: New York, 1999.
- (271) Springborg, M. *DFT Methods in Chemistry and Materials Science*; Wiley: New York, 1997.
- (272) Koch, W.; Holthausen, M. C. *A Chemist's Guide to Density Functional Theory*; Wiley-VCH: Weinheim, 2000.
- (273) Ziegler, T. *Chem. Rev.* **1991**, *91*, 651.
- (274) Hammer, B.; Nørskov, J. K. *Adv. Catal.* **2000**, *45*, 1.
- (275) Chong, D. P. *Recent Advances in Density Functional Methods*; World Scientific: Singapore, 1995.
- (276) Ernzerhof, M.; Scuseria, G. E. *Theor. Chem. Acc.* **2000**, *103*, 259.
- (277) Pople, J. A. *Rev. Mod. Phys.* **1999**, *71*, 1267.
- (278) Hehre, W. J.; Radom, L.; Schelyer, P. R.; Pople, J. A. *Ab Initio Molecular Orbital Theory*; Wiley: New York, 1986.
- (279) Kohn, W. *Rev. Mod. Phys.* **1999**, *103*, 1253.
- (280) Parr, R. G.; Yang, W. *Density Functional Theory of Atoms and Molecules*; Oxford University Press: New York, 1989.
- (281) Szabo, A.; Ostlund, N. S. *Modern Quantum Chemistry*; McGraw-Hill: New York, 1982.
- (282) Roothaan, C. C. *Rev. Mod. Phys.* **1951**, *23*, 69.
- (283) Bartlett, R. J. *Annu. Rev. Phys. Chem.* **1981**, *32*, 359.
- (284) Bacon, A. D.; Zerner, M. C. *Theor. Chim. Acta* **1979**, *53*, 21.
- (285) Thiel, W.; Voityuk, A. A. *J. Phys. Chem.* **1996**, *100*, 616.
- (286) Poveda, F. M.; Sierralta, A.; Villaveces, J. L.; Ruetter, F. *J. Mol. Catal. A* **1996**, *106*, 109.
- (287) Blyholder, G.; Head, J.; Ruetter, F. *Theor. Chim. Acta* **1982**, *60*, 429.
- (288) Bredow, T.; Geudtner, G.; Jug, K. *J. Comput. Chem.* **2001**, *22*, 861.
- (289) Voityuk, A. A.; Rösch, N. *J. Phys. Chem. A* **2000**, *104*, 4089.
- (290) Kryachko, E. S.; Ludeña, E. V. *Density Functional Theory of Many Electron Systems*; Kluwer: Dordrecht, The Netherlands, 1990.
- (291) Hohenberg, P.; Kohn, W. *Phys. Rev. B* **1964**, *136*, 864.
- (292) Geerlings, P.; DeProft, F.; Langenaeker, W. *Chem. Rev.* **2003**, *103*, 1793.
- (293) Kohn, W.; Sham, L. J. *Phys. Rev.* **1965**, *140*, A1133.
- (294) Ceperly, D. M.; Alder, B. J. *Phys. Rev. Lett.* **1980**, *45*, 566.
- (295) Becke, A. D. *Phys. Rev. A* **1988**, *38*, 3098.
- (296) Perdew, J. P. In *Electronic Structure of Solids '91*; Ziesche, P., Esching, H., Eds.; Academic: Berlin, 1991.
- (297) Wang, Y.; Perdew, J. P. *Phys. Rev. B* **1991**, *44*, 13298.
- (298) Lee, C.; Yang, W.; Parr, R. G. *Phys. Rev. B* **1988**, *37*, 785.
- (299) Perdew, J. P.; Burke, K.; Ernzerhof, M. *Phys. Rev. Lett.* **1996**, *77*, 3865.
- (300) Becke, A. D. *J. Chem. Phys.* **1993**, *98*, 5648.
- (301) Hamprecht, F. A.; Cohen, A. J.; Tozer, D. J.; Handy, N. C. *J. Chem. Phys.* **1998**, *109*, 6264.
- (302) De Oliveira, G.; Martin, J. M. L.; De Proft, F.; Geerlings, P. *Phys. Rev. A* **1999**, *60*, 1034.
- (303) De Proft, F.; Geerlings, P. *J. Chem. Phys.* **1997**, *106*, 3270.
- (304) Curtiss, L. A.; Redfern, P. C.; Raghavachari, K.; Pople, J. A. *J. Chem. Phys.* **1998**, *109*, 42.
- (305) De Proft, F.; Martin, J. M. L.; Geerlings, P. *Chem. Phys. Lett.* **1996**, *250*, 393.
- (306) De Proft, F.; Tielens, F.; Geerlings, P. *J. Mol. Struct. (THEO-CHEM)* **2000**, *506*, 1.
- (307) Scott, A. P.; Radom, L. *J. Phys. Chem.* **1996**, *100*, 16502.
- (308) Moukara, M.; Stadele, M.; Majewski, J. A.; Vogl, P.; Gorling, A. *J. Phys. Condens. Matter* **2000**, *12*, 6783.
- (309) Cordatos, H.; Ford, D.; Gorte, R. J. *J. Phys. Chem.* **1996**, *100*, 18128.
- (310) Conesa, J. C. *Surf. Sci.* **1995**, *339*, 337.

- (311) Balducci, G.; Kaspar, J.; Fornasiero, P.; Graziani, M.; Islam, M. S.; Gale, J. D. *J. Phys. Chem. B* **1997**, *101*, 1750.
- (312) Gale, J. D. *J. Chem. Soc., Faraday Trans.* **1997**, *93*, 629.
- (313) Bosh, H.; Janssen, F. *Catal. Today* **1988**, *2*, 369.
- (314) Forzatti, P. *Catal. Today* **2000**, *62*, 51.
- (315) Hoffman, M. R.; Martin, S. T.; Choi, W.; Wahneman, D. W. *Chem. Rev.* **1995**, *95*, 69.
- (316) Maldoti, A.; Molinari, A.; Amadeni, R. *Chem. Rev.* **2002**, *102*, 3811.
- (317) Kalyanasendevan, K.; Gratzel, M. in *Optoelectronic Properties of Inorganic Compounds*; Roundhill, D. M., Fackler, J. P., Eds.; Plenum: New York, 1999; pp 169–194.
- (318) Sheveglieri, G., Ed.; *Gas Sensors*; Kluwer: Dordrecht, 1992.
- (319) Johnson, R. W.; Thieles, E. S.; French, R. H. *Tappi. J.* **1997**, *80*, 233.
- (320) Phillips, L. G.; Barbeno, D. M. *J. Dairy Sci.* **1997**, *80*, 2726.
- (321) Selhofer, H. *Vacuum Thin Films* August 1999, 15.
- (322) Fujishima, A.; Rao, T. N.; Tryk, D. A. *J. Photochem. Photobiol. C: Photochem. Rev.* **2000**, *1*, 1.
- (323) Sousa, C.; Illas, F. *Phys. Rev. B* **1994**, *50*, 13974.
- (324) Bonhole, P.; Gogniat, E.; Gratzel, M.; Ashrit, P. V. *Thin Solid Films* **1999**, *350*, 269.
- (325) Marchand, R.; Broham, L.; Tournoux, M. *Mater. Res. Bull.* **1980**, *15*, 1129.
- (326) Muscat, J.; Swany, V.; Harrison, N. M. *Phys. Rev. B* **2002**, *65*, 224112.
- (327) Zhang, H.; Banfield, J. F. *J. Phys. Chem. B* **2000**, *104*, 3481.
- (328) Lazzeri, M.; Vittadini, A.; Selloni, A. *Phys. Rev. B* **2001**, *63*, 155409.
- (329) Depero, L. E.; Sangetti, L.; Allieri, B.; Bontempi, E.; Marino, A.; Zocchi, M. *J. Cryst. Growth* **1999**, *198/199*, 516.
- (330) Chemseddine, A.; Moritz, T. *Eur. J. Inorg. Chem.* **1999**, 235.
- (331) Wang, C.-C.; Ying, J. Y. *Chem. Mater.* **1999**, *11*, 3133.
- (332) Wu, M.; Long, J.; Huang, A.; Luo, Y. *Langmuir* **1999**, *15*, 8822.
- (333) Huang, W.; Tang, X.; Wang, Y.; Kolybin, Y.; Gedankan, A. *Chem. Commun.* **2000**, 1415.
- (334) Yin, H.; Wada, Y.; Kitamura, T.; Kambe, S.; Murasawa, A.; Mori, H.; Sakata, T.; Yangida, S. *J. Mater. Chem.* **2001**, *11*, 1694.
- (335) Aruna, S. T.; Tirosh, S.; Zaban, A. *J. Mater. Chem.* **2000**, *10*, 2388.
- (336) Kominami, H.; Kohno, M.; Kera, Y. *J. Mater. Chem.* **2000**, *10*, 1151.
- (337) Ding, X. Z.; Liu, X.-H. *J. Mater. Res.* **1998**, *13*, 2556.
- (338) Hu, Y.; Tsai, H.-L.; Huang, C.-L. *Mater. Res. Eng. A* **2003**, *344*, 209.
- (339) Gouma, P. I.; Millis, M. J. *J. Am. Ceram. Soc.* **2001**, *84*, 619.
- (340) Penn, R. L.; Banfield, J. F. *Am. Mineral.* **1999**, *84*, 1231.
- (341) Sakthivel, S.; Kirsch, H. *Angew. Chem., Int. Ed.* **2003**, *42*, 4908.
- (342) Sansonov, G. V. *The Oxide Handbook*; IFI/plenum Press: New York, 1982.
- (343) Yagi, E.; Hasiguti, R. *Phys. Rev. B* **1996**, *54*, 7945.
- (344) Smith, D. J.; Bursill, L. A.; Blanchin, M. G. *Philos. Mag. A* **1984**, *50*, 473.
- (345) Knauth, P.; Tuller, H. L. *J. Appl. Phys.* **1999**, *85*, 897.
- (346) Bersani, D.; Antonioli, G.; Lottici, P. P.; Lopez, L. *J. Non-Cryst. Sol.* **1998**, *232–234*, 175.
- (347) Guidi, V.; Carotta, M. C.; Ferroni, M.; Martinelli, G.; Sacerdoti, M. *J. Phys. Chem. B* **2003**, *107*, 120.
- (348) Fuente, A.; Hernández-Alonso, M. D.; Maira, A. J.; Martínez-Arias, A.; Fernández-García, M.; Conesa, J. C.; Soria, J.; Munuera, G. *J. Catal.* **2002**, *212*, 1.
- (349) Loca, V.; Thomson, S.; Howe, R. F. *J. Chem. Soc., Faraday Trans.* **1997**, *93*, 2195.
- (350) Wang, J. A.; Limas-Ballesteros, R.; López, T.; Moreno, A.; Gómez, R.; Novaro, O.; Bokhim, X. *J. Phys. Chem. B* **2001**, *105*, 9692.
- (351) Fernández-García, M., unpublished results.
- (352) Depero, L. E.; Marino, A.; Allieri, B.; Bontempi, E.; Sangaletti, L.; Casale, C.; Notaro, M. *J. Mater. Res.* **2000**, *15*, 2080.
- (353) Al-Salim, N. I.; Bagshaw, S. A.; Bittar, A.; kemmit, T.; McQuil-lan, A. J.; Mills, A. M.; Ryan, M. J. *J. Mater. Chem.* **2000**, *10*, 2358.
- (354) Sensato, F. R.; Custodio, R.; Longo, E.; Beltrán, A.; Andrés, J. *Catal. Today* **2003**, *85*, 145.
- (355) Fuente, A.; Hernández-Alonso, M. D.; Maira, A. J.; Martínez-Arias, A.; Fernández-García, M.; Conesa, J. C.; Soria, J. *Chem. Commun.* **2001**, 2178.
- (356) Xu, A.-W.; Gao, Y.; Liu, H.-Q.; *J. Catal.* **2002**, *207*, 151.
- (357) *Science and Technology of Zirconia, Advances in Ceramics*; Heuer, A. H., Hobbs, L. W., Eds.; The American Ceramics Society, Westerville, OH, 1981; Vol. 3.
- (358) Steele, B. C. H.; Heinzl, A. *Nature* **2001**, *414*, 345.
- (359) Brailsford, A. D.; Logothetis, E. M. *Sensors Actuators B* **1998**, *52*, 195.
- (360) Somov, S. I.; Reinhardt, G.; Guth, U.; Gopel, W. *Solid State Ionics* **2000**, *136–137*, 543.
- (361) Stichert, W.; Shüth, F. *Chem. Mater.* **1998**, *10*, 2020.
- (362) Garvie, R. C. *J. Phys. Chem.* **1965**, *69*, 1238.
- (363) Clearfield, A. *Inorg. Chem.* **1964**, *3*, 146.
- (364) Mitsuhashi, T.; Ichihara, M.; Taksuke, U. *J. Am. Ceram. Soc.* **1974**, *57*, 97.
- (365) Garvie, R. C. *J. Phys. Chem.* **1978**, *82*, 218.
- (366) Baldinozzi, G.; Simeone, D.; Gosset, D.; Dutheil, M. *Phys. Rev. Lett.* **2003**, *90*, 216103.
- (367) Mayo, M. J.; Seidensticker, J. R.; Hague, D. C.; Carim, A. H. *Nanostructured Mater.* **1999**, *11*, 271.
- (368) Bravo-León, A.; Morikawa, Y.; Kawahara, M.; Mayo, M. J. *Acta Mater.* **2002**, *50*, 4555.
- (369) Howard, C. J.; Kisi, E.; Ohtaka, O. *J. Am. Ceram. Soc.* **1991**, *74*, 2321.
- (370) (a) McCullough, J. D.; Trueblood, K. N. *Acta Crystallogr.* **1959**, *15*, 1187. (b) Smith, D. K.; Newkirk, H. W. *Acta Crystallogr.* **1965**, *18*, 982.
- (371) Finnis, M. W.; Paxton, A. T.; Methfessel, M.; van Schilf-gaarde, M. *Phys. Rev. Lett.* **1998**, *81*, 5149.
- (372) Bouvier, P.; Godlewski, J.; Lucazeau, G. *J. Nucl. Mater.* **2002**, *300*, 118.
- (373) Stichert, W.; Schüth, F. *Chem. Mater.* **1998**, *10*, 2020.
- (374) Pacheco, G.; Fripiat, J. J. *J. Phys. Chem. B* **2000**, *104*, 11906.
- (375) Mayo, M. J.; Suresh, A.; Porter, W. D. *Rev. Adv. Mater. Sci.* **2003**, *5*, 100.
- (376) Xie, S.; Iglesia, E.; Bell, A. T. *Chem. Mater.* **2000**, *12*, 2442.
- (377) Srinivasan, R.; Watkins, T. R.; Hubbard, C. R.; Davis, B. H. *Chem. Mater.* **1995**, *7*, 725.
- (378) Djurado, E.; Dessemond, L.; Roux, C. *Solid State Ionics* **2000**, *136–137*, 1249.
- (379) Chadwick, A. V.; Mountjoy, G.; Nield, V. M.; Poplett, I. J. F.; Smith, M. E.; Strange, J. H.; Tucker, M. G. *Chem. Mater.* **2001**, *13*, 1219.
- (380) Li, M.; Feng, Z.; Xiong, G.; Ying, P.; Xin, Q.; Li, C. *J. Phys. Chem. B* **2001**, *105*, 8107.
- (381) Li, M.; Feng, Z.; Ying, P.; Xin, Q.; Li, C. *Phys. Chem. Chem. Phys.* **2003**, *5*, 5326.
- (382) Tsunekawa, S.; Ito, S.; Kawazoe, Y.; Wang, J.-T. *Nano Lett.* **2003**, *3*, 871.
- (383) Meldrum, A.; Boatner, L. A.; Ewing, R. C. *Phys. Rev. Lett.* **2002**, *88*, 25503.
- (384) Sickafus, K. E.; Matzke, H.; Hartmann, Th.; Yasuda, K.; Valdez, J. A.; Chodak, P., III; Nastasi, M.; Verrall, R. A. *J. Nucl. Mater.* **1999**, *274*, 66.
- (385) Boulch, F.; Djurado, E. *Solid State Ionics* **2003**, *157*, 335.
- (386) Adachi, G.; Imanaka, N.; Tamura, S. *Chem. Rev.* **2002**, *102*, 2405.
- (387) Boulch, F.; Dessemond, L.; Djurado, E. *Solid State Ionics* **2002**, *154–155*, 143.
- (388) Liu, D. *J. Mater. Sci. Lett.* **1998**, *17*, 467.
- (389) Schoonman, J. *Solid State Ionics* **2000**, *135*, 5.
- (390) Mondal, P.; Klein, A.; Jaegermann, W.; Hahn, H. *Solid State Ionics* **1999**, *118*, 331.
- (391) Knöner, G.; Reimann, K.; Röwer, R.; Södervall, U.; Schaefer, H. *Proc. Nat. Acad. Sci. U.S.A.* **2003**, *100*, 3870.
- (392) Brossmann, U.; Würschum, R.; Södervall, U.; Schaefer, H. *J. Appl. Phys.* **1999**, *85*, 7646.
- (393) Rajh, T.; Chen, L. X.; Lukas, K.; Liu, T.; Thurnauer, M. C.; Tiede, D. M. *J. Phys. Chem. B* **2002**, *106*, 10543.
- (394) Scherzman, K. in *Catalysis by Ceria and Related Materials*; Trovarelli, A., Ed.; World Scientific: London, 2002; Chapter 1.
- (395) Thompson, A. M. *Oxides of the Rare Earths*; Wiley: New York, 1978.
- (396) Nöremberg, H.; Briggs, G. A. D. *Phys. Rev. Lett.* **1997**, *79*, 4222.
- (397) Fujimori, A. *Phys. Rev. B* **1983**, *28*, 2281.
- (398) Wuilloud, E.; Delley, B.; Schneider, W.-D.; Baer, Y. *Phys. Rev. Lett.* **1984**, *53*, 202.
- (399) Marabelli, F.; Wachter, P. *Phys. Rev. B* **1987**, *36*, 1987.
- (400) Koelling, D. D.; Boring, A. M.; Wood, J. H. *Solid State Commun.* **1983**, *47*, 227.
- (401) Liu, G.; Rodriguez, J. A.; Chang, Z.; Hrbek, J.; Peden, C. H. F. *J. Phys. Chem. B* **2004**, *108*, 2931.
- (402) Shelef, M.; Graham, G. W. *Catal. Rev. Sci. Eng.* **1994**, *36*, 433.
- (403) Trovarelli, A. *Catal. Rev. Sci. Eng.* **1996**, *38*, 439.
- (404) Martínez-Arias, A.; Fernández-García, M.; Ballesteros, V.; Salamanca, L. N.; Conesa, J. C.; Otero, C.; Soria, J. *Langmuir* **1999**, *15*, 4797.
- (405) Fernández-García, M.; Martínez-Arias, A.; Hungria, A. B.; Iglesias-Juez, A.; Conesa, J. C.; Soria, J. *Phys. Chem. Chem. Phys.* **2002**, *4*, 2473.
- (406) Robinson, R. D.; Spanier, J. E.; Zhang, F.; Chan, S.-W.; Herman, I. P. *J. Appl. Phys.* **2002**, *92*, 1936.
- (407) Zhang, F.; Chan, S.-W.; Spanier, J. E.; Apak, E.; Jin, Q.; Robinson, R. D.; Herman, I. P. *J. Appl. Phys. Lett.* **2002**, *80*, 127.
- (408) Adachi, G.; Masui, T. In *Catalysis by Ceria and Related Materials*; Trovarelli, A., Ed.; Imperial College Press: London, 2002; Chapter 3.
- (409) Rodriguez, J. A.; Wang, X.; Hanson, J. C.; Liu, G.; Iglesias-Juez, A.; Fernández-García, M. *J. Chem. Phys.* **2003**, *119*, 5659.
- (410) Eck, S.; Castellarin-Cudia, C.; Surnev, S.; Ramsey, M. G.; Netzer, F. P. *Surf. Sci.* **2002**, *520*, 173.
- (411) Kašpar, J.; Fornasiero, P.; Graziani, M. *Catal. Today* **1999**, *50*, 285.

- (412) Nagai, Y.; Yamamoto, T.; Tanaka, T.; Yoshida, S.; Nonaka, T.; Okamoto, T.; Suda, A.; Sugiura, M. *Catal. Today* **2002**, *74*, 225.
- (413) Wang, X.; Hanson, J. C.; Rodriguez, J. A.; Iglesias-Juez, A.; Fernández-García, M., in preparation.
- (414) Chiang, Y. M.; Lavik, E. B.; Kosacki, I.; Tuller, H. L.; Ying, J. Y. *J. Electroceram.* **1997**, *1*, 7.
- (415) Fierro, J. L. G.; Soria, J.; Sanz, J.; Rojo, J. M. *J. Solid State Chem.* **1987**, *66*, 154.
- (416) Sohlberg, K.; Pantelides, S. K.; Pennycook, S. J. *J. Am. Chem. Soc.* **2001**, *123*, 6609.
- (417) Fu, Q.; Saltsburg, H.; Flytzani-Stephanopoulos, M. *Science* **2003**, *301*, 935.
- (418) Fernández-García, M.; Martínez-Arias, A.; Guerrero-Ruiz, A.; Conesa, J. C.; Soria, J. *J. Catal.* **2002**, *211*, 326.
- (419) Vlaic, G.; Di Monte, R.; Fornasiero, P.; Fonda, E.; Kašpar, J.; Graziani, M. *J. Catal.* **1999**, *182*, 378.
- (420) Liu, W.; Wadia, C.; Flytzani-Stephanopoulos, M. *Catal. Today* **1996**, *28*, 391.
- (421) Rodriguez, J. A.; Jirsak, T.; Freitag, A.; Hanson, J. C.; Larese, J. Z.; Chaturvedi, S. *Catal. Lett.* **1999**, *62*, 113.
- (422) Fu, Q.; Weber, A.; Flytzani-Stephanopoulos, M. *Catal. Lett.* **2001**, *77*, 87.
- (423) Shelef, M.; McCabe, R. W. *Catal. Today* **2000**, *62*, 35.
- (424) Colón, G.; Valdivieso, F.; Pijolat, M.; Baker, R. T.; Calvino, J. J.; Bernal, S. *Catal. Today* **1999**, *50*, 271.
- (425) Putna, E. S.; Bunluesin, T.; Fan, X. L.; Gorte, R. J.; Vohs, J. M.; Lakis, R. E.; Egami, T. *Catal. Today* **1999**, *50*, 343.
- (426) Yashima, M.; Arashi, H.; Kakihana, M.; Yoshimura, M. *J. Am. Ceram. Soc.* **1994**, *77*, 1067.
- (427) Kaspar, J.; Fornasiero, P.; Balducci, G.; Di Monte, R.; Hickey, N.; Sergio, V. *Inorg. Chim. Acta* **2003**, *349*, 217.
- (428) Martínez-Arias, A. M.; Fernández-García, A. B.; Hungria, J. C.; Conesa, G. Munuera, J. *Phys. Chem. B* **2003**, *107*, 2667.
- (429) de Carolis, S.; Pascual, J. L.; Petterson, L. G. M.; Baudin, M.; Wojcik, M.; Hermansson, K.; Palmqvist, A. E. C.; Muhammed, M. *J. Phys. Chem. B* **1999**, *103*, 7627.
- (430) Emsley, J. *The Elements*; Clarendon, Oxford, 1989.
- (431) Barr, T. L.; Brundle, C. R. *Phys. Rev. B* **1992**, *46*, 9199.
- (432) Guittet, M. J.; Crocombette, J. P.; Gautier-Soyer, M. *Phys. Rev. B* **2001**, *63*, 125117.
- (433) Bernal, S.; Blanco, G.; Cifredo, G. A.; Delgado, J. J.; Finol, D.; Gatica, J. M.; Rodríguez-Izquierdo, J. M.; Vidal, H. *Chem. Mater.* **2002**, *14*, 844.
- (434) Ikryannikova, L. N.; Aksenov, A. A.; Markaryan, G. L.; Muravéva, G. P.; Kostyuk, B. G.; Kharlanov, A. N.; Lunina, E. V. *Appl. Catal. A* **2001**, *210*, 225.
- (435) Föllner, A. M. *Magnesium Oxide and its Applications*; Vollhardt: Berlin, 1978.
- (436) Tasker, P. W. *Adv. Ceram.* **1984**, *10*, 176.
- (437) Gibson, A.; Haydock, R.; LaFemina, J. P. *J. Vac. Sci. Technol. A* **1992**, *10*, 2361.
- (438) Moodie, A. F.; Warble, C. E. *J. Cryst. Growth* **1971**, *10*, 26.
- (439) Mackrodt, W. C.; Tasker, P. W. *Chem. Br.* **1985**, *21*, 13.
- (440) DeSantis, E.; Ferrari, J., private communication.
- (441) Dohnálek, Z.; Kimmel, G. A.; McCreedy, D. E.; Young, J. S.; Dohnáková, A.; Smith, R. S.; Kay, B. D. *J. Phys. Chem. B* **2002**, *106*, 3526.
- (442) Rodriguez, J. A.; Jirsak, T.; Kim, J.-Y.; Larese, J. Z.; Maiti, A. *Chem. Phys. Lett.* **2000**, *330*, 475.
- (443) Soave, R.; Pacchioni, G. *Chem. Phys. Lett.* **2000**, *320*, 345.
- (444) Pacchioni, G.; Pescarmona, P. *Surf. Sci.* **1998**, *412/413*, 657.
- (445) Gibson, A.; Haydock, R.; LaFemina, J. P. *Appl. Surf. Sci.* **1993**, *72*, 285.
- (446) Giamello, E.; Paganini, M. C.; Murphy, D. M.; Ferrari, A. M.; Pacchioni, G. *J. Phys. Chem.* **1997**, *101*, 971.
- (447) Ferrari, A. M.; Pacchioni, G. *J. Phys. Chem.* **1996**, *100*, 9032.
- (448) Rodriguez, J. A. *Catal. Today* **2003**, *85*, 177.
- (449) Rodriguez, J. A.; Jirsak, T.; Pérez, M.; Chaturvedi, S.; Kuhn, M.; González, L.; Maiti, A. *J. Am. Chem. Soc.* **2000**, *122*, 12362.
- (450) Nagaoka, K.; Karasuda, T.; Aika, K. *J. Catal.* **1999**, *181*, 160.
- (451) Rodriguez, J. A.; Jirsak, T.; Pérez, M.; González, L.; Maiti, A. *J. Chem. Phys.* **2001**, *114*, 4186.
- (452) Tomishige, K.; Chen, Y.; Fujimoto, K. *J. Catal.* **1999**, *181*, 91.
- (453) Rodriguez, J. A.; Jirsak, T.; Freitag, A.; Larese, J. Z.; Maiti, A. *J. Phys. Chem. B* **2001**, *104*, 7439.
- (454) Rodriguez, J. A.; Jirsak, T.; González, L.; Evans, J.; Perez, M.; Maiti, A. *J. Chem. Phys.* **2001**, *115*, 10914.
- (455) Larese, J. Z., private communication.
- (456) Schmitz, P. J.; Baird, R. J. *J. Phys. Chem. B* **2002**, *106*, 4172.
- (457) Wang, X.; Hanson, J.; Rodriguez, J. A.; Szanyi, J., in preparation.
- (458) Carnes, C. L.; Klabunde, K. J. *Chem. Mater.* **2002**, *14*, 1806.
- (459) Klabunde, K. J.; Stark, J.; Koper, O.; Mobs, C.; Park, D. G.; Decker, S.; Jiang, Y.; Lagadic, I.; Zhang, D. *J. Phys. Chem.* **1996**, *100*, 12142.
- (460) Schneider, W. F. *J. Phys. Chem. B* **2004**, *108*, 273.
- (461) Pacchioni, G.; Ricart, J. M.; Illas, F. *J. Am. Chem. Soc.* **1994**, *116*, 10152.
- (462) Cimino, A.; Stone, F. S. *Adv. Catal.* **2002**, *47*, 141.
- (463) Stumpf, H. C.; Russel, A. S.; Newsome, J. W.; Tucker, C. M. *Ind. Eng. Chem.* **1950**, *42*, 1398.
- (464) McHale, J. M.; Novrotsky, A.; Perrota, A. J. *J. Phys. Chem. B* **1997**, *102*, 603.
- (465) Knozinger, H.; Ratnasamy, P. *Catal. Rev. Sic. Eng.* **1978**, *17*, 31.
- (466) Cai, S.-H.; Rashkeev, S. N.; Pantelides, S. T.; Sohlberg, K. *Phys. Rev. B* **2003**, *67*, 224104.
- (467) Sharma, P. K.; Varadan, V. V.; Varadan, V. K. *J. Eur. Ceram. Soc.* **2003**, *23*, 659.
- (468) Noda, H.; Muramoto, H. K. *J. Mater. Sci.* **2003**, *38*, 2043.
- (469) Bagwell, R. B.; Messing, G. L.; Howell, P. R. *J. Mater. Sci.* **2001**, *36*, 1833.
- (470) McHale, J. M.; Yureki, K.; Dabbs, D. M.; Novrotsky, A.; Sunderesan, S.; Aksay, I. A. *Chem. Mater.* **1997**, *9*, 3096.
- (471) Bowen, P.; Carry, C. *Powder Technol.* **2002**, *128*, 248.
- (472) Ragan, D. D.; Mates, T.; David, R. *J. Am. Ceram. Soc.* **2003**, *86*, 541.
- (473) Rossignol, S.; Kappenstein, C. *Int. J. Inorg. Mater.* **2001**, *3*, 51.
- (474) Appel, S.; Clausen, R.; Chouvanov, A.; Natter, H.; Hempelman, R.; Sabine, X.; Vollath, D. *Ceram. Eng. Sci. Proc.* **2002**, *23*, 585.
- (475) Zou, H.; Ge, X.; Shen, J. *Thermochim. Acta* **2003**, *397*, 81.
- (476) Cornell, R. M.; Schwertmann, U. *The Iron Oxides*; VCH: Weinheim, 1996.
- (477) Weiss, W.; Ranke, W. *Prog. Surf. Sci.* **2002**, *70*, 151.
- (478) Feltin, N.; Pileni, M. P. *Langmuir* **1997**, *13*, 3927.
- (479) Morales, M. P.; Pecharroman, C.; Conzaes Carreño, T.; Serna, C. J. *J. Sol. State Chem.* **1994**, *108*, 158.
- (480) Moreno, E. M.; Zayat, M.; Morales, M. P.; Serna, C. J.; Roig, A.; Levi, D. *Langmuir* **2002**, *18*, 4972.
- (481) Jolivet, J. J.; Chaneac, C.; Tronc, E. *Chem. Commun.* **2004**, 472.
- (482) Corrias, A.; Ennas, G.; Montjoy, G.; Paschina, G. *Phys. Chem. Chem. Phys.* **2000**, *2*, 1045.
- (483) Ennas, G.; Marongini, G.; Musini, A.; Falqui, A.; Belliarano, P.; Camini, R. *J. Mater. Res.* **1999**, *14*, 1570.
- (484) Chanéac, C.; Tronc, E.; Jolivet, J. P. *Nanostructured Mater.* **1995**, *6*, 715.
- (485) Larcher, D.; Masquelier, C.; Bonnin, D.; Chabre, Y.; Masson, V.; Leriche, J. B.; Tarasxob, J. M. *J. Electrochem. Soc.* **2003**, *150*, A133.
- (486) Hüfner, S. *Adv. Phys.* **1994**, *43*, 183.
- (487) Sebastian, I.; Bertrams, T.; Meinel, K.; Neddermeyer, H. *Faraday Discuss.* **1999**, *114*, 129.
- (488) Carnes, C. L.; Stipp, J.; Klabunde, K. J.; Bonevich, J. *Langmuir* **2002**, *18*, 1352.
- (489) Jones, F. H.; Dixon, R.; Foord, J. S.; Egdel, R. G.; Pethica, J. B. *Surf. Sci.* **1997**, *376*, 367.
- (490) Cox, D. F.; Fryberger, T. B.; Semancik, S. *Phys. Rev. B* **1988**, *38*, 2072.
- (491) Manassidis, I.; Goniakovski, J.; Kantorovich, L. N.; Gillan, M. J. *Surf. Sci.* **1995**, *339*, 258.
- (492) Fröhlich, D.; Klenkies, R.; Helbig, R. *Phys. Rev. Lett.* **1978**, *41*, 1750.
- (493) Samson, S.; Fonstad, C. G. *J. Appl. Phys.* **1973**, *44*, 4618.
- (494) Bläser, G.; Rühl, Th.; Diehl, C.; Ulrich, M.; Kohl, D. *Phys. A* **1999**, *266*, 218.
- (495) Centi, G.; Trifiro, F. *Catal. Rev.* **1986**, *28*, 165.
- (496) Popescu, D. A.; Herrmann, J.-M.; Ensueque, A.; Bozon-Verduraz, F. *Phys. Chem. Chem. Phys.* **2001**, *3*, 2522.
- (497) Lu, F.; Liu, Y.; Dong, M.; Wang, X. *Sens. Actuators B* **2000**, *66*, 225.
- (498) Bahnemann, D. W.; Kormann, C.; Hoffmann, R. *J. Phys. Chem.* **1987**, *91*, 3789.
- (499) Jing, L.; Xu, Z.; Shang, J.; Sun, X.; Guo, H. *Mater. Sci. Eng. A* **2002**, *332*, 356.
- (500) Boresov, G. K. *Adv. Catal.* **1965**, *15*, 285.
- (501) Novakova, J. *Catal. Rev.* **1970**, *4*, 77.
- (502) Winter, E. R. S. *J. Chem. Soc. A* **1968**, 2289.
- (503) Doornkamp, C.; Clement, M.; Ponc, V. *J. Catal.* **1999**, *182*, 390.
- (504) Doornkamp, C.; Clement, M.; Gao, X.; Deo, G.; Wachs, I. E.; Ponc, V. *J. Catal.* **1999**, *185*, 415.
- (505) Li, C.; Domen, K.; Maruya, K.-I.; Onishi, T. *J. Am. Chem. Soc.* **1989**, *111*, 7683.
- (506) Karasuda, T.; Aika, K.-I. *J. Catal.* **1997**, *171*, 439.
- (507) Yeung, J. A.; Bell, A. T.; Iglesia, E. *J. Catal.* **1999**, *185*, 213.
- (508) Martin, D.; Duprez, D. *J. Phys. Chem. B* **1996**, *100*, 9429.
- (509) Ishihara, I.; Kilner, J. A.; Honda, M.; Sakai, N.; Yokokawa, H.; Takita, Y. *Solid State Ionics* **1998**, *113–115*, 593.
- (510) Duprez, D. *Stud. Surf. Sci. Catal.* **1997**, *112*, 13.
- (511) Iglesias-Juez, A. B.; Hungria, O.; Gálvez, M.; Fernández-García, A.; Martínez-Arias, A.; Guerrero-Ruiz, J. C.; Conesa, J.; Soria, *Stud. Surf. Sci. Catal.* **2001**, *138*, 347.
- (512) Brossmann, U.; Sodervall, U.; Wurschum, R.; Schaefer, H.-E. *Nanostructured Mater.* **1999**, *12*, 871.
- (513) Knauth, P.; Tuller, H. L. *J. Am. Ceram. Soc.* **2002**, *85*, 1654.
- (514) Heitjans, P.; Indris, S. *J. Phys.: Condens. Matter* **2003**, *15*, R1257.
- (515) Kim, S.; Maier, J. *J. Electrochem. Soc.* **2002**, *149*, J73.
- (516) Tschöpe, A.; Sommer, E.; Birringer, R. *Solid State Ionics* **2001**, *139*, 255.

- (517) Knauth, P.; Tuller, H. L. *Solid State Ionics* **2000**, 136–137, 1215.
- (518) Chiang, Y.-M.; Lavik, E. B.; Blom, D. A. *Nanostructured Mater.* **1997**, 9, 633.
- (519) Maier, J. *Z. Phys. Chem.* **2003**, 217, 415.
- (520) Tschöpe, A. *Solid State Ionics* **2001**, 139, 267.
- (521) Bange, K. *Sol. Energy Mater. Sol. Cells* **1999**, 58, 1.
- (522) Green, M. *Ionics* **1999**, 5, 161.
- (523) Gondopadhyay, R.; De, A. *Chem. Mater.* **2000**, 13, 608.
- (524) Gratzel, M. *Nature* **2001**, 414, 338.
- (525) Salem, I. *Catal. Rev. Sci. Eng.* **2003**, 45, 205.
- (526) Kawahara, T.; Konishi, Y.; Tada, H.; Tohge, N.; Nishii, J.; Ito, S. *Angew. Chem., Int. Ed.* **2002**, 41, 2811.
- (527) Ikeda, S.; Sugiyama, N.; Murakami, S.-Y.; Kominari, H.; Kera, Y.; Noguchi, H.; Uosaki, K.; Torimoto, T.; Ohtani, B. *Phys. Chem. Chem. Phys.* **2003**, 5, 778.
- (528) Anpo, M.; Takeuchi, M. *J. Catal.* **2003**, 216, 505.
- (529) Asahi, R.; Morikawa, T.; Ohwaki, T.; Aoki, K.; Taga, Y. *Science* **2001**, 293, 269.
- (530) Thurson, T. R.; Wilcoxon, J. P. *J. Phys. Chem. B* **1999**, 103, 11.
- (531) Peter, L. M.; Wijanyanta, K. G.; Riley, D. J.; Wagget, J. P. *J. Phys. Chem. B* **2003**, 107, 8378.
- (532) Lee, C. Y.; Macquart, R.; Zhou, Q.; Kennedy, B. J. *J. Solid State Chem.* **2003**, 174, 310.
- (533) Yin, J.; Zou, Z.; Ye, J. *Chem. Phys. Lett.* **2003**, 378, 24.
- (534) Al-Abadleh, H. A.; Grassian, V. H. *Surf. Sci. Rep.* **2003**, 52, 63.
- (535) Davydov, A. A. *Infrared Spectra of Adsorbed Species on the Surface of Transition Metal Oxides*; Wiley: Chichester, 1990.
- (536) Busca, G. *Catal. Today* **1998**, 41, 191.
- (537) Hadjivanov, K. I. *Catal. Rev.* **2000**, 42, 71.
- (538) Burcham, L. J.; Briand, L. E.; Wachs, I. S. *Langmuir* **2001**, 17, 6164.
- (539) Burcham, L. J.; Briand, L. E.; Wachs, I. S. *Langmuir* **2001**, 17, 6175.
- (540) Ryczkowski, J. *Catal. Today* **2001**, 68, 263.
- (541) Somorjay, G. A.; McCrear, K. R. *Adv. Catal.* **2000**, 45, 385.
- (542) Haw, J. F.; Xu, T. *Adv. Catal.* **1998**, 42, 115.
- (543) Hunger, M. *Catal. Rev.* **1997**, 39, 345.
- (544) Che, M.; Tench, A. J. *Adv. Catal.* **1983**, 32, 1.
- (545) Martínez-Arias, A.; Fernández-García, M.; Conesa, J. C. In *Catalysis by Ceria and Related Materials*; Trovarelli, A., Ed.; Imperial College Press: London, 2002; Chapter 5.
- (546) Liu, P.; Rodriguez, J. A. *J. Chem. Phys.* **2003**, 119, 10895.
- (547) Rodriguez, J. A.; Pérez, M.; Jirsak, T.; Evans, J.; Hrbek, J.; González, L. *Chem. Phys. Lett.* **2003**, 378, 526.
- (548) Lopez, N.; Nørskov, J. K. *J. Am. Chem. Soc.* **2002**, 124, 11262.
- (549) Giordano, L.; Pacchioni, G.; Illas, F.; Rösch, N. *Surf. Sci.* **2002**, 499, 73.
- (550) González, S.; Sousa, C.; Fernández-García, M.; Bertin, V.; Illas, F. *J. Phys. Chem. B* **2002**, 106, 7839.
- (551) Liu, P.; Rodriguez, J. A.; Muckerman, J. *J. Phys. Chem. B*, in press.
- (552) DeSantis, E.; Ferrari, J.; González, L.; Pérez, M.; Evans, J.; Rodriguez, J. A., to be published.
- (553) Wichtendahl, R.; Rodriguez-Rodrigo, M.; Härtel, U.; Kuhlenbeck, H.; Freund, H.-J. *Phys. Status Solidi A*, **1999**, 173, 93.
- (554) He, J.-W.; Estrada, C. A.; Corneille, J. S.; Wu, M.-C.; Goodman, D. W. *Surf. Sci.* **1992**, 261, 164.
- (555) Pacchioni, G. *Surf. Rev. Lett.* **2000**, 7, 2777.
- (556) Jones, C. F.; Reeve, R. A.; Rigg, R.; Segall, R. L.; Smart, R. S. C.; Turner, P. S. *J. Chem. Soc., Faraday Trans. 1*, **1984**, 80, 2609.
- (557) Onishi, H.; Egawa, C.; Aruga, T.; Iwasawa, Y. *Surf. Sci.* **1987**, 191, 479.
- (558) Xu, C.; Goodman, D. W. *Chem. Phys. Lett.* **1997**, 265, 341.
- (559) Stirniman, M. J.; Huang, C.; Scott-Smith, R.; Joyce, S. A.; Kay, B. D. *J. Chem. Phys.* **1996**, 105, 1295.
- (560) McGraw, L. T.; Yu, C.-M.; Thomas, J. *Langmuir* **2000**, 23, 352.
- (561) Schneider, W. F.; Li, J.; Hass, K. C. *J. Phys. Chem. B* **2001**, 105, 6972.
- (562) Pacchioni, G.; Clotet, A.; Ricart, J. M. *Surf. Sci.* **1994**, 315, 337.
- (563) Jiang, Y.; Decker, S.; Mohs, C.; Klabunde, J. K. *J. Catal.* **1998**, 180, 24.
- (564) Elder, S. H.; Cot, F. M.; Heald, S. M.; Fyryhkin, A. M.; Bowman, M. K.; Gao, Y.; July, A. G.; Blamer, M. L.; Kolwaite, A. C.; Magrini, K. A.; Blake, A. M.; *J. Am. Chem. Soc.* **2000**, 122, 5138.
- (565) Martyanov, I. N.; Klabunde, K. L. *J. Catal.* **2004**, 224, 340.
- (566) Delmon, B. In *Handbook of Heterogeneous Catalysis*; Ertl, G., Knözinger, H., Weitkamp, J., Eds.; Wiley-VCH: New York, 1997; pp 264–277.
- (567) Rodriguez, J. A.; Hanson, J. C.; Frenkel, A. I.; Kim, J. Y.; Pérez, M. *J. Am. Chem. Soc.* **2002**, 124, 346.
- (568) Kim, J. Y.; Rodriguez, J. A.; Hanson, J. C.; Frenkel, A. I.; Lee, P. L. *J. Am. Chem. Soc.* **2003**, 125, 10684.
- (569) Evans, J.; Lee, H. In *Topics in Environmental Catalysis*; Rao, S. V., Ed.; Interscience: New York, 2001; pp 187–214.

CR030032F